Spring 2016

Hierarchical control of complex manufacturing processes

Hesam Zomorodi Moghadam

Department: Mechanical and Aerospace Engineering

HIERARCICAL CONTROL OF COMPLEX MANUFACTURING PROCESSES

by

HESAM ZOMORODI MOGHADAM

A DISSERTATION

Presented to the Faculty of the Graduate School of the

MISSOURI UNIVERSITY OF SCIENCE AND TECHNOLOGY

In Partial Fulfillment of the Requirements for the Degree

DOCTOR OF PHILOSOPHY

in

MECHANICAL ENGINEERING

2016

Approved by
Robert G. Landers, Advisor
S. N. Balakrishnan
Douglas A. Bristow
Ming Leu
Jagannathan Sarangapani

PUBLICATION DISSERTATION OPTION

This dissertation consists of the following three papers, formatted in the styles used by the specified journals listed as follows:

Paper 1 (pages 13-43), H. Zomorodi, R. G. Landers, and S. N. Balakrishnan, "Hierarchical Optimal Contour Control of Motion Systems," *Mechatronics*, 2014, vol. 24, no. 2, pp. 98-107.

Paper 2 (pages 44-72), H. Zomorodi, R. G. Landers, and S. N. Balakrishnan, "Hierarchical Optimal Force-position Control of Complex Manufacturing Processes," *Control Engineering Practice*, 2014, vol. 25, pp. 75-84.

Paper 3 (pages 73-105), H. Zomorodi, and R. G. Landers, "Hierarchical Explicit Model Predictive Control for Extrusion Fabrication Processes," *(under preparation)*.

ABSTRACT

The need for changing the control objective during the process has been reported in many systems in manufacturing, robotics, etc. However, not many works have been devoted to systematically investigating the proper strategies for these types of problems. In this dissertation, two approaches to such problems have been suggested for fast varying systems. The first approach, addresses problems where some of the objectives are statically related to the states of the systems. Hierarchical Optimal Control was proposed to simplify the nonlinearity caused by adding the statically related objectives into control problem. The proposed method was implemented for contour-position control of motion systems as well as force-position control of end milling processes. It was shown for a motion control system, when contour tracking is important, the controller can reduce the contour error even when the axial control signals are saturating. Also, for end milling processes it was shown that during machining sharp edges where, excessive cutting forces can cause tool breakage, by using the proposed controller, force can be bounded without sacrificing the position tracking performance. The second approach that was proposed (Hierarchical Model Predictive Control), addressed the problems where all the objectives are dynamically related. In this method neural network approximation methods were used to convert a nonlinear optimization problem into an explicit form which is feasible for real time implementation. This method was implemented for force-velocity control of ram based freeform extrusion fabrication of ceramics. Excellent extrusion results were achieved with the proposed method showing excellent performance for different changes in control objective during the process.

ACKNOWLEDGMENTS

First and foremost, I would like to thank my advisor, Dr. Robert G. Landers, for teaching me the qualities of a professional researcher and for showing me the importance of paying attention to details in every aspect of life. Also, I would like to thank him for his continuous support during my studies. I would like to thank Dr. S. N. Balakrishnan for his thoughtful ideas, inspiring talks, and encouragements during my studies. I am grateful to Dr. Douglas Bristow for his insightful comments and suggestions. Also, I would like to express my thanks to Dr. Jag Sarangapani and Dr. Ming Leu for their in-depth suggestions to improve this work. Thanks to Ankush Chakrabarty for his helpful suggestions on implementation aspects of Model Predictive Control. Thanks to Karthikeyan Rajgapool for his help with implementation aspects of Modified State Observer. Thanks to Nima Lotfi for his professional collaboration during multiple projects. Thanks to Mitchell S. Cottrell, for his ongoing technical help in a lot of my research projects. Thanks to Katherine Wagner, for her help with my official paper works at multiple points in my studies.

I would like to thank my friends for their love, support, and friendship during these years here in Missouri S&T. Friends, who have been and will always be an important part of my life. I would not have achieved what I have today without their emotional support and encouragements.

Lastly, I would like to thank my family that without their support I would not be at this point in my career. I am grateful to them for always encouraging me during my ups and downs in this path. This work is dedicated to my parents, brothers, sister, and my girlfriend Maryam.

TABLE OF CONTENTS

Page

PUBLICATION DISSERTATION OPTION iii

ABSTRACT iv

ACKNOWLEDGMENTS v

LIST OF ILLUSTRATIONS viii

LIST OF TABLES x

SECTION

1. INTRODUCTION 1

1.1. HIERARCHICAL CONTROL 1

1.2. HIERARCHICAL CONTROL COMPLEX MOTION SYSTEMS 2

1.3. HIERARCHICAL FORCE–POSITION CONTROL OF END MILLING PROCESSES 3

1.4. HIERARCHICAL OF EXTRUSION FABRICATION PROCESSES 6

PAPER

I. Hierarchical optimal contour control of motion systems 10

ABSTRACT 10

1. Introduction 11

2. Hierarchical contour control methodology 16

3. Experimental results and discussion 23

4. Summary and conclusions 27

Acknowledgement 28

Appendix A. Stability proof of the proposed controller 28

References 31

II. Hierarchical optimal force–position control of complex manufacturing 44

ABSTRACT 44

1. Introduction 45

2. Approach 48

3. Results and discussion 61

3.1. Hierarchical control analysis 63

3.2. Comparison of hierarchical and decentralized control 66

4. Summary and conclusions 69

Refrences 71

III. Hierarchical explicit model predictive control for extrusion fabrication processes 74

ABSTRACT 74

1. Introduction 75

2. Experimental setup 79

3. System dynamics 80

4. Control structure 84

4.1. Process level 86

4.2. Supervisory level 87

5. Determining design and process parameters 89

6. Results and discussion 94

7. Summary and conclusions 96

References 96

SECTION

2. SUMMARY AND CONCLUSIONS 109

REFERENCES 114

VITA 118

LIST OF ILLUSTRATIONS

Page

PAPER I

Fig. 1. Table top CNC machine. 35

Fig. 2. Block diagram of the proposed controller. 36

Fig. 3. Diamond contour schematic. 36

Fig. 4. Maximum transient errors for Cases I–V. 37

Fig. 5. Detailed plot of experimental points at right corner for low contour emphasis versus high contour emphasis. 38

Fig. 6. Right corner transient responses for Cases I–V. 38

Fig. 7. Top corner transient responses for Cases I–V. 39

Fig. 8. Steady state errors for Cases I–V. 39

Fig. 9. Experimental Results for Case V. 40

Fig. 10. Freeform contour schematic. 41

Fig. 11. Maximum transient errors for Cases VI–X. 42

Fig. 12. Steady state errors for Cases VI–X. 42

Fig. 13. Experimental Results for Case VI. 43

PAPER II

Fig. 1. Table top CNC machine. 49

Fig. 2. Machining forces acting on tool in end milling process; a) top view b) front view 54

Fig. 3. Diamond contour used for simulation studies. 62

Fig. 4. Simulation of results for hierarchical controllers at diamond's right corner. 64

Fig. 5. Detailed simulation results for Case I. 65

Fig. 6. Detailed simulation results for Case IX. 66

Fig. 7. Simulation results for decentralized controllers at diamond right corner. 67

Fig. 8. Maximum axis position, contour, and machining force errors for hierarchical and decentralized controllers. 69

PAPER III

Fig. 1. FEF experimental system. 100

Fig. 2. Steady state ram velocity versus steady state extrusion force (Marker points denote experimental data and continuous lines denote the model). 101

Fig. 3. Illustration of hysteresis switching function for q_F. 101

Fig. 4. Experimental investigation of disturbance bounds.....102

Fig. 5. Neural network approximation results. 103

Fig. 6. Step test for evaluating the full emphasis on force tracking. 104

Fig. 7. Dash lines printed with 0.609 mm diameter nozzle and ram velocity of 0.01 mm/s and variable table feed rates. 104

Fig. 8. Normalized thickness versus normalized table feed rate 105

Fig. 9. Extrusion force, ram velocity, and command voltage signals.....106

Fig. 10. Printed dash lines.....107

Fig. 11. Comparison of line thicknesses along the line length. 108

LIST OF TABLES

Page

PAPER I

Table 1 Diamond Contour Cases. 37

Table 2 Freeform Contour Cases. 41

PAPER II

Table 1 Hierarchical controller simulation cases. 64

Table 2 Decentralized controller simulation cases (i.e., $q = 0$). 67

PAPER III

Table 1 Steady state relationship between extrusion force and ram velocity for various pastes and nozzle lengths, and a 0.609 mm nozzle diameter 100

SECTION

1. INTRODUCTION

1.1. HIERARCHICAL CONTROL

The need for variations in the control objective during the process has many examples in manufacturing and robotics [1-4]. For example, when drilling a through hole in a part, it has been shown [3] that at the beginning and end of the process, in order to reduce the burr formation at the two openings of the drilled hole, it is desired to control the tools feed rate while in the middle, in order to reduce tool wear and prevent tool failure it is desired to control the normal drilling force. In cases like the one mentioned, there is a need to systematically switch the control structure emphasis during the process (in this case, between force tracking and velocity tracking). In other areas like robotics, such examples have been reported in the literature many times. For example, Takahashi et al. [5], introduced a robust force and position control method for grasping of unknown objects by a multi fingered robotic hand. The method proposed by Takahashi et al. was capable of switching between the force control and position control according to the amount of the external force. In manufacturing, Ulsoy and Koren [6] investigated the literature in machining control at three levels (i.e., servo, process, and supervisory), and suggested the need for incorporating all three levels in the control structure. One of the methods for addressing this problem is the use of a hierarchical control structure where a supervisory level is responsible for monitoring the status of the system and deciding which control strategy should be adopted in the lower levels. In the lower levels normally a flexible controller method is incorporated that can place emphasis on different

objectives as commanded by the supervisory level [3, 4, 7]. For example, Landers and Balakrishnan [8], proposed a hierarchical optimal control structure to control the motion of a two–axis bi-linear system. In another work by Tang et al. [9], the same hierarchical optimal control methodology was expanded to simultaneously regulate machining force, and servomechanism position errors in a milling process. However in these works the effect of control objective variation was not analyzed and no strategy was considered for uncertainties and disturbances in the process dynamics. In this research three different applications of using hierarchical control structure is investigated and different strategies are suggested for simplification of the control structure as well as dealing with different uncertainties and disturbances in the process.

1.2. HIERARCHICAL CONTROL COMPLEX MOTION SYSTEMS

In the first paper, the problem of tracking complex contours is considered which involves compensation of the axial error versus the contour error (i.e., the shortest distance from the actual point to the contour). Normally in the literature, contour error compensation is addressed through the Cross Coupling Control concept and its variations [10-13]. However, Cross Coupling Control does not provide a flexible platform to vary the emphasis between axial error and contour error which is needed for cases where variable objective is desired. Also a lot of other techniques that use the concept of Cross Coupling Control but with more advanced algorithms lack this feature. For example Chu et al. proposed a two section control signal; a Proportional controller to compensate the axial error and an optimal control signal with the quadratic difference between the positions of two parallel axes used as the cost, to account for asynchronicity [14].

Kulkarni et al. also, used the same control structure to reduce the axial error while compensating the contour error [15]. In these works, there is no flexible platform to vary the emphasis from axial error compared to synchronicity error. Also none of these works have provided a systematic way for introducing different objectives as the synchronizing strategy.

Landers and Balakrishnan [8], combined contour and servomechanism control, using hierarchical optimal control techniques, for a two–axis motion control system. In another work by Tang et al. [9], a hierarchical optimal control methodology was introduced that simultaneously regulated machining force processes, contour error, and servomechanism position errors. In these works an error–space based method proposed by Franklin and Powell [16] was utilized and applied via simulation studies. In the first paper a similar hierarchical structure as [8] was introduced in which the process level was divided into two levels of operation. In the higher level the contour error was considered and using a propagation relationship with the lower level was propagated to the lower level where the servo dynamics of two axes were considered. This formulation created a flexible controller in the process level which was able to vary the emphasis of the control from axial error compensation to contour error compensation. It was shown that at some points during a tracking task it was beneficial to place more emphasis on contour error.

1.3. HIERARCHICAL FORCE–POSITION CONTROL OF END MILLING PROCESSES

In the second paper, the problem of contour tracking while machining a part in end milling processes was considered. The objective of this work was to bind the normal

cutting force during an end milling process under a desired value without sacrificing the tracking performance of the system.

Controlling force and position in an actuator is a well-developed research area in robotics. Siciliano et al. have published a survey on force/position control techniques [17]. The force/position control techniques can be divided into two groups; Open loop methods and closed loop methods [17]. In open loop techniques the system is controlled by developing a relationship between force and position [18]. In this category Impedance control (i.e., regulating the mechanical impedance of the robot end-effector) is the main path of research [19]. Examples of these works are optimal adaptive impedance force/position control for robotic manipulators [20], and impedance force control for a surgical bone milling device [21].

In the closed loop force (also called hybrid force/position control) category force and position are independently controlled [18, 19, 22]. Typically, the works in this area can be divided into explicit or parallel and implicit methods. Explicit closed loop force control methods involve modifying the control signal directly by the force tracking error. The example of this group are explicit position/force control for parallel robots using computed torque method based on end effector position and force measurements[22], online learning neural networks technique for hybrid position/force control of flexible actuators using visual information and force measurements [23], and manipulators control using a neuro-adaptive controller in compliant contact with a surface under non-parametric uncertainties [24]. Implicit hybrid force/position control methods comprise two control loops; an inner position control loop and an outer control loop that is responsible for modifying the reference to the inner loop in order to regulate the force

error and position error simultaneously [25]. Examples of this group are controlling a anthropomorphic hand using cascaded implicit force/position control [22], tracking an object of unknown shape using iterative-learning implicit force/position control [26], impulsive hybrid force/position control[18], adaptive implicit force/position control based on Least Square methods [27].

Although there is large number of literature devoted to force/position control, few studies have focused on the integration of machining force and position control in manufacturing. Also the as mentioned before, sometimes in manufacturing there is a need for an algorithm that provides the ability to switch emphasis between force and position control which requires a more flexible control structure. Ulsoy and Koren [6], suggested the need for a hierarchical control structure for controlling the machining systems. A hierarchical optimal control methodology was developed by Tang et al. [9] in order to incorporate machining force, contour, and position control in a lathing process simultaneously. However no considerations for model uncertainties and the noise inherent in the physical system were considered in the method proposed by Tang et al. [9]. In the second paper of this dissertation a control hierarchy based on a work by Tang et al. [9] was introduced to create a flexible framework for controlling force and position in end milling processes while also accounting for system uncertainties and inherent measurement noises. Like the first paper, here, the process level consisted of two levels where in the higher level the force tracking problem was considered and in the lower level the position tracking was considered. A relationship between the normal cutting force error and the axial errors was developed to aggregate the higher level objective to the lower level in the form of a linear optimal control problem.

1.4. HIERARCHICAL OF EXTRUSION FABRICATION PROCESSES

In the third paper, control of ram based extrusion for ceramics was considered. Using ceramic parts has gained a tremendous interest in industries such as automotive, energy, biomedical, etc. However because of their hardness machining ceramics is difficult [28] also, it is known that using molds for small scale production are expensive [29]. Therefore, for small scale production of ceramic parts, Additive Manufacturing processes have emerged as a potential solution. Extrusion Freeforming which is building a 3D part by deposition of pastes in a layer-by-layer fashion, is one of the main methods of Additive Manufacturing for ceramics [30]. Freeze-form Extrusion Fabrication (FEF) [31] is a Extrusion Freeforming in which a water based ceramic paste is loaded inside a reservoir and is pushed into a nozzle using a ram and plunger system that are driven by a linear motion system. The flow of the paste coming out of the nozzle is normally controlled by either controlling the velocity of the ram [32, 33] or by controlling the paste pressure (or the force that ram applies to the plunger) [34, 35]. One of the advantages of FEF method compared to other Extrusion Freeforming methods is that in FEF pastes are water based and very low amounts of organic binders are needed for paste preparation compared to other methods, which saves a lot of time in the binder burn out stage and is more environmentally friendly [36, 37]. However, normally the pastes used in FEF have complex rheologies and because of the preparation stages involved different amounts of air can be mixed with the paste which leads to uncertainties in the linear relationship between ram velocity and paste flow [38]. According to previous studies [38], only when paste is flowing out of the nozzle and the extrusion force is at a steady state value, the

ram velocity can be considered linearly related to the paste flow rate. As a result ram velocity control techniques alone, are not reliable for controlling the paste flow in FEF systems. Therefore, the different works have focused on controlling the paste flow by controlling the pressure of the paste [39]. However in force control techniques, since paste flow cannot be systematically related to the extrusion force, the table feed rate should be found by try and error and as a result the thickness of the extruded line might not be consistent when paste type is changed. As mentioned before, with constant velocity methods in steady state, the paste flow is related to the ram velocity by $V_n = \frac{r_p V_r}{r_n}$ where V_r is the ram velocity, r_n is the radius of the nozzle, r_p is the radius of the plunger, and V_n is the nozzle velocity. Therefore a table feed rate can be calculated in order to deposit lines with a desired thickness regardless extrusion force which is a function of the paste type and nozzle dimension. Deuser et al. [40], introduced a hybrid force-velocity control method where at the start and stop extrusion and air bubble release, force control was engaged and during the steady state stage, velocity control was active. In this work, this problem was addressed through a hierarchical control structure. In the process level a Model Predictive Controller was designed that would allow variable control objectives (i.e., force tracking or velocity tracking). In the supervisory level, an algorithm was developed for detecting the system status and changing the objective of the controller.

Here is a chronological list of papers I have published (as an author and coauthor) in journals and conferences during my Ph.D. studies;

1. H. Zomorodi, R. G. Landers, and S. N. Balakrishnan, “Hierarchical Position-contour Control of Linear Axes”, *International Symposium on Flexible Automation*, Tokyo, Japan, 2010, July 12–14.
2. H. Zomorodi, R. G. Landers, and S. N. Balakrishnan, “Hierarchical Optimal Force-position Control of Complex Manufacturing Processes”, *International Symposium on Flexible Automation*, St. Louis, MO, 2012, June 18-20.
3. J. Ishaku, N. Lotfi, H. Zomorodi, and R. G. Landers, “Control-Oriented Modeling for Open-Cathode Fuel Cell Systems”, *American Control Conference*, Portland, OR, 2014, June 4-6.
4. H. Zomorodi, R. G. Landers, and S. N. Balakrishnan, “Hierarchical Optimal Contour Control of Motion Systems”, *Mechatronics*, 2014, vol. 24, no. 2, pp. 98-107.
5. H. Zomorodi, R. G. Landers, and S. N. Balakrishnan, “Hierarchical Optimal Force-position Control of Complex Manufacturing Processes”, *Control Engineering Practice*, 2014, vol. 25, pp. 75-84.
6. N. Lotfi, H. Zomorodi, and R. G. Landers, “Thermal Management and Voltage Stabilization in Air-Forced Open-cathode Fuel Cells”, *ASME Dynamic Systems and Control Conference*, Columbus, OH, 2015, October 28-30.
7. H. Zomorodi, and R. G. Landers, “Extrusion Based Additive Manufacturing Using Explicit Model Predictive Control”, *American Control Conferacne (submitted)*.
8. H. Zomorodi, and R. G. Landers, “Hierarchical Explicit Model Predictive Control for Extrusion Fabrication Processes”, *(in preparation)*.

9. N. Lotfi, H. Zomorodi, and R. G. Landers, “Adaptive Voltage regulation in Air-Forced Open-cathode Fuel Cells”, *(in preparation)*.

However, this dissertation is composed of papers 4, 5, and 8 of the above list.

PAPER

I. Hierarchical optimal contour control of motion systems

ABSTRACT

Many motion control applications utilize multiple axes to traverse complex trajectories. The hierarchical contour control methodology proposed in this paper treats each axis as an individual subsystem and combines the Internal Model Principle with robust tracking and optimal hierarchical control techniques to track a desired trajectory. In this method the objectives are divided into two levels. Measurable goals of each subsystem are included in the bottom level and unmeasurable goals, which are estimated using the bottom level states, are considered in the top level where the subsystems are synchronized. The proposed methodology reduces system complexity while greatly improving tracking performance. The tracking error for each axis is considered in the bottom level where the Internal Model Principle is used to compensate for unmodeled nonlinear friction and slowly varying uncertainties. The top level goal (i.e., zero contour error) is propagated to the lower level by an aggregation relationship between contour error and physical linear axis variables. A controller is designed at the bottom level which simultaneously satisfies the bottom level goals (i.e., individual axis tracking) and the top level goal. Experimental results implemented on a table top CNC machine for diamond and freeform contours illustrate the performance of the proposed methodology. While this methodology was implemented for a two–axis motion system, it can be extended to any motion system containing more than two axes.

KEYWORDS: Contour Control, Discrete Optimal Control, Hierarchical Control

1. Introduction

Accurate trajectory control is a fundamental requirement in most motion control applications (e.g., robotics, manufacturing). For many contours multiple axes must be utilized simultaneously. When the independent controllers for each axis are utilized, any differences in the performance of one axis caused by disturbances, variation in parameters, etc., in addition to tracking errors, may cause the axes to become unsynchronized. This unsynchronized motion produces contour error, which is defined as the closest distance between the current location and the desired path of the motion system. To compensate for axis and contour errors, two different approaches, respectively, have been adopted: tracking control and contour control. In tracking control, feedback control of individual axes was first utilized; however, since the reference is usually known, feed forward methods emerged to improve tracking performance. As examples, a velocity feed–forward loop was used in [1] and Zero Phase Error Tracking Control (ZPETC) was proposed in [2]. In addition to the drawbacks of these techniques (e.g., producing high frequency components in the control signal and sensitivity to disturbances and variations in parameters) they do not guarantee reduction of contour error, even though they improve single axis tracking. The literature in this area typically considers cases where no physical coupling exists between the axes. To regulate the synchronization error, a virtual coupling between the axes has been introduced using different methods [1, 3]. The first such technique was Cross Coupling Control (CCC)

proposed by Koren [4]. In CCC methods the contour error is calculated online and a modification to the control law or the reference signal is generated accordingly. Other methods have introduced virtual coupling using different approaches such as adaptive coupling control [5], fuzzy logic [6], neural network techniques [7], etc.

Studies in CCC can be divided in two groups by the strategy they adopt: pre–compensation and control signal manipulation. Several research studies utilized the idea of pre–compensation, which is regulating the contour error by manipulating the axis reference signals. Freng et al. [8] used CCC to minimize the orientation error of a differential–drive mobile robot by sending wheel speed correction signals. Chin et al. [9] proposed a Cross–Coupled Pre–compensation Method (CCPM) to improve accuracy and eliminate steady–state errors. Lee et al. [10] implemented real–time contour error compensation that calculated the contour error and modified the reference position commands. In another work Shih et al. [11] combined CCC with a multiple–loop cascaded control design method. Chin et al. [12] improved the performance of the CCPM by integrating it with a fuzzy logic algorithm. Cheng et al. [13] incorporated position feedback, velocity feedforward, a fuzzy regulator, and a CCC equipped with a real–time contour error estimator. Su et al. [14] combined position error pre–compensation, a modified CCC, and a fuzzy–logic based feedrate regulator. In the work by Altinas and Khoshdarregi [15] a vibration avoidance and contouring error compensation algorithm was proposed. In this work a pre–compensation component was generated from the axis closed–loop transfer functions. In order to improve the contour accuracy, input shaping filters were implemented on the generated reference positions for vibration avoidance.

Other research studies in CCC used the idea of directly manipulating the control signal of each axis. Part of the literature in this area used neural networks structure to improve robustness (e.g., [16]). Other studies have combined various control methods with CCC. Chiu et al. [17] introduced a coupling effect to each axis into a multi–axis system by the proper choice of a Lyapunov–like function. Ho et al. [18] proposed a path following controller with decoupled tangential and normal control. Yeh et al. [19] combined feedback proportional control and feedforward ZPETC control. A contour error transfer function was then derived to design the integrated controller. In another study Chiu et al. [20] proposed a method based on a moving coordinate frame attached to the desired contour. Chen et al. [21] used an integral sliding mode controller based on polar coordinates. In [22] a contouring error vector was estimated to efficiently determine the variable gains for CCC. A linear CCC was proposed in [23] to improve tracking accuracy at high speeds. In another study by Koren et al. [24], a proportional controller, cross coupling controller, and ZPETC were compared and the effect of their combination in a cross coupling formulation was analyzed. McNab et al., [25] formulated the contour tracking problem as a receding horizon linear quadratic problem with variable state weighting matrices. A stability proof was provided for linear reference trajectories. In a recent work by Tang and Landers [25] a model predictive controller was used to optimally synchronize the subsystems while a pre–compensation scheme was used to improve system performance by varying the feederate according to the predicted contour error. Ouyang et al. [26] proposed a PD contour controller in the position domain for a multiaxis system. In their method the motion of the axes are described by a function where one of the axes is considered to be the master axis. Guo et al. [27] combined

quantitative feedback theory with CCC for coordinating hydraulic motors. In places where friction or other unmodeled effects dominate the system response, fuzzy logic controllers are more applicable than other methods [24]. For example, [28] introduced an adaptive fuzzy controller for a 3 axis system with substantial nonlinear friction to ensure stability robustness. However, these methods cannot explicitly account for parametric uncertainties in the formulation. Lee et al. [30] proposed an adaptive method based on a Lyapunov technique for contour control in which the motion system friction and inertia were estimated on line. This method showed an improvement over PD controllers and CCC.

In most of the literature contour control has been investigated for two–dimensional applications. However, for many industrial applications precise motion is required for motion systems with more than two dimensions. Uchiyama et al. [31] suggested a contour controller for three–dimensional machining applications using a coordinate transformation based method. In another application for five axis machine tools, Sencer et al. [32] defined two types of contouring errors based on the normal deviation of the tool tip from the reference path, and the normal deviation of the tool axis orientation from the reference orientation using spherical coordinates.

Generally, in the studies concerning CCC, there is little attention paid to the flexibility of the control structure with respect to the process effects. For example, in case of a machining process, at some instances precise regulation of the contour error might lead to high control actions and hence higher machining forces which, in turn, might cause tool breakage. Optimal control techniques are usually incorporated in cross coupling control structure to address these issues. For example, [29] used a weighted

quadratic difference between each of the axes in the cost function of an optimal control formulation to account for the asynchronicity of the axes. Also, in [30] two different combinations of contour error and control signals in the cost function were investigated. In these works, to ensure a zero tracking steady state error in straight lines a Proportional controller was used for each axis which might result in oscillations in presence of measurement noises. Also in these studies no flexibility is available between the synchronicity control signal and tracking control signal. Therefore the net control signal that is sent to the motors is not guaranteed to be optimum. Some studies have considered a combination of control signal, tracking error, and synchronicity error in centralized optimal control formulation to overcome these issues. In [1] and [3] the asynchronicity problem of multiple axes has been address by a centralized optimal controller with a cost function consisting of a combination of tracking error, synchronicity error and, control signal. However model uncertainties and robustness to noise were not considered. None of these works have proposed a systematic way for introducing different objectives as the synchronizing strategy. For example, when machining a slot along a single axis, position control is very important a the beginning and end of the slot, while force control in the middle would be desirable to maximize operation productivity. As a result, there is a need for a systematic method to switch emphasis between axis tracking and machining process control. The need was first realized by Ulsoy and Koren [31] who investigated the literature in machining control at three levels (i.e., servo, process, and supervisory), and suggested the need of hierarchical methods to incorporate all three levels.

In Landers and Balakrishnan [32], contour and servomechanism control were combined, using hierarchical optimal control techniques, for a two–axis motion control

system. In another work by Tang et al. [33], a hierarchical optimal control methodology was introduced that simultaneously regulated machining force processes, contour error, and servomechanism position errors. In these works an error–space based method proposed by Franklin and Powell [34] was utilized and applied via simulation studies. In this paper, a hierarchical optimal contour controller is developed using optimal and feedforward control techniques and applied experimentally. A stability proof of the proposed hierarchical controller is given in the Appendix.

First, a dynamic model of a mini CNC machine is presented. To achieve robust tracking, the Internal Model Principle is utilized in the bottom level to compensate for unmodeled friction and other slowly varying uncertainties. Using a hierarchical structure, the contour error is propagated to the physical level through an aggregation relationship. The top level goal (i.e., zero contour error) is defined and propagated to the lower level by a linear aggregation relationship between contour error and the linear axis variables. A linear optimal control problem is then introduced with a cost function that includes the top and bottom level goals, as well as the control effort. Different experiments on a tabletop CNC explore the performance of the proposed methodology. Also a thorough investigation is provided on the effect of increasing or decreasing the importance of contour error.

2. Hierarchical contour control methodology

The contour control methodology is now derived for two linear axes, denoted x and y, of a table top CNC machine (Fig. 1). The methodology, however, is expandable to

motion systems with more than two axes. Assuming the electrical dynamics are much faster than the mechanical dynamics, a common feed drive system model is considered [35]. Including nonlinear friction, the dynamic equations of motion of the x and y axes, respectively, are

$$\tau_x \ddot{x}(t) + \dot{x}(t) = K_x u_x(t) - F_{fx}\left(\dot{x}(t)\right) \tag{1}$$

$$\tau_y \ddot{y}(t) + \dot{y}(t) = K_y u_y(t) - F_{fy}\left(\dot{y}(t)\right) \tag{2}$$

where τ the is time constant (s), K is the gain ((mm/s)/V), x and y are displacements (mm), u is the command voltage (V), and F_f is the nonlinear friction (mm/s). The subscripts x and y refer to the x and y axes, respectively. The subsequent analysis is applied to the x axis. Friction in this model is considered as an unknown constant disturbance and is rejected via the use of the Internal Model Principle. Therefore, an ideal model is considered first and is then modified based on the Internal Model Principle. Ignoring nonlinear friction, the transfer function relating the axis position to the command voltage is

$$G_x(s) = \frac{X(s)}{U_x(s)} = \frac{K_x}{\tau_x s^2 + s} \tag{3}$$

Equation (3) is transformed into the Z domain using a Zero Order Hold

$$G_x(z) = K_x \frac{\left[\left(\frac{T}{\tau_x} - 1 + e^{-\frac{T}{\tau_x}}\right)z + \left(1 - e^{-\frac{T}{\tau_x}} - \frac{T}{\tau_x}e^{-\frac{T}{\tau_x}}\right)\right]}{\frac{1}{\tau_x}(z-1)\left(z - e^{-\frac{T}{\tau_x}}\right)} \tag{4}$$

where T is the sample period. To apply the Internal Model Principle, the transfer function is multiplied by $\frac{z-1}{z-1}$. It can be shown that this will allow the controller to reject constant and slowly varying disturbances, as well as track ramp reference trajectories. The modified transfer function is

$$G_x(z) = \frac{\mathrm{b}_x(z)}{\mathrm{a}_x(z)} = \frac{b_{x1}z^2 + b_{x2}z + b_{x3}}{z^3 + a_{x1}z^2 + a_{x2}z + a_{x3}} \tag{5}$$

where $a_{x1} = -\left(e^{-\frac{T}{\tau_x}} + 2\right)z^2$, $a_{x2} = \left(2e^{-\frac{T}{\tau_x}} + 1\right)z$, $a_{x3} = -e^{-\frac{T}{\tau_x}}$, $b_{x1} = K_x\tau_x\left(\frac{T}{\tau_x} - 1 + e^{-\frac{T}{\tau_x}}\right)z^2$,

$b_{x2} = K_x\tau_x\left(2 - 2e^{-\frac{T}{\tau_x}} - \frac{T}{\tau_x}\left(1 + e^{-\frac{T}{\tau_x}}\right)\right)z$, and $b_{x3} = -K_x\tau_x\left(1 - e^{-\frac{T}{\tau_x}} - \frac{T}{\tau_x}e^{-\frac{T}{\tau_x}}\right)$.

Transforming equation (5) into the difference domain

$$\begin{aligned} x(k) + a_{x1}\,x(k-1) + a_{x2}\,x(k-2) + a_{x3}\,x(k-3) = \\ b_{x1}u_x(k-1) + b_{x2}u_x(k-2) + b_{x3}u_x(k-3) \end{aligned} \tag{6}$$

The system states are

$$\begin{aligned} x_1(k) &= x(k-2) = x_2(k-1) \\ x_2(k) &= x(k-1) = x_3(k-1) \\ x_3(k) &= x(k) = -a_{x1}\,x_3(k-1) - a_{x2}\,x_2(k-1) - a_{x3}\,x_1(k-1) + \\ &\qquad b_{x1}u_x(k-1) + b_{x2}u_x(k-2) + b_{x3}u_x(k-3) \end{aligned} \tag{7}$$

Now the error states with respect to a desired trajectory are

$$\begin{aligned} e_{x1}(k) &= r_x(k-2) - x_1(k) = e_{x2}(k-1) \\ e_{x2}(k) &= r_x(k-1) - x_2(k) = e_{x3}(k-1) \\ e_{x3}(k) &= r_x(k) - x_3(k) = -a_{x1}\,e_{x3}(k-1) - a_{x2}\,e_{x2}(k-1) - a_{x3}\,e_{x1}(k-1) + \mu_x(k-1) \end{aligned} \tag{8}$$

where

$$\begin{aligned}\mu_x(k) = r_x(k+1) + a_{x1} r_x(k) + a_{x2} r_x(k-1) + a_{x3} r_x(k-2) \\ - b_{x1} u_x(k) - b_{x2} u_x(k-1) - b_{x3} u_x(k-2)\end{aligned} \tag{9}$$

Letting the error state vector be $\mathbf{e_x}(k) = \begin{bmatrix} e_{x1}(k) & e_{x2}(k) & e_{x3}(k) \end{bmatrix}$, the x axis error system can be represented in state space as

$$\mathbf{e_x}(k) = \begin{bmatrix} 0 & 1 & 0 \\ 0 & 0 & 1 \\ -a_{x3} & -a_{x2} & -a_{x1} \end{bmatrix} \mathbf{e_x}(k-1) + \begin{bmatrix} 0 \\ 0 \\ 1 \end{bmatrix} \mu_x(k-1) = \mathbf{A_{ex}} \mathbf{e_x}(k-1) + \mathbf{B_{ex}} \mu_x(k-1) \tag{10}$$

The same procedure is applied to the y axis system. The total error system is

$$\mathbf{e}(k) = \mathbf{A_e} \mathbf{e}(k-1) + \mathbf{B_e} \boldsymbol{\mu}(k-1) = \begin{bmatrix} \mathbf{A_{ex}} & \mathbf{0}_{3\times3} \\ \mathbf{0}_{3\times3} & \mathbf{A_{ey}} \end{bmatrix} \begin{bmatrix} \mathbf{e_x}(k-1) \\ \mathbf{e_y}(k-1) \end{bmatrix} + \begin{bmatrix} \mathbf{B_{ex}} & \mathbf{0}_{3\times1} \\ \mathbf{0}_{3\times1} & \mathbf{B_{ey}} \end{bmatrix} \begin{bmatrix} \mu_x(k-1) \\ \mu_y(k-1) \end{bmatrix} \tag{11}$$

where $\mathbf{A_{ey}} = \begin{bmatrix} 0 & 1 & 0 \\ 0 & 0 & 1 \\ -a_{y3} & -a_{y2} & -a_{y1} \end{bmatrix}$ and $\mathbf{B_{ey}} = \mathbf{B_{ex}}$. The bottom level of the hierarchical structure consists of the total error system. Therefore, the total bottom level is

$$\mathbf{x_b}(k) = \mathbf{A_b} \mathbf{x_b}(k-1) + \mathbf{B_b} \mathbf{u_b}(k-1) = \mathbf{A_e} \mathbf{x_b}(k-1) + \mathbf{B_e} \mathbf{u_b}(k-1) \tag{12}$$

where $\mathbf{x_b}(k) = \mathbf{e}(k)$ and

$$\begin{aligned}\mathbf{u_b}(k) = \begin{bmatrix} \mu_x(k) \\ \mu_y(k) \end{bmatrix} = \begin{bmatrix} r_x(k+1) + a_{x1} r_x(k) + a_{x2} r_x(k-1) + a_{x3} r_x(k-2) \\ r_y(k+1) + a_{y1} r_y(k) + a_{y2} r_y(k-1) + a_{y3} r_y(k-2) \end{bmatrix} \\ - \begin{bmatrix} b_{x1} u_x(k) + b_{x2} u_x(k-1) + b_{x3} u_x(k-2) \\ b_{y1} u_y(k) + b_{y2} u_y(k-1) + b_{y3} u_y(k-2) \end{bmatrix}\end{aligned} \tag{13}$$

The upper level goal is defined in this work as zero contour error. In order to propagate the upper level goal to the lower level an aggregation relation between the

variables at both levels is required. The relationship between axial errors and contour error is [36]

$$\varepsilon(k) = \mathbf{C}_{\mathbf{x}}(k)\mathbf{e}_{\mathbf{x}}(k) - \mathbf{C}_{\mathbf{y}}(k)\mathbf{e}_{\mathbf{y}}(k) = \mathbf{C}(k)\mathbf{x}_{\mathbf{b}}(k) \tag{14}$$

where $\mathbf{C}(k) = \begin{bmatrix} 0 & 0 & c_x(k) & 0 & 0 & c_y(k) \end{bmatrix} = \begin{bmatrix} \mathbf{C}_{\mathbf{x}}(k) & -\mathbf{C}_{\mathbf{y}}(k) \end{bmatrix}$. The expressions for $\mathbf{C}_{\mathbf{x}}(k)$ and $\mathbf{C}_{\mathbf{y}}(k)$ depend upon the contour. Therefore, using this aggregation relationship the unmeasurable top level goal is now approximated by a combination of measurable bottom level states. As can be seen in equation (14), the top level error automatically goes to zero if the bottom level errors are driven to zero. However, bottom level errors are unavoidable during transient phases. It will be seen that emphasizing contour error will allow the axes to be coordinated such that contour error is reduced even during these phases. At these points top and bottom goals are competing objectives and it is desirable for both to be small. In fact, the bottom level goal results in preventing the deviation of each axis from its reference and the top level goal synchronizes the axes and ensures the relative movement of the axes result in a trajectory closer to the desired trajectory.

The next step is to formulate and solve an optimal tracking control problem as outlined in [37] with a modified cost function. At this point the top level goal is approximated using the aggregation relationship and included in the cost function

$$J_b = \frac{1}{2}\sum_{k=1}^{\infty} L_b(k) \tag{15}$$

where

$$L_b(k)=\frac{1}{2}\begin{Bmatrix}\left[\mathbf{C}(k)\mathbf{x}_\mathbf{b}(k)-\varepsilon_r(k)\right]^{\mathrm{T}} q\left[\mathbf{C}(k)\mathbf{x}_\mathbf{b}(k)-\varepsilon_r(k)\right]\\ +\mathbf{u}_\mathbf{b}^{\mathrm{T}}(k)\mathbf{R}_\mathbf{b}\mathbf{u}_\mathbf{b}(k)+\mathbf{x}_\mathbf{b}^{\mathrm{T}}(k)\mathbf{Q}_\mathbf{b}\mathbf{x}_\mathbf{b}(k)\end{Bmatrix} \tag{16}$$

and ε_r is the reference contour error, which is zero. In equation (16) the first term maintains the aggregation relationship between the top and bottom levels. The second and third terms are used to penalize the control usage and state deviations, respectively, at the bottom level. The Hamiltonian at the bottom level is

$$H_b(k)=L_b(k)+\boldsymbol{\lambda}_\mathbf{b}^{\mathrm{T}}(k+1)\left[\mathbf{A}_\mathbf{b}\mathbf{x}_\mathbf{b}(k)+\mathbf{B}_\mathbf{b}\mathbf{u}_\mathbf{b}(k)\right] \tag{17}$$

Taking the derivative of the Hamiltonian with respect to $\mathbf{x}_\mathbf{b}(k)$ and setting $\varepsilon_r(k)=0$, the Lagrange multiplier is

$$\boldsymbol{\lambda}_\mathbf{b}(k)=\left[\mathbf{C}^{\mathrm{T}}(k)q\,\mathbf{C}(k)+\mathbf{Q}_\mathbf{b}\right]\mathbf{x}_\mathbf{b}(k)+\mathbf{A}_\mathbf{b}^{\mathrm{T}}\boldsymbol{\lambda}_\mathbf{b}(k+1) \tag{18}$$

Taking the partial derivative of equation (17) with respect to $\mathbf{u}_\mathbf{b}(k)$, equating the result to zero, and rearranging gives the optimal control law

$$\mathbf{u}_\mathbf{b}(k)=-\mathbf{R}_\mathbf{b}^{-1}\mathbf{B}_\mathbf{b}^{\mathrm{T}}\boldsymbol{\lambda}_\mathbf{b}(k+1) \tag{19}$$

Substituting $\mathbf{u}_\mathbf{b}(k)$ from equation (19) into equation (12) results in

$$\mathbf{x}_\mathbf{b}(k+1)=\mathbf{A}_\mathbf{b}\mathbf{x}_\mathbf{b}(k)-\mathbf{B}_\mathbf{b}\mathbf{R}_\mathbf{b}^{-1}\mathbf{B}_\mathbf{b}^{\mathrm{T}}\boldsymbol{\lambda}_\mathbf{b}(k+1) \tag{20}$$

Now it is assumed that the Lagrangian multiplier can be expressed as

$$\boldsymbol{\lambda}_\mathbf{b}(k)=\mathbf{P}_\mathbf{b}(k)\mathbf{x}_\mathbf{b}(k) \tag{21}$$

where $\mathbf{P}_\mathbf{b}(k)$ is a positive definite, nonsingular matrix. Substituting equation (21) into equation (18) and (20) and rearranging, the following Ricatti equation is derived

$$\mathbf{P}_\mathbf{b}(k)=\mathbf{C}^{\mathrm{T}}(k)q\,\mathbf{C}(k)+\mathbf{Q}_\mathbf{b}+\mathbf{A}_\mathbf{b}^{\mathrm{T}}\mathbf{P}_\mathbf{b}(k+1)\left(\mathbf{I}+\mathbf{B}_\mathbf{b}\mathbf{R}_\mathbf{b}^{-1}\mathbf{B}_\mathbf{b}^{\mathrm{T}}\mathbf{P}_\mathbf{b}(k+1)\right)^{-1}\mathbf{A}_\mathbf{b} \tag{22}$$

The matrix $\mathbf{P_b}(k)$ is found from solving equation (22). As shown in the cost function in equation (15), an infinite horizon optimal control formulation is used to find the optimal signal $\mathbf{u_b}(k)$. Therefore, the steady state value of $\mathbf{P_b}(k)$, denoted $\overline{\mathbf{P}}_\mathbf{b}$, is used to solve the above Ricatti equation. Given $\mathbf{A_b}$, $\mathbf{B_b}$, $\mathbf{Q_b}$, $\mathbf{R_b}$, q, and $\mathbf{C}(k)$, the term $\overline{\mathbf{P}}_\mathbf{b}$ can be calculated off–line. If the ranges of variations in c_x and c_y are known, curves can be fit to the entries of $\overline{\mathbf{P}}_\mathbf{b}$ over the c_x and c_y ranges. These curves are then used for online implementation to increase computational efficiency. Knowing the time history of $\overline{\mathbf{P}}_\mathbf{b}$, the optimal control signal can be expressed as

$$\mathbf{u}_\mathbf{b}(k) = -\mathbf{K}_\mathbf{b}\mathbf{x}_\mathbf{b}(k) \tag{23}$$

where the control gain is

$$\mathbf{K}_\mathbf{b} = \left[\mathbf{R}_\mathbf{b} + \mathbf{B}_\mathbf{b}^{\mathrm{T}}\overline{\mathbf{P}}_\mathbf{b}\mathbf{B}_\mathbf{b}\right]^{-1}\mathbf{B}_\mathbf{b}^{\mathrm{T}}\overline{\mathbf{P}}_\mathbf{b}\mathbf{A}_\mathbf{b} \tag{24}$$

The physical control signals are found by solving the following equation for $u_x(k)$ and $u_y(k)$

$$\begin{aligned}\begin{bmatrix} b_{x1}u_x(k) \\ b_{y1}u_y(k) \end{bmatrix} = &\begin{bmatrix} r_x(k+1) + a_{x1}r_x(k) + a_{x2}\,r_x(k-1) + a_{x3}r_x(k-2) \\ r_y(k+1) + a_{y1}r_y(k) + a_{y2}\,r_y(k-1) + a_{y3}r_y(k-2) \end{bmatrix} + \\ &\mathbf{K}_\mathbf{b}\mathbf{x}_\mathbf{b}(k) - \begin{bmatrix} b_{x2}u_x(k-1) + b_{x3}u_x(k-2) \\ b_{y2}u_y(k-1) + b_{y3}u_y(k-2) \end{bmatrix}\end{aligned} \tag{25}$$

Note that the control signals require the reference positions at the next iteration, which are typically known. Fig. 2 shows a block diagram of the proposed controller. Based on equations (22) and (24), in Fig. 2 the controller gains are a function of $\mathbf{C}(k)$, which is a function of the desired trajectory and, for complex trajectories, the axial errors.

3. Experimental results and discussion

In this section experiments that explore the performance of the proposed hierarchical optimal contour control methodology are presented. Five experiments for a diamond contour and five experiments for a freeform contour are investigated on a table top CNC machine (Fig. 1). To generate the reference trajectories a constant velocity interpolator is used with a reference velocity of 8 mm/s. The linear axis model parameters are $\tau_x = 9.943\times10^{-3}$ s, $\tau_y = 1.044\times10^{-2}$ s, $K_x = 1.882$ (mm/s)/V, and $K_y = 1.764$ (mm/s)/V. The sample period is 1 ms and the control signals are saturated at ±10 V. The axial positions are measured by encoders with resolutions of 0.1075 μm. Here $\mathbf{R_b} = r_b\mathbf{I}_2$ where $r_b = 8$ for all experiments and the weighting matrices $\mathbf{Q_b} = q_b\mathbf{I}_6$ and q are varied. It has been experimentally determined that for the system to be stable neither q_b nor q can be more than two orders of magnitude greater than r_b. On the other hand, if q_b or q are more than four orders of magnitude smaller than the coefficient of r_b, no noticeable difference in performance can be detected.

First, diamond contours are tested. The contour error for a line segment is

$$\varepsilon(k) = \frac{l_y}{L}\mathbf{e_x}(k) - \frac{l_x}{L}\mathbf{e_y}(k) = \begin{bmatrix} 0 & 0 & c_x & 0 & 0 & c_y \end{bmatrix}\mathbf{x_b}(k) \tag{26}$$

where $c_x = \frac{l_y}{L}$, $c_y = -\frac{l_x}{L}$, l_x and l_y are the lengths of travel of the x and y axes, respectively, and L is the total length of travel. For each line segment the parameters c_x and c_y are constant, hence, the matrix $\bar{\mathbf{P}}_\mathbf{b}$ is constant. Five cases are presented, each with a different value of q/q_b. To increase the significance of contour error regulation, as

compared to axial error regulation, the ratio q/q_b is increased from 10^{-2} in Case I, where the axial tracking requirements are weighted more heavily than the contour error requirement, to 100 in Case V, where the top level contour error requirement is weighted more heavily than the axial tracking requirements. The weighting matrices for Cases I–V are listed in Table 1. In order to verify the repeatability of the controller performance, each experiment is conducted five times. The reference velocity for Cases I–V is 8 mm/s. Fig. 3 shows a schematic of the diamond contour. In Fig. 4 a comparison of the maximum transient errors is presented with the error bars depicting the error standard deviations centered around the average value for each case. It can be seen that as the emphasis on the contour error (i.e., q/q_b) increases, the maximum transient contour error generally decreases while the maximum transient axial errors generally increase. In fact, when the ratio q/q_b is increased, the higher level controller causes the axes to deviate from their reference values in such a way as to reduce the contour error. However, it can be seen from Fig. 4 that even with the maximum emphasis on contour, the contour error at the corner is still considerable. This is due to control signal saturation. The effect of increasing the emphasis on contour error in the right corner of the diamond contour is illustrated in Fig. 5. In the right corner of the diamond contour the controller reduces the contour error by intelligently increasing e_y.

Fig. 6 shows the transient responses for Cases I–V at the right corner. It can be seen that as q/q_{bot} increases, the amount of overshoot decreases, resulting in lower contour errors and, for $q/q_b = 100$ the axes move backwards to reduce the contour error. In this situation, a high emphasis on contour error reduction results in a sharp reaction to unsynchronized motion. Fig. 7 presents the axis trajectories at the top corner. It should be

noted that the reason for unsynchronized axis motion at the corners is that one of the axes always changes direction at these points. Therefore, the unsynchronized motion at the corners is related to the speed of the axis that is changing direction. While at the right corner the x axis speed changes from 7.51 mm/s to –7.51 mm/s, at the top corner the y axis speed changes from 2.73 mm/s to –2.73 mm/s. Therefore, as can be seen in Fig. 7, the resulting contour error at the top corner is not as significant as the contour error at the right corner. As shown in Fig. 8, the controller produces steady–state errors that are within two sensor resolutions for all five cases. It can be seen in Fig. 8 that during the steady state, changing the emphasis does not significantly affect the axial and contour errors since these errors are within two encoder resolutions. Fig. 9 depicts a detailed view of the experimental results for Case V. As can be seen in Fig. 9, the control signals often saturate when an axis changes direction, causing the system to be unable to reduce the contour error any further. However, it is evident that the steady state error is still within two encoder resolutions.

Freeform contours are investigated next. A schematic of the freeform contour used for the experimental studies conducted in this paper is shown in Fig. 10. For these contours, the radius of curvature constantly changes along the contour and, therefore, to maintain a constant linear velocity, the angular velocity is constantly changing. The contour error for a freeform contour is approximated at each instant by a contour error for a circle with a radius equal to the instantaneous radius of curvature,

$$\begin{aligned}\varepsilon(k) &= \left\{\sin\left[\theta(k)\right] + \frac{e_x(k)}{2\rho(k)}\right\} e_x(k) - \left\{\cos\left[\theta(k)\right] + \frac{e_y(k)}{2\rho(k)}\right\} e_y(k) \\ &= \begin{bmatrix} 0 & 0 & c_x(k) & 0 & 0 & c_y(k) \end{bmatrix} \mathbf{x_b}(k)\end{aligned} \tag{27}$$

where c_x and c_y vary and are functions of θ (i.e., the angle of the instantaneous reference velocity vector from the positive x axis), the instantaneous error, and the instantaneous radius of curvature, which is

$$\rho(t) = \frac{\left(\left[r_x'(t)\right]^2 + \left[r_y'(t)\right]^2\right)^{1.5}}{\left|r_x'(t)r_y''(t) - r_y'(t)r_x''(t)\right|} \tag{28}$$

where $r_x'(t) = \frac{dr_x(t)}{dt}$, $r_y'(t) = \frac{dr_y(t)}{dt}$, $r_x''(t) = \frac{dr_x^2(t)}{d^2t}$, and $r_y''(t) = \frac{dr_y^2(t)}{d^2t}$. To avoid the computational burden of solving the Ricatti equation at each iteration, an approximation of the matrix $\bar{\mathbf{P}}_\mathbf{b}$ as a function of c_x and c_y is developed. The parameters c_x and c_y are within the range –1.5 to 1.5. Therefore, a mesh is generated in this range and at each node $\bar{\mathbf{P}}_\mathbf{b}$ is calculated using the *dare* function in Matlab. Curves are fit to the calculated data and the coefficients of the curves are saved and used to calculate the entries of $\bar{\mathbf{P}}_\mathbf{b}$ at each iteration online. The weighting matrices for each case are given in Table 2. Fig. 11 shows the maximum value of the transient responses with error bars depicting the error standard deviations centered around the average value for each case. As q/q_b increases from 10^{-2} to 100, the maximum axial errors generally increase and the maximum contour error generally decreases. In Fig. 12 a comparison of steady–state errors is presented. It should be noted that although the trajectory's direction of motion is constantly changing for all five cases, the steady–state errors are still within two sensor resolutions. As the steady state errors are close to the sensor resolution, changing the emphasis from axial to contour error does not significantly affect the steady state errors. A detailed view of the results for Case VI is presented in Fig. 13. The spikes that appear in the axial and contour

errors are a result of one of the axes changing direction and are regulated in an optimum manner with more emphasis on the axial error (i.e., $q = 10^{-3}$ and $q_b = 0.1$). The experimental results for the freeform contours show the hierarchical contour control method is also valid for complex contours where the angular velocity constantly varies.

4. Summary and conclusions

In this paper, a new hierarchical contour control methodology for motion control systems having multiple objectives was proposed and experimentally implemented. The objectives are allocated into two levels of decision making i.e., a higher level for axis synchronization and a bottom level for individual axis tracking. To apply the proposed methodology, the axis dynamics are converted into the error domain and the Internal Model Principle, coupled with optimal control, is used to simultaneously satisfy the top level goal (i.e., zero contour error) and the bottom level goals (i.e., zero axial errors and minimal control usage). The top level goal is propagated to the physical linear axis level by an aggregation relationship. Optimal control techniques are used to weight the relative importance between axial and contour errors.

Experimental results on a table top CNC machine demonstrate the excellent tracking capability of this method for diamond and freeform contours. For both contours, the steady state errors are approximately 0.2 μm, which are within two encoder resolutions, indicating the excellent tracking and disturbance rejection capabilities of the controller. To test the performance of the controller for different relative weightings of the top and bottom level goals, five cases were conducted, where q/q_{bot} increased from

10^{-2} (i.e., high weight on axial errors) to 100 (i.e., high weight on contour error). It was found that the transient errors generally decreased when the contour error was weighted more heavily than the axial errors for both contours. On the other hand, the steady state errors were independent of the relative weighting. This is due to the fact that for both cases the steady state error was within two encoder resolutions. Two axes of a table top CNC machine was used in this paper as a test bed to experimentally implement and analyze the proposed methodology. However, the hierarchical optimal contour control methodology can be extended to any motion system with multiple axes whose motion must be coordinated. To extend the methodology to more than two axes, a new contour error formulation and possibly tool orientation error formulation would need to be derived and the error dynamics of the additional axes would need to be incorporated.

Acknowledgement

The authors wish to acknowledge the financial support for this work from the Intelligent Systems Center at the Missouri University of Science and Technology.

Appendix A. Stability proof of the proposed controller

In order to investigate the global asymptotic tracking stability of the overall closed-loop system, a Layapunov function candidate is considered as

$$V\left(\mathbf{x}_{\mathbf{b}}\left(k\right)\right)=\mathbf{x}_{\mathbf{b}}^{\mathrm{T}}\left(k\right)\overline{\mathbf{P}}_{\mathbf{b}}{}^{k}\mathbf{x}_{\mathbf{b}}\left(k\right) \tag{29}$$

where $V(0) = 0$ and $\overline{\mathbf{P}}_{\mathbf{b}}^{\,k} = \overline{\mathbf{P}}_{\mathbf{b}}\left(C(k)\right)$ is the steady state solution of the reccuti equation with respect to $C(k)$. Because $\overline{\mathbf{P}}_{\mathbf{b}}^{\,k}$ is a positive definite matrix, $\forall \mathbf{x}_{\mathrm{b}}(k) \neq 0,\ V\left(\mathbf{x}_{\mathrm{b}}(k)\right) > 0$. The first order forward difference of $V\left(\mathbf{x}_{\mathrm{b}}(k)\right)$ is

$$\Delta V(k) = V\left(\mathbf{x}_{\mathbf{b}}(k+1)\right) - V\left(\mathbf{x}_{\mathbf{b}}(k)\right) = \mathbf{x}_{\mathbf{b}}^{\mathrm{T}}(k+1)\,\overline{\mathbf{P}}_{\mathbf{b}}^{\,k+1}\mathbf{x}_{\mathbf{b}}(k+1) - \mathbf{x}_{\mathbf{b}}^{\mathrm{T}}(k)\,\overline{\mathbf{P}}_{\mathbf{b}}^{\,k}\mathbf{x}_{\mathbf{b}}(k) \quad (30)$$

Evaluating $\Delta V(k)$ along the error system equation

$$\begin{aligned}\Delta V(k) = \left[\mathbf{A}_{\mathbf{b}}\mathbf{x}_{\mathbf{b}}(k) + \mathbf{B}_{\mathbf{b}}\mathbf{u}_{\mathbf{b}}(k)\right]^{\mathrm{T}}\overline{\mathbf{P}}_{\mathbf{b}}^{\,k+1}\left[\mathbf{A}_{\mathbf{b}}\mathbf{x}_{\mathbf{b}}(k) + \mathbf{B}_{\mathbf{b}}\mathbf{u}_{\mathbf{b}}(k)\right] - \\ \mathbf{x}_{\mathbf{b}}^{\mathrm{T}}(k)\,\overline{\mathbf{P}}_{\mathbf{b}}^{\,k}\mathbf{x}_{\mathbf{b}}(k)\end{aligned} \quad (31)$$

Expanding equation (31)

$$\begin{aligned}\Delta V = {} & \mathbf{x}_{\mathbf{b}}^{\mathrm{T}}(k)\,\mathbf{A}_{\mathbf{b}}^{\mathrm{T}}\overline{\mathbf{P}}_{\mathbf{b}}^{\,k+1}\mathbf{A}_{\mathbf{b}}\mathbf{x}_{\mathbf{b}}(k) - \mathbf{x}_{\mathbf{b}}^{\mathrm{T}}(k)\,\overline{\mathbf{P}}_{\mathbf{b}}^{\,k}\mathbf{x}_{\mathbf{b}}(k) + \\ & \mathbf{x}_{\mathbf{b}}^{\mathrm{T}}(k)\,\mathbf{A}_{\mathbf{b}}^{\mathrm{T}}\overline{\mathbf{P}}_{\mathbf{b}}^{\,k+1}\mathbf{B}_{\mathbf{b}}\mathbf{u}_{\mathbf{b}}(k) + \mathbf{u}_{\mathbf{b}}^{\mathrm{T}}(k)\,\mathbf{B}_{\mathbf{b}}^{\mathrm{T}}\overline{\mathbf{P}}_{\mathbf{b}}^{\,k+1}\mathbf{A}_{\mathbf{b}}\mathbf{x}_{\mathbf{b}}(k) + \\ & \mathbf{u}_{\mathbf{b}}^{\mathrm{T}}(k)\,\mathbf{B}_{\mathbf{b}}^{\mathrm{T}}\overline{\mathbf{P}}_{\mathbf{b}}^{\,k+1}\mathbf{B}_{\mathbf{b}}\mathbf{u}_{\mathbf{b}}(k)\end{aligned} \quad (32)$$

Since $\overline{\mathbf{P}}_{\mathbf{b}}^{\,K}$ is symmetric and $\mathbf{u}_{\mathbf{b}}^{\mathrm{T}}(k)\,\mathbf{B}_{\mathbf{b}}^{\mathrm{T}}\overline{\mathbf{P}}_{\mathbf{b}}^{\,k+1}\mathbf{A}_{\mathbf{b}}\mathbf{x}_{\mathbf{b}}(k)$ is scalar,

$$\begin{aligned}\Delta V = {} & \mathbf{x}_{\mathbf{b}}^{\mathrm{T}}(k)\,\mathbf{A}_{\mathbf{b}}^{\mathrm{T}}\overline{\mathbf{P}}_{\mathbf{b}}^{\,k+1}\mathbf{A}_{\mathbf{b}}\mathbf{x}_{\mathbf{b}}(k) - \mathbf{x}_{\mathbf{b}}^{\mathrm{T}}(k)\,\overline{\mathbf{P}}_{\mathbf{b}}^{\,k}\mathbf{x}_{\mathbf{b}}(k) + \\ & 2\mathbf{x}_{\mathbf{b}}^{\mathrm{T}}(k)\,\mathbf{A}_{\mathbf{b}}^{\mathrm{T}}\overline{\mathbf{P}}_{\mathbf{b}}^{\,k+1}\mathbf{B}_{\mathbf{b}}\mathbf{u}_{\mathbf{b}}(k) + \mathbf{u}_{\mathbf{b}}^{\mathrm{T}}(k)\,\mathbf{B}_{\mathbf{b}}^{\mathrm{T}}\overline{\mathbf{P}}_{\mathbf{b}}^{\,k+1}\mathbf{B}_{\mathbf{b}}\mathbf{u}_{\mathbf{b}}(k)\end{aligned} \quad (33)$$

In order to simplify equation (33) the matrix inversion lemma [42] is implemented to the reccuti equation in steady state condition which results in

$$\overline{\mathbf{P}}_{\mathbf{b}}^{\,k} = \mathbf{Q}(k) + \mathbf{A}_{\mathbf{b}}^{\mathrm{T}}\overline{\mathbf{P}}_{\mathbf{b}}^{\,k}\mathbf{A}_{\mathbf{b}} - \mathbf{A}_{\mathbf{b}}^{\mathrm{T}}\overline{\mathbf{P}}_{\mathbf{b}}^{\,k}\mathbf{B}_{\mathrm{b}}\left(\mathbf{B}_{\mathrm{b}}^{\mathrm{T}}\overline{\mathbf{P}}_{\mathbf{b}}^{\,k}\mathbf{B}_{\mathrm{b}} + \mathbf{R}_{\mathrm{b}}\right)^{-1}\mathbf{B}_{\mathrm{b}}^{\mathrm{T}}\overline{\mathbf{P}}_{\mathbf{b}}^{\,k}\mathbf{A}_{\mathbf{b}} \quad (34)$$

Substituting for $\overline{\mathbf{P}}_{\mathbf{b}}^{\,K}$ from equation (34), into the second term of equation (33) and after some simplifications,

$$\begin{aligned}\Delta V = {} & \mathbf{x}_\mathbf{b}^\mathrm{T}(k)\mathbf{A}_\mathbf{b}^\mathrm{T}\overline{\mathbf{P}}_\mathbf{b}^{\,k}\mathbf{B}_\mathbf{b}\left(\mathbf{\Phi}^k\right)^{-1}\mathbf{B}_\mathbf{b}^\mathrm{T}\overline{\mathbf{P}}_\mathbf{b}^{\,k}\mathbf{A}_\mathbf{b}\mathbf{x}_\mathbf{b}(k)-\mathbf{x}_\mathbf{b}^\mathrm{T}(k)\mathbf{Q}(k)\mathbf{x}_\mathbf{b}(k)\\ & +\mathbf{x}_\mathbf{b}^\mathrm{T}(k)\mathbf{A}_\mathbf{b}^\mathrm{T}\left(\overline{\mathbf{P}}_\mathbf{b}^{\,k+1}-\overline{\mathbf{P}}_\mathbf{b}^{\,k}\right)\mathbf{A}_\mathbf{b}\mathbf{x}_\mathbf{b}(k)\\ & +2\mathbf{x}_\mathbf{b}^\mathrm{T}(k)\mathbf{A}_\mathbf{b}^\mathrm{T}\overline{\mathbf{P}}_\mathbf{b}^{\,k+1}\mathbf{B}_\mathbf{b}\mathbf{u}_\mathbf{b}(k)+\mathbf{u}_\mathbf{b}^\mathrm{T}(k)\mathbf{B}_\mathbf{b}^\mathrm{T}\overline{\mathbf{P}}_\mathbf{b}^{\,k+1}\mathbf{B}_\mathbf{b}\mathbf{u}_\mathbf{b}(k)\end{aligned} \tag{35}$$

where $\mathbf{\Phi}^k=\mathbf{B}_\mathbf{b}^\mathrm{T}\overline{\mathbf{P}}_\mathbf{b}^{\,k}\mathbf{B}_\mathbf{b}+\mathbf{R}_\mathbf{b}$ and is symmetric and nonsingular.

From equations (23) and (24) the control signal can be expressed by

$$\mathbf{u}_\mathbf{b}(k)=-\left(\mathbf{\Phi}^k\right)^{-1}\mathbf{B}_\mathbf{b}^\mathrm{T}\overline{\mathbf{P}}_\mathbf{b}^{\,k}\mathbf{A}_\mathbf{b}\mathbf{x}_\mathbf{b}(k) \tag{36}$$

Now replacing for control signal from equation (36) into the fourth and fifth terms of equation (35) and after some simplifications,

$$\Delta V=-\mathbf{x}_\mathbf{b}^\mathrm{T}(k)\begin{pmatrix}-\mathbf{A}_\mathbf{b}^\mathrm{T}\overline{\mathbf{P}}_\mathbf{b}^{\,k}\mathbf{B}_\mathbf{b}\left(\mathbf{\Phi}^k\right)^{-1}\left(\mathbf{B}_\mathbf{b}^\mathrm{T}\overline{\mathbf{P}}_\mathbf{b}^{\,k+1}\mathbf{B}_\mathbf{b}\right)\left(\mathbf{\Phi}^k\right)^{-1}\mathbf{B}_\mathbf{b}^\mathrm{T}\overline{\mathbf{P}}_\mathbf{b}^{\,k}\mathbf{A}_\mathbf{b}\\ -\mathbf{A}_\mathbf{b}^\mathrm{T}\left(\overline{\mathbf{P}}_\mathbf{b}^{\,k}-2\overline{\mathbf{P}}_\mathbf{b}^{\,k+1}\right)\mathbf{B}_\mathbf{b}\left(\mathbf{\Phi}^k\right)^{-1}\mathbf{B}_\mathbf{b}^\mathrm{T}\overline{\mathbf{P}}_\mathbf{b}^{\,k}\mathbf{A}_\mathbf{b}\\ -\mathbf{A}_\mathbf{b}^\mathrm{T}\left(\overline{\mathbf{P}}_\mathbf{b}^{\,k+1}-\overline{\mathbf{P}}_\mathbf{b}^{\,k}\right)\mathbf{A}_\mathbf{b}+\mathbf{Q}(k)\end{pmatrix}\mathbf{x}_\mathbf{b}(k) \tag{37}$$

Therefore, when $\mathbf{C}(k)$ is variable, as long as the matrix $\mathbf{M}^k=\begin{pmatrix}-\mathbf{A}_\mathbf{b}^\mathrm{T}\overline{\mathbf{P}}_\mathbf{b}^{\,k}\mathbf{B}_\mathbf{b}\left(\mathbf{\Phi}^k\right)^{-1}\left(\mathbf{B}_\mathbf{b}^\mathrm{T}\overline{\mathbf{P}}_\mathbf{b}^{\,k+1}\mathbf{B}_\mathbf{b}\right)\left(\mathbf{\Phi}^k\right)^{-1}\mathbf{B}_\mathbf{b}^\mathrm{T}\overline{\mathbf{P}}_\mathbf{b}^{\,k}\mathbf{A}_\mathbf{b}+\\ \mathbf{A}_\mathbf{b}^\mathrm{T}\left(2\overline{\mathbf{P}}_\mathbf{b}^{\,k+1}-\overline{\mathbf{P}}_\mathbf{b}^{\,k}\right)\mathbf{B}_\mathbf{b}\left(\mathbf{\Phi}^k\right)^{-1}\mathbf{B}_\mathbf{b}^\mathrm{T}\overline{\mathbf{P}}_\mathbf{b}^{\,k}\mathbf{A}_\mathbf{b}-\mathbf{A}_\mathbf{b}^\mathrm{T}\left(\overline{\mathbf{P}}_\mathbf{b}^{\,k+1}-\overline{\mathbf{P}}_\mathbf{b}^{\,k}\right)\mathbf{A}_\mathbf{b}+\mathbf{Q}(k)\end{pmatrix}$ is positive definite ΔV is negative definite indicating the system is asymptotically stable. And since $\forall\mathbf{x}_\mathbf{b}(k)\in\mathbf{R},\ if\ \left\|\mathbf{x}_\mathbf{b}(k)\right\|\to\infty,\ V\left(\mathbf{x}_\mathbf{b}(k)\right)\to\infty$, the system is globally asymptotically stable Therefore when for a free form contour the designer should always check if the $\mathbf{M}^k$ satisfy the mentioned condition before implementing the controller. However when $\mathbf{C}(k)=\mathbf{C}(k+1)$ therefore $\overline{\mathbf{P}}_\mathbf{b}^{\,k}=\overline{\mathbf{P}}_\mathbf{b}^{\,k+1}$ and as a result ΔV will be simplified to

$$\Delta V = -\mathbf{x}_\mathbf{b}^\mathrm{T}(k)\begin{pmatrix} -\mathbf{A}_\mathbf{b}^\mathrm{T}\overline{\mathbf{P}}_\mathbf{b}^{\,k}\mathbf{B}_\mathbf{b}\left(\boldsymbol{\Phi}^k\right)^{-1}\left(\mathbf{B}_\mathbf{b}^\mathrm{T}\overline{\mathbf{P}}_\mathbf{b}^{\,k}\mathbf{B}_\mathbf{b}\right)\left(\boldsymbol{\Phi}^k\right)^{-1}\mathbf{B}_\mathbf{b}^\mathrm{T}\overline{\mathbf{P}}_\mathbf{b}^{\,k}\mathbf{A}_\mathbf{b} \\ +\mathbf{A}_\mathbf{b}^\mathrm{T}\overline{\mathbf{P}}_\mathbf{b}^{\,k}\mathbf{B}_\mathbf{b}\left(\boldsymbol{\Phi}^k\right)^{-1}\mathbf{B}_\mathbf{b}^\mathrm{T}\overline{\mathbf{P}}_\mathbf{b}^{\,k}\mathbf{A}_\mathbf{b} \\ +\mathbf{Q}(k) \end{pmatrix}\mathbf{x}_\mathbf{b}(k) \tag{38}$$

Combining the first and second terms inside the parenthesis in equation (38) and substituting for $\mathbf{x}_\mathbf{b}^\mathrm{T}(k)\mathbf{A}_\mathbf{b}^\mathrm{T}\overline{\mathbf{P}}_\mathbf{b}^{\,k}\mathbf{B}_\mathbf{b}\left(\boldsymbol{\Phi}^k\right)^{-1}$ and $\left(\boldsymbol{\Phi}^k\right)^{-1}\mathbf{B}_\mathbf{b}^\mathrm{T}\overline{\mathbf{P}}_\mathbf{b}^{\,k}\mathbf{A}_\mathbf{b}\mathbf{x}_\mathbf{b}(k)$ from equation (36)

$$\Delta V = -\mathbf{u}_\mathbf{b}^\mathrm{T}(k)\mathbf{R}_\mathbf{b}\mathbf{u}_\mathbf{b}(k) - \mathbf{x}_\mathbf{b}^\mathrm{T}(k)\mathbf{Q}(k)\mathbf{x}_\mathbf{b}(k) < 0\ ,\ \forall \mathbf{x}_\mathbf{b}(k) \neq 0 \tag{39}$$

Therefore when $\mathbf{C}(k)$ is constant, ΔV is always negative definite and since $\forall \mathbf{x}_\mathbf{b}(k) \in \mathbf{R},\ if\ \left\|\mathbf{x}_\mathbf{b}(k)\right\| \to \infty,\ V\left(\mathbf{x}_\mathbf{b}(k)\right) \to \infty$, the system is always globally asymptotically stable.

References

[1] c.-y. C. Marvin h.-m. Cheng, ezzat g. Bakhoum and aniruddha mitra, "synchronization controller synthesis with the consideration of multi-resolution", *international journal of innovative computing, information and control*, 2009, vol. 3, no. 4(a), pp. 1025-1030.

[2] m. Tomizuka, "zero phase error tracking algorithm for digital control", *j. Dyn. Syst. Meas. Control.*, 1987, vol. 109, no. 1, pp. 65-68.

[3] y. Xiao, k. Zhu, and h. Choo liaw, "generalized synchronization control of multi-axis motion systems", *control engineering practice*, 2005, vol. 13, no. 7, pp. 809-819.

[4] y. Koren, "cross-coupled biaxial computer control for manufacturing systems", *asme journal of dynamic systems, measurement and control*, 1980, vol. 102, no. 4, pp. 265-272.

[5] d. Sun, "position synchronization of multiple motion axes with adaptive coupling control", *automatica*, 2003, vol. 39, no. 6, pp. 997-1005.

[6] p. Moore, and c. Chen, “fuzzy logic coupling and synchronised control of multiple independent servo-drives”, *control engineering practice*, 1995, vol. 3, no. 12, pp. 1697-1708.

[7] h. C. Lee, and g. J. Jeon, “a neuro controller for synchronization of two motion axes”, *international journal of intelligent systems*, 1998, vol. 13, no. 6, pp. 571-586.

[8] l. Feng, y. Koren, and j. Borenstein, “cross-coupling motion controller for mobile robots”, *ieee control systems magazine*, 1993, vol. 13, no. 6, pp. 35-43.

[9] j. H. Chin, and t. C. Lin, “cross-coupled precompensation method for the contouring accuracy of computer numerically controlled machine tools”, *international journal of machine tools and manufacture*, 1997, vol. 37, no. 7, pp. 947-967.

[10] h. C. Lee, and g. J. Jeon, “real-time compensation of two-dimensional contour error in cnc machine tools”, *ieee/asme international conference on advanced intelligent mechatronics*, atlanta, georgia, 1999, september 19-23, 1999.

[11] y.-t. Shih, c.-s. Chen, and a.-c. Lee, “a novel cross-coupling control design for bi-axis motion”, *international journal of machine tools and manufacture*, 2002, vol. 42, no. 14, pp. 1539-1548.

[12] j. H. Chin, y. M. Cheng, and j. H. Lin, “improving contour accuracy by fuzzy-logic enhanced cross-coupled precompensation method”, *robotics and computer-integrated manufacturing*, 2004, vol. 20, no. 1, pp. 65-76.

[13] m. Y. Cheng, k. H. Su, and s. F. Wang, “contour error reduction for free-form contour following tasks of biaxial motion control systems”, *robotics and computer-integrated manufacturing*, 2009, vol. 25, no. 2, pp. 323-333.

[14] k. H. Su, and m. Y. Cheng, “contouring accuracy improvement using cross-coupled control and position error compensator”, *international journal of machine tools and manufacture*, 2008, vol. 48, no. 12-13, pp. 1444-1453.

[15] y. Altintas, and m. Khoshdarregi, “contour error control of cnc machine tools with vibration avoidance”, *cirp annals-manufacturing technology*, 2012.

[16] s. Goto, m. Nakamura, and n. Kyura, “accurate contour control of mechatronic servo systems using gaussian networks”, *ieee transactions on industrial electronics*, 1996, vol. 43, no. 4, pp. 469-476.

[17] g. T. C. Chiu, and m. Tomizuka, “coordinated position control of multi-axis mechanical systems”, *asme journal of dynamic systems, measurement and control*, 1998, vol. 120, no. 3, pp. 389-393.

[18] h. C. Ho, j. Y. Yen, and s. S. Lu, “a decoupled path-following control algorithm based upon the decomposed trajectory error”, *international journal of machine tools and manufacture*, 1999, vol. 39, no. 10, pp. 1619-1630.

[19] s.-s. Yeh, and p.-l. Hsu, “design of precise multi-axis motion control systems”, *proceedings of 6th international workshop on advanced motion control*, 2000, 1 april.

[20] g. T. C. Chiu, and m. Tomizuka, “contouring control of machine tool feed drive systems: a task coordinate frame approach”, *ieee transactions on control systems technology*, 2001, vol. 9, no. 1, pp. 130-139.

[21] s. L. Chen, h. L. Liu, and s. C. Ting, “contouring control of biaxial systems based on polar coordinates”, *ieee/asme transactions on mechatronics*, 2002, vol. 7, no. 3, pp. 329-345.

[22] s. S. Yeh, and p. L. Hsu, “estimation of the contouring error vector for the cross-coupled control design”, *ieee/asme transactions on mechatronics*, 2002, vol. 7, no. 1, pp. 44-51.

[23] q. Zhong, y. Shi, j. Mo, and s. Huang, “a linear cross-coupled control system for high-speed machining”, *the international journal of advanced manufacturing technology*, 2002, vol. 19, no. 8, pp. 558-563.

[24] y. Koren, “control of machine tools”, *asme journal of mechanical design*, 1997, vol. 119, pp. 749-755.

[25] l. Tang, and r. G. Landers, “predictive contour control with adaptive feed rate”, *ieee/asme transactions on mechatronics*, 2012, vol. 17, no. 4, pp. 669-679.

[26] p. Ouyang, t. Dam, j. Huang, and w. Zhang, “contour tracking control in position domain”, *mechatronics*, 2012.

[27] z. Guo, c. Wang, k. Zhao, and y. Wang, “equal-status approach synchronization controller design method based on quantitative feedback theory for dual hydraulic motors driven flight simulators”, *computer design and applications (iccda), 2010 international conference on*, 2010.

[28] s. Jee, and y. Koren, “adaptive fuzzy logic controller for feed drives of a cnc machine tool”, *mechatronics*, 2004, vol. 14, no. 3, pp. 299-326.

[29] b. Chu, s. Kim, d. Hong, h.-k. Park, and j. Park, “optimal cross-coupled synchronizing control of dual-drive gantry system for a smd assembly machine”, *jsme international journal*, 2004, vol. 47 series c, no. 3, pp. 939-945.

[30] p. K. Kulkarni, and k. Srinivasan, “optimal contouring control of multi-axial feed drive servomechanisms”, *asme journal of engineering for industry*, 1989, vol. 111, no. 2, pp. 140-148.

[31] a. G. Ulsoy, and y. Koren, “control of machining processes”, *asme journal of dynamic systems, measurement, and control*, 1993, vol. 115, pp. 301-308.

[32] r. G. Landers, and s. N. Balakrishnan, “hierarchical optimal contour-position control of motion control systems”, *asme international mechanical engineering congress and exposition*, anaheim, california, 2004, november 13 – 19, 2004.

[33] y. Tang, r. G. Landers, and s. N. Balakrishnan, “hierarchical optimal force-position-contour control of machining processes”, *control engineering practice*, 2006, vol. 14, no. 8, pp. 909-922.

[34] g. Franklin, j. Powell, and a. Emami-naeini, "feedback control of dynamic systems", 3rd edition ed.: addison-wesley reading, 1994.

[35] k. Srinivasan, and t. C. Tsao, “machine tool feed drives and their control - a survey of the state of the art”, *asme journal of manufacturing science and engineering*, 1997, vol. 119, no. 4 part ii, pp. 743-748.

[36] y. Koren, and c. C. Lo, “variable-gain cross-coupling controller for contouring”, *cirp annals*, 1991, vol. 40, no. 1, pp. 371-374.

[37] f. Lewis, and v. Syrmos, "optimal control": wiley-interscience, 1995.

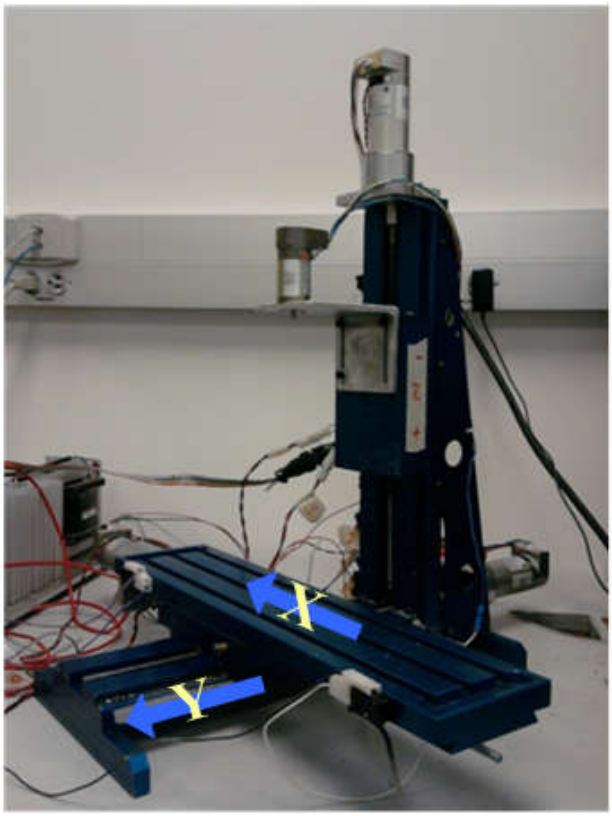

Fig. 1. Table top CNC machine.

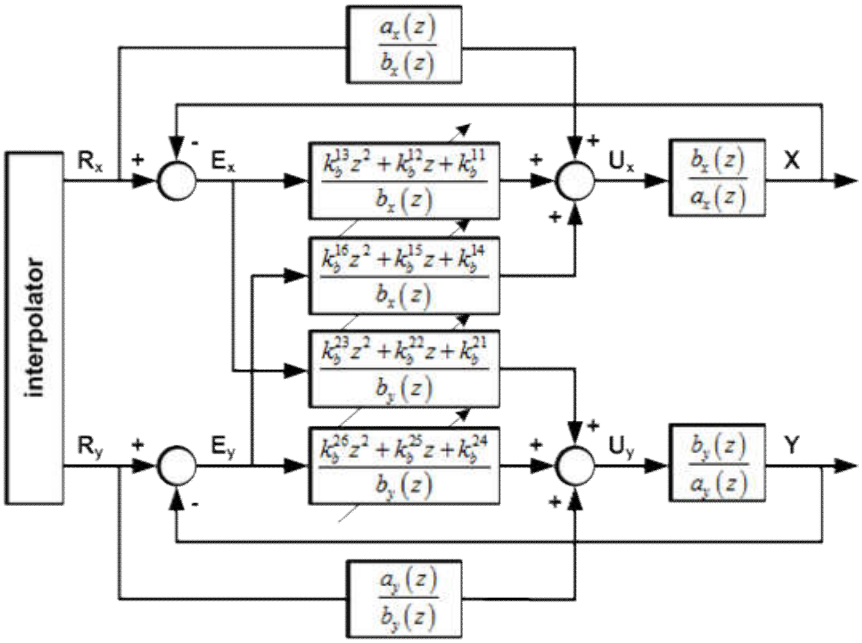

Fig. 2. Block diagram of the proposed controller.

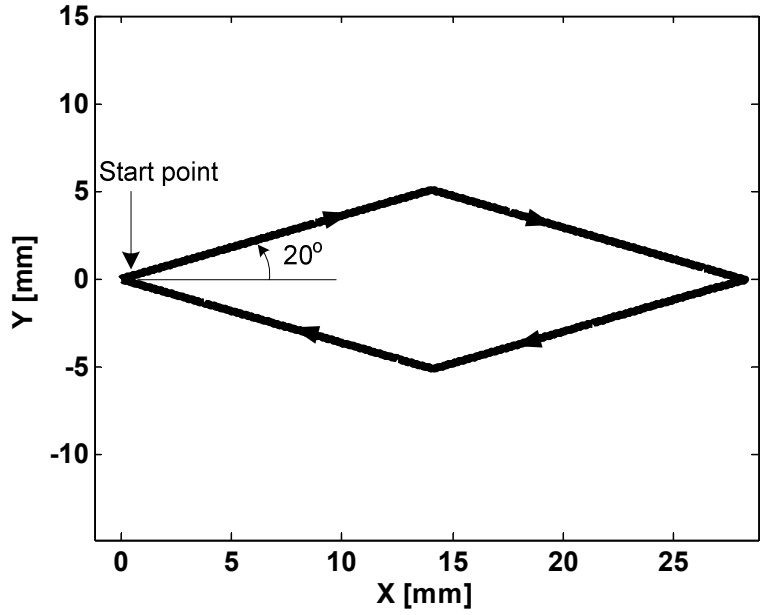

Fig. 3. Diamond contour schematic.

Table 1
Diamond Contour Cases.

Case	I	II	III	IV	V
q	10^{-3}	10^{-2}	0.1	0.1	0.1
q_b	0.1	0.1	0.1	10^{-2}	10^{-3}
q/q_b	10^{-2}	0.1	1	10	100

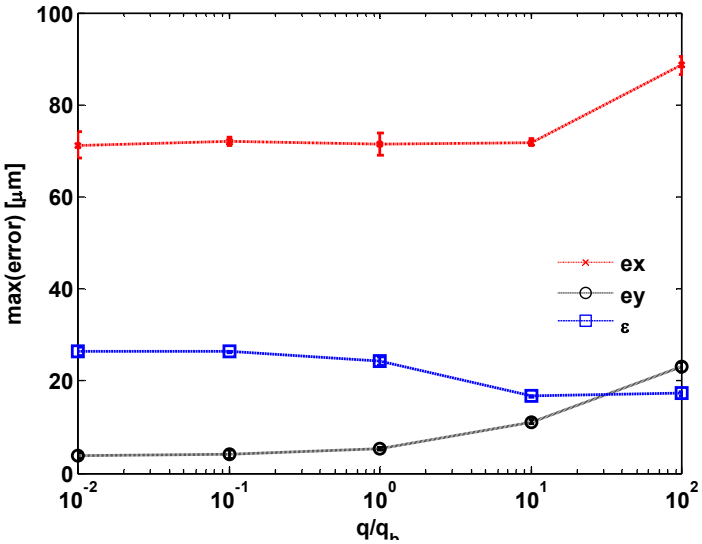

Fig. 4. Maximum transient errors for Cases I–V.

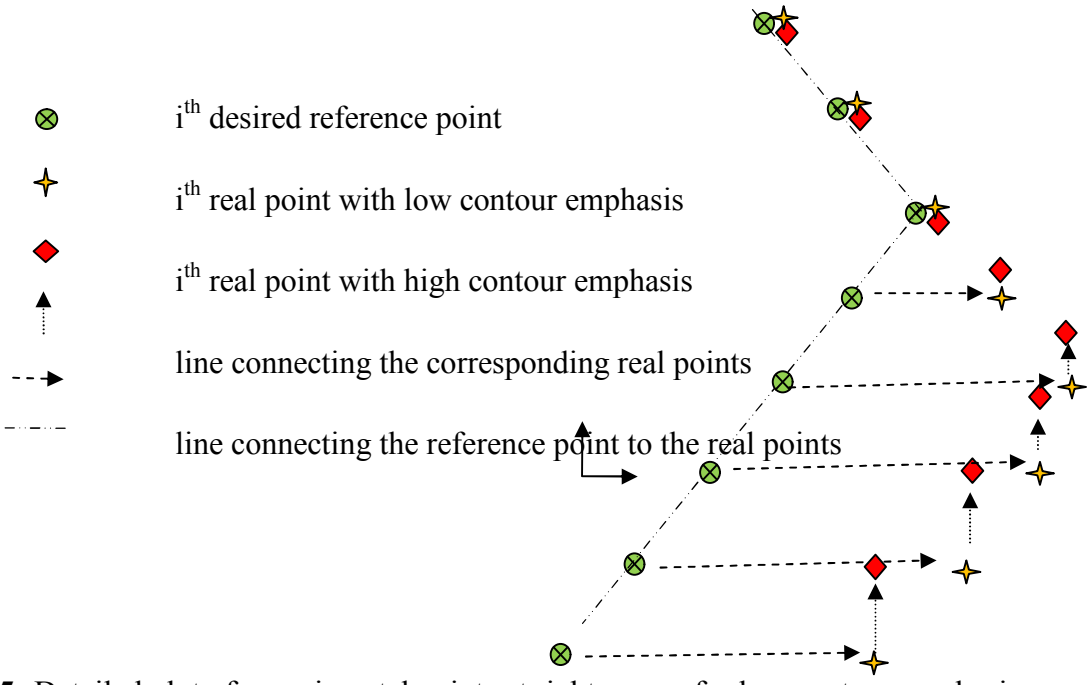

Fig. 5. Detailed plot of experimental points at right corner for low contour emphasis versus high contour emphasis.

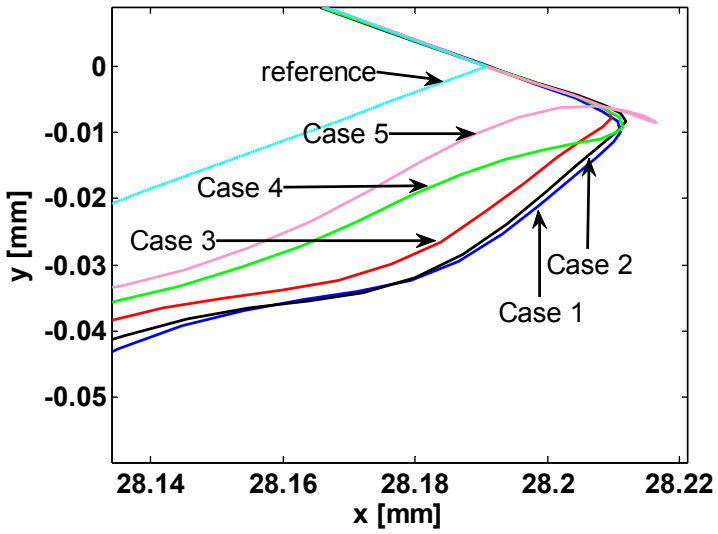

Fig. 6. Right corner transient responses for Cases I–V.

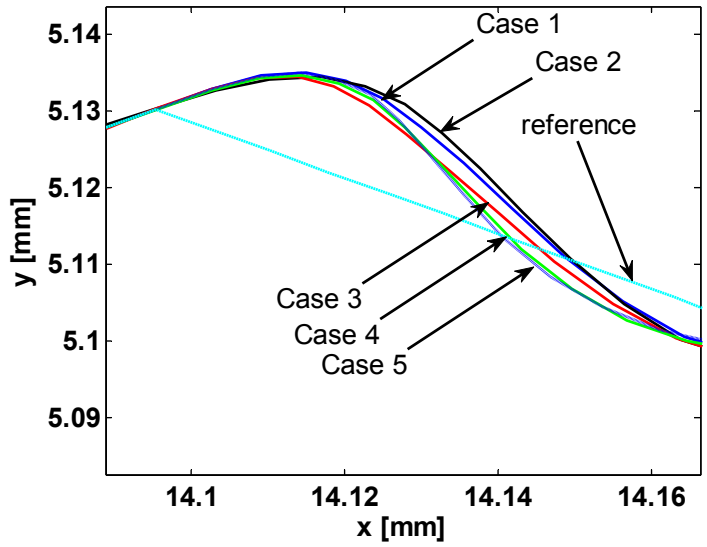

Fig. 7. Top corner transient responses for Cases I–V.

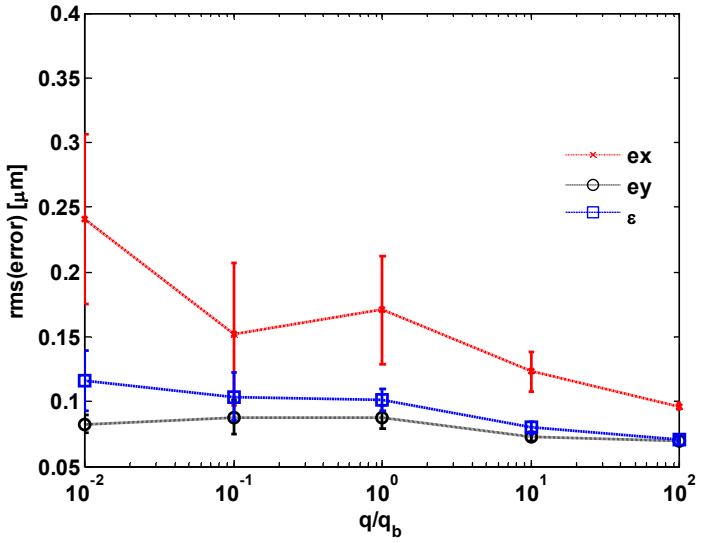

Fig. 8. Steady state errors for Cases I–V.

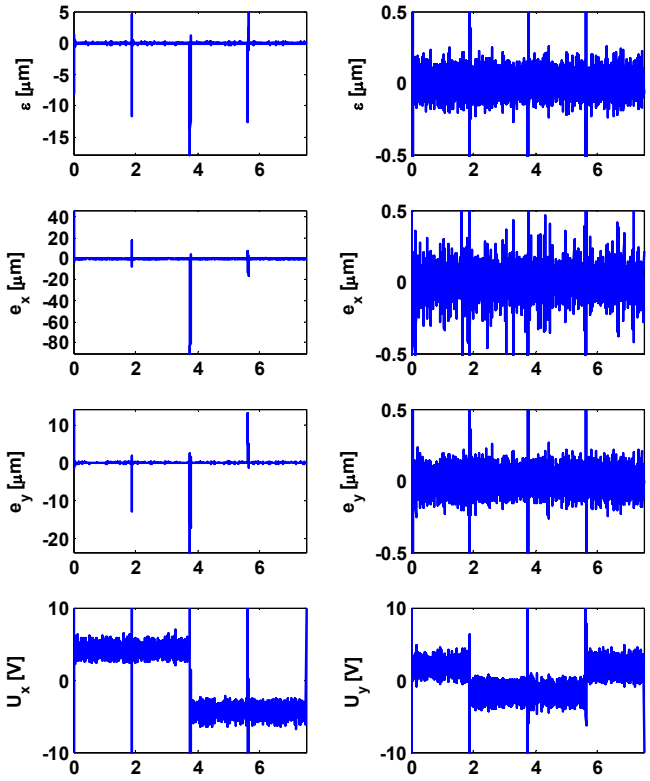

Fig. 9. Experimental Results for Case V.

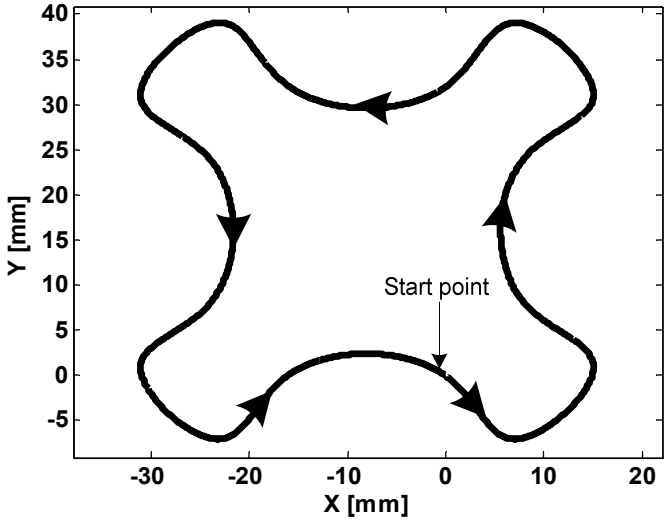

Fig. 10. Freeform contour schematic.

Table 2
Freeform Contour Cases.

Case	VI	VII	VIII	IX	X
q	10^{-3}	10^{-2}	0.1	0.1	0.1
q_b	0.1	0.1	0.1	10^{-2}	10^{-3}
q/q_b	10^{-2}	0.1	1	10	100

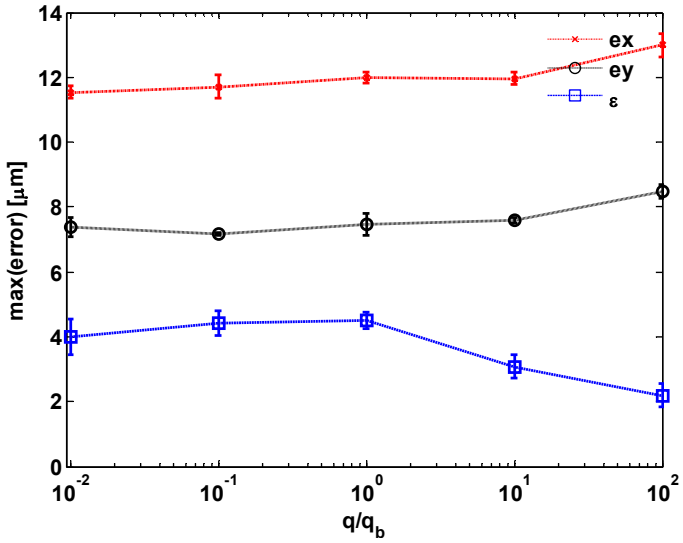

Fig. 11. Maximum transient errors for Cases VI–X.

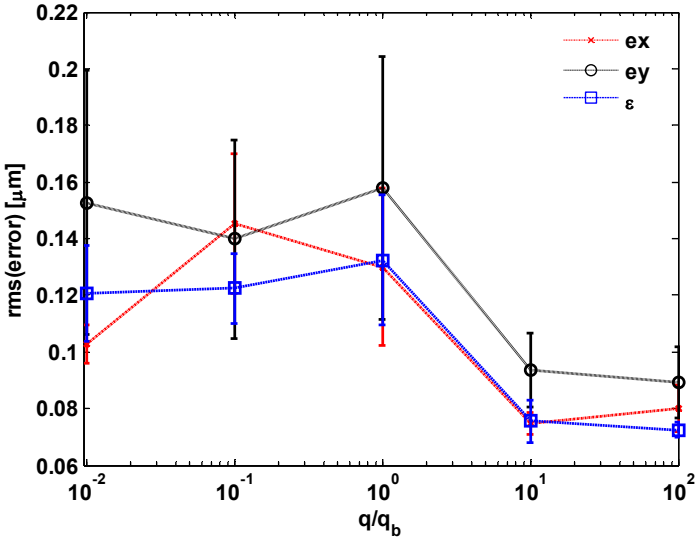

Fig. 12. Steady state errors for Cases VI–X.

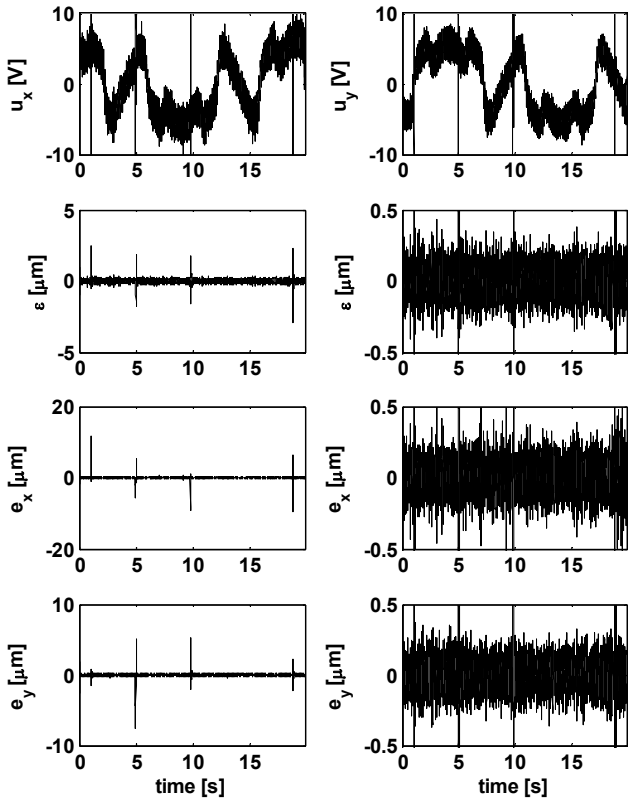

Fig. 13. Experimental Results for Case VI.

II. Hierarchical optimal force–position control of complex manufacturing

ABSTRACT

A hierarchical optimal controller is developed in this paper to regulate the machining force and axis positions, simultaneously, in a micro end milling process. The process is divided into two levels of decision making. The bottom level includes the measurable states, which in this work comprises the axis positions. The top level includes the higher order objectives, which can be derived from the bottom level objectives by an aggregation relationship. In this work, the top level's objective is to regulate the machining force. A series of simulations were conducted in which the weighting between the top and the bottom level objectives is adjusted within the feasible range. The results demonstrated that excellent tracking of both axis positions and machining force are achieved during the steady state regardless of the weighting. However, the transient performance of the system could be systematically shaped to achieve better performance of either objectives. For the purpose of comparison a decentralized optimal controller was constructed and simulated for the feasible range of controller weights. When the axis position errors were weighted heavily, both controllers were able to regulate the axis errors well, while the hierarchical controller had smaller machining force errors. When the machining force errors were weighted heavily, although the machining force error decreased for the decentralized controller the axis position errors increased significantly. However, with heavy machining force weighting, the hierarchical controller was able to manipulate the axial errors in a way that while the machining force error was reduced, the

contour error (i.e., smallest deviation from the tool tip to the desired contour) remained small.

KEYWORDS: Hierarchical Control, Optimal Control, Internal Model Principle

1. Introduction

The demand for higher productivity in todays' manufacturing plants, has resulted in a need for lower machining process time that leads to higher machining forces. Excessive machining forces can cause tool breakage, low surface quality, spindle stall, and other undesirable effects. In addition, due to changes in cutting geometry, tool wear, etc., the machining force constantly changes throughout the operation.

As a result of machining uncertainties and process variations, adaptive approaches have been utilized extensively in machining force control literature. In these methods model parameters are estimated online and no prior knowledge of the system is required. [Harder 1995, Landers and Ulsoy 2000] In these techniques stability is maintained over a wide range of parameter variations by adjusting the controller gains based upon online measurements. However, implementation, analysis, and development of adaptive methods are difficult, making them less desirable in industry. Where the development of a model was feasible, different model based approaches have been utilized to robustly control machining forces. Some examples for adaptive approaches are model reference control [Landers and Ulsoy 2000], linearized force process control [Harder 1995], and robust machining force control [Kim, et al. 2003]. Landers et al., compared four model based approaches with an adaptive approach.[Landers, et al. 2004] The derived models

can also aid in process planning, monitoring, and analysis, making them useful beyond machining force control [Landers and Ulsoy 2000]. Other machining force control methods adopted in the literature utilized artificial intelligence techniques such as neural networks as neural networks [Luo, et al. 1998] and fuzzy logic [Kim and Jeon 2011].

Integration of force control and position control is a well-developed area in robotics. A survey on some of the studies of a class of parallel force/position control schemes can be found in a work by Siciliano et al.[Siciliano 2000] Generally two types of force/position control schemes are used in literature.[Siciliano 2000] The first general category is open loop force control which is controlling the motion and force by developing a relationship (i.e., mechanical impedance) between external forces and end-effector position.[Khayati, et al. 2006] The main group in this category is impedance control for which the objective is to regulate the mechanical impedance of the robot end-effector.[Kumar, et al. 2011] For example, Filaretov and Zuev proposed an optimal adaptive impedance force/position control for robotic manipulators.[Filaretov and Zuev 2008] Also, Ping-Lang and Zuev [Ping-Lang and Cheng-Hsin 2007] proposed an impedance method for parallel manipulators with an internal traditional industrial position control loop and an external computed torque control loop used to modify the reference position with respect to the desired position and the desired cutter impedance. The second category is closed loop force control or hybrid force/position control methods in which force and position are independently controlled along each joint or task subspace.[Bierbaum, et al. 2009, Khayati, et al. 2006, Kumar, et al. 2011] There are two main groups in this category, explicit or parallel and implicit. In explicit methods the force tracking error directly modifies the control signal to the motors. Bierbaum et al.,

proposed explicit hybrid position/force controller for parallel robots based on computed torque technique using visual measurements of the end effector pose and force measurements.[Bierbaum, et al. 2009] Huang et al., proposed a hybrid control position/force method based on online learning neural networks to enable a robot with a flexible tool to trace a given curve by visual information and force measurements.[Huang, et al. 2005] Karayiannidis proposed a neuro-adaptive controller for manipulators in compliant contact with a surface under non-parametric uncertainties.[Karayiannidis, et al. 2007] Panwar and Sukavanam proposed an optimal hybrid force/position controller for a robot manipulator and used a feed forward neural network to compensate for the uncertainties. In this study, the dynamic model of the manipulator is transformed into a constrained and an unconstrained motion using proper sliding surfaces and an optimal controller is defined for the modified system.[Panwar and Sukavanam 2007] In implicit methods there is an inner position control loop and an outer control loop which modifies the reference inputs to the inner loop in order to regulate the force errors while regulating the position errors.[Roy and Whitcomb 2002] Some of the works in this group are impulsive hybrid force/position control[Khayati, et al. 2006], cascaded implicit force/position control of an anthropomorphic hand[Bierbaum, et al. 2009], iterative-learning implicit force/position control for tracking an object of unknown shape[Visioli, et al. 2010], least Square based adaptive implicit force/position control [Kroger, et al. 2004], force/position controller with a varying gain for the position feedback loop[Munasinghe and Nakamura 2007].

Among the large number of literature in this area, few studies have considered the integration of machining force and axis position control in manufacturing area. Tang et

al. [Tang, et al. 2006] extended a hierarchical optimal control methodology [Franklin, et al. 1994] to integrate machining force, contour, and position control in a lathing process. In their approach no considerations were taken to account for the uncertainties in the model and the noise inherent in the physical system. The method presented in [Tang, et al. 2006] is extended in the present work to simultaneously control the machining force and axis positions in a micro end milling process. The bottom level is constructed such that the Internal Model Principle is utilized to address noise and uncertainties in the system, and feed forward capabilities are added to improve the performance.

In the method presented in this paper a complex process is divided into different levels where the higher level controls a high–level objective, based on propagated errors from the bottom level through aggregation relationships. A correction signal is sent to each local controller at the bottom level in order to regulate the higher level objectives while simultaneously regulating the low level errors. The correction signal in this structure acts as the coordinator for the low level controllers. The machining process considered in this work is a micro end milling process, which is decomposed into a two–layer hierarchical structure where machining force control is allocated to the top level and axis position control is allocated to the bottom level.

2. Approach

The hierarchical optimal control methodology was derived for a micro end milling process on a table top CNC machine (Fig. 1). Since only two dimensional motions are analyzed in this study, only two linear axes will be considered in the motion

system. However, the methodology is applicable to any motion system with multiple axes. Assuming the electrical dynamics are much faster than the mechanical dynamics, a common feed drive system model is considered [Srinivasan and Tsao 1997]. Including nonlinear friction, the dynamic equations of motion of the x and y axes, respectively, are

$$\tau_x \ddot{x}(t) + \dot{x}(t) = K_x u_x(t) - F_{fx}\left(\dot{x}(t)\right) \tag{1}$$

$$\tau_y \ddot{y}(t) + \dot{y}(t) = K_y u_y(t) - F_{fy}\left(\dot{y}(t)\right) \tag{2}$$

where τ_x and τ_y are time constants (s), K_x and K_y are the system gains ((mm/s)/V), x and y are the axis positions (mm), u is the command voltage (V), and F_f is the nonlinear friction (mm/s). The subscripts x and y refer to the x and y axes, respectively. The subsequent analysis is applied to the x axis.

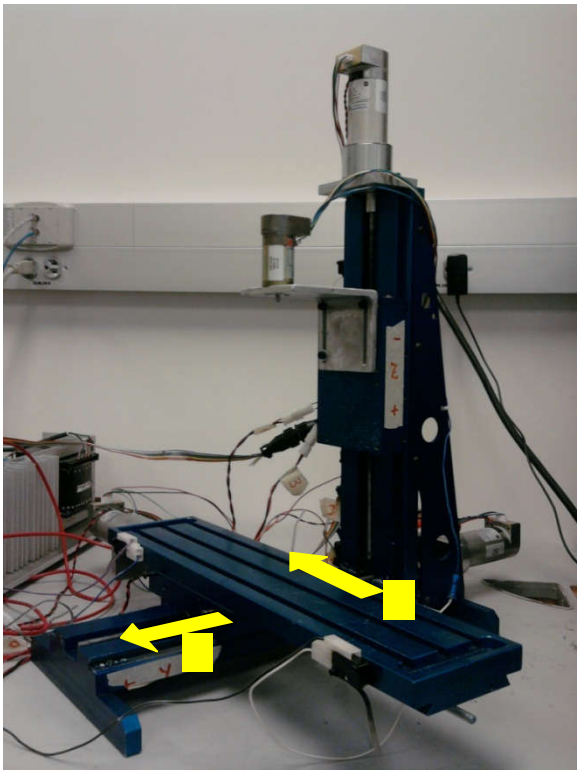

Fig. 1. Table top CNC machine.

Nonlinear friction in this model is considered as an unknown constant disturbance and is rejected by the Internal Model Principle. Therefore, an ideal model is considered first and is then modified based on the Internal Model Principle to account for the nonlinear friction. Ignoring nonlinear friction, the transfer function relating the axis position to the command voltage in Z domain using a Zero Order Hold is

$$G_x(z) = \frac{A_x z + B_x}{z^2 - \left(1 + e^{-\frac{T}{\tau_x}}\right) z + e^{-\frac{T}{\tau_x}}} \tag{3}$$

where $A_x = \tau_x K_x \left(\frac{T}{\tau_x} - 1 + e^{-\frac{T}{\tau_x}} \right)$, $B_x = \tau_x K_x \left(1 - e^{-\frac{T}{\tau_x}} - \frac{T}{\tau_x} e^{-\frac{T}{\tau_x}} \right)$, and T is the sample period. To apply the Internal Model Principle, the transfer function is multiplied by $\frac{z-1}{z-1}$. This will allow the controller to reject constant and slowly varying disturbances. After applying the same procedure to the y axis, the position dynamics of the whole system is converted into the difference domain. Considering the error signal $e_x(k) = r_x(k) - x(k)$ and $e_y(k) = r_y(k) - y(k)$, total dynamics of the position error in state space is

$$\begin{aligned} \mathbf{x_b}(k) &= \mathbf{A_b}\mathbf{x_b}(k-1) + \mathbf{B_b}\mathbf{u_b}(k-1) = \\ &\begin{bmatrix} \mathbf{A_{ex}} & \mathbf{0}_{3\times3} \\ \mathbf{0}_{3\times3} & \mathbf{A_{ey}} \end{bmatrix} \begin{bmatrix} \mathbf{e_x}(k-1) \\ \mathbf{e_y}(k-1) \end{bmatrix} + \begin{bmatrix} \mathbf{B_{ex}} & \mathbf{0}_{3\times1} \\ \mathbf{0}_{3\times1} & \mathbf{B_{ey}} \end{bmatrix} \begin{bmatrix} \mu_x(k-1) \\ \mu_y(k-1) \end{bmatrix} \end{aligned} \tag{4}$$

where $\mathbf{x_b}(k) = \begin{bmatrix} e_x(k-2) & e_x(k-1) & e_x(k) & e_y(k-2) & e_y(k-1) & e_y(k) \end{bmatrix}^T$,

$$\mathbf{A_{ex}} = \begin{bmatrix} 0 & 1 & 0 \\ 0 & 0 & 1 \\ -a_{x3} & -a_{x2} & -a_{x1} \end{bmatrix}, \qquad \mathbf{A_{ey}} = \begin{bmatrix} 0 & 1 & 0 \\ 0 & 0 & 1 \\ -a_{y3} & -a_{y2} & -a_{y1} \end{bmatrix}, \qquad \mathbf{B_{ex}} = \mathbf{B_{ey}} = \begin{bmatrix} 0 \\ 0 \\ 1 \end{bmatrix},$$

$$a_{x1(y1)} = -\left(e^{-\frac{T}{\tau_{x(y)}}} + 2 \right) z^2, \qquad a_{x2(y2)} = \left(2e^{-\frac{T}{\tau_{x(y)}}} + 1 \right) z, \qquad a_{x3(y3)} = -e^{-\frac{T}{\tau_{x(y)}}},$$

$$b_{x1(y1)} = K_{x(y)}\tau_{x(y)}\left(\frac{T}{\tau_{x(y)}} - 1 + e^{-\frac{T}{\tau_{x(y)}}} \right) z^2, \quad b_{x2(y2)} = K_{x(y)}\tau_{x(y)}\left(2 - 2e^{-\frac{T}{\tau_{x(y)}}} - \frac{T}{\tau_{x(y)}}\left(1 + e^{-\frac{T}{\tau_{x(y)}}} \right) \right) z,$$

$$b_{x3(y3)} = -K_{x(y)}\tau_{x(y)}\left(1 - e^{-\frac{T}{\tau_{x(y)}}} - \frac{T}{\tau_{x(y)}} e^{-\frac{T}{\tau_{x(y)}}} \right),$$ and the dummy control signal, $\mathbf{u_b}(k)$, is

$$\begin{aligned} \mathbf{u_b}(k) = \begin{bmatrix} \mu_x(k-1) \\ \mu_y(k-1) \end{bmatrix} = & \begin{bmatrix} r_x(k+1) + a_{x1} r_x(k) + a_{x2} r_x(k-1) + a_{x3} r_x(k-2) \\ r_y(k+1) + a_{y1} r_y(k) + a_{y2} r_y(k-1) + a_{y3} r_y(k-2) \end{bmatrix} \\ & - \begin{bmatrix} b_{x1} u_x(k) + b_{x2} u_x(k-1) + b_{x3} u_x(k-2) \\ b_{y1} u_y(k) + b_{y2} u_y(k-1) + b_{y3} u_y(k-2) \end{bmatrix} \end{aligned} \tag{5}$$

The vector $\mathbf{u_b}(k)$ will be constructed such that the importance of the bottom and higher level objectives can be systematically shaped. To accomplish this, the higher level objective must be propagated, using an aggregation relationship, to the bottom level where the physical control signals reside. The aggregation relationship relates top level objectives to bottom level objectives by defining top level states in terms of bottom level states.

The top level objective in this work is to maintain a desired maximum machining force per spindle revolution to achieve maximum operation efficiency in a micro end milling process. As can be seen from Fig. 2, in order to analyze machining forces acting on an end mill, the length of the tool in contact with the part is divided into N_d divisions. To determine the machining forces acting on each division, the divisions are modeled as individual face mills, each having a unique entry and exit angle. Assuming a uniform

pressure distribution on the flute, the machining forces applied to the i^{th} flute on the j^{th} division can be experimentally modeled in the discrete domain by

$$\begin{aligned} F_T^{i,j}(k) &= \left[K_T f_{i,j}^{\alpha_T}(k) d^{\beta_T}(k) V^{\gamma_T}(k)\right] a^{i,j}(k) \sigma_{i,j} \\ F_C^{i,j}(k) &= \left[K_C f_{i,j}^{\alpha_C}(k) d^{\beta_C}(k) V^{\gamma_C}(k)\right] a^{i,j}(k) \sigma_{i,j} \\ F_L^{i,j}(k) &= \left[K_L f_{i,j}^{\alpha_L}(k) d^{\beta_L}(k) V^{\gamma_L}(k)\right] a^{i,j}(k) \sigma_{i,j} \end{aligned} \tag{6}$$

where $F_T^{i,j}$ is the thrust force (N), $F_C^{i,j}$ is the cutting force (N), and $F_L^{i,j}$ is the longitudinal force (N) acting on the i^{th} flute on the j^{th} division (see Fig. 2). The parameters $K_{T,C,L}$, $\alpha_{T,C,L}$, $\beta_{T,C,L}$, and $\gamma_{T,C,L}$ are unknown constants and found experimentally. The parameter $f_{i,j}$ is the instantaneous feed of the i^{th} flute on the j^{th} division (mm) and is

$$f_{i,j} = \frac{V_r}{N_t N_f} \cos\left(\theta^{i,j}\right) \tag{7}$$

where N_f is the number of flutes, N_d is the number of divisions, V_r is the feedrate (mm/min), and $\theta^{i,j}$ is the angle between the j^{th} division of i^{th} flute and the instantaneous tangent to the tool path at the tool position (rad). The parameter d is the depth–of–cut (mm), V is the cutting velocity (mm/min) and is

$$V = \frac{D_t}{2} N_s \tag{8}$$

where D_t is the tool diameter (mm), and N_s is the spindle speed (rpm). The parameter $a^{i,j}$ is the chip area (mm^2) of the i^{th} flute on the j^{th} division and is

$$a^{i,j} = f^{i,j} \Delta z \tag{9}$$

where Δz is the tool division height (mm), and $\sigma_{i,j}$ is

$$\sigma_{i,j} = \begin{cases} 1 & \text{if } j^{\text{th}} \text{ division of } i^{\text{th}} \text{ flute is in contact with part} \\ 0 & \text{if } j^{\text{th}} \text{ division of } i^{\text{th}} \text{ flute is not in contact with part} \end{cases} \tag{10}$$

After some math, the thrust and cutting forces, in equation (6) can be expressed, respectively, as

$$\begin{aligned} F_T^{i,j} &= F_T^+ \cos\left(\theta^{i,j}\right)^{(\alpha_T+1)} \sigma_{i,j} \\ F_C^{i,j} &= F_C^+ \cos\left(\theta^{i,j}\right)^{(\alpha_C+1)} \sigma_{i,j} \end{aligned} \tag{11}$$

where $F_T^+ = \left[K_T f_f{}^{(\alpha_T+1)}(k)\Delta z^{(\beta_T+1)}(k) V^{\gamma_T}(k)\right]$ and $F_C^+ = \left[K_C f_f{}^{(\alpha_C+1)}(k)\Delta z^{(\beta_C+1)}(k) V^{\gamma_C}(k)\right]$. The parameters F_C^+ and F_T^+ are constant for constant process parameters.

The total machining forces applied to the tool in x, y, and z directions, respectively, are (see Fig. 2)

$$\begin{aligned} F_x &= \sum_{i=1}^{N_f}\sum_{j=1}^{N_d}\left(-F_T^{i,j}\cos\left(\theta^{i,j}\right) + F_C^{i,j}\sin\left(\theta^{i,j}\right)\right)\sigma_{i,j} \\ F_y &= \sum_{i=1}^{N_f}\sum_{j=1}^{N_d}\left(-F_T^{i,j}\sin\left(\theta^{i,j}\right) - F_C^{i,j}\cos\left(\theta^{i,j}\right)\right)\sigma_{i,j} \\ F_z &= \sum_{i=1}^{N_f}\sum_{j=1}^{N_d}\left(-F_L^{i,j}\right)\sigma_{i,j} \end{aligned} \tag{12}$$

At this point a set of end milling experiments are performed in which F_x, F_y, and F_z are recoded for different process parameters and then using an optimization algorithm the optimum values for $K_{T,C,L}$, $\alpha_{T,C,L}$, $\beta_{T,C,L}$, and $\gamma_{T,C,L}$ are found to fit the model in equation (12) to the experimental data. Also from equation (12) the square of the normal machining force applied to the tool in the x–y plane is

$$F_n^2 = \left[\sum_{i=1}^{N_f}\sum_{j=1}^{N_d}\left(-F_T^{i,j}\cos\left(\theta^{i,j}\right)+F_C^{i,j}\sin\left(\theta^{i,j}\right)\right)\right]^2 + \left[\sum_{i=1}^{N_f}\sum_{j=1}^{N_d}\left(-F_T^{i,j}\sin\left(\theta^{i,j}\right)-F_C^{i,j}\cos\left(\theta^{i,j}\right)\right)\right]^2 \quad (13)$$

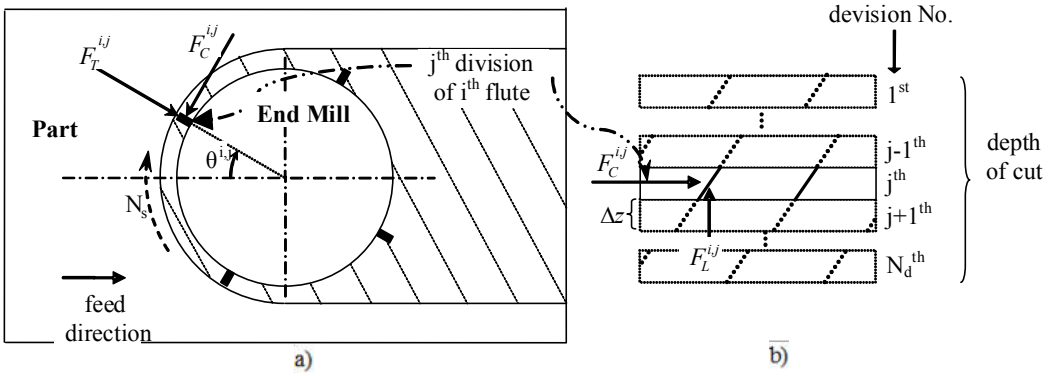

Fig. 2. Machining forces acting on tool in end milling process; a) top view b) front view.

Using equation (11) in (13), the square of the normal machining force applied to the tool in the x–y plane is

$$F_n^2 = \left[\sum_{i=1}^{N_f}\sum_{j=1}^{N_d}\left(-F_T^{+}\cos\left(\theta^{i,j}\right)^{(\alpha_T+2)}\sigma_{i,j}+F_C^{+}\cos\left(\theta^{i,j}\right)^{(\alpha_C+1)}\sin\left(\theta^{i,j}\right)\sigma_{i,j}\right)\right]^2 + \left[\sum_{i=1}^{N_f}\sum_{j=1}^{N_d}\left(-F_T^{+}\cos\left(\theta^{i,j}\right)^{(\alpha_T+1)}\sin\left(\theta^{i,j}\right)\sigma_{i,j}-F_C^{+}\cos\left(\theta^{i,j}\right)^{(\alpha_C+2)}\sigma_{i,j}\right)\right]^2 = \left(F_C^{+}F_{C2}^{*}-F_T^{+}F_{T1}^{*}\right)^2+\left(F_T^{+}F_{T2}^{*}+F_C^{+}F_{C1}^{*}\right)^2 \quad (14)$$

where

$$
\begin{aligned}
F_{T1}^{*} &= \sum_{i=1}^{N_f}\sum_{j=1}^{N_d}\left(\cos\left(\theta^{i,j}\right)^{(\alpha_T+2)}\sigma_{i,j}\right)\\
F_{T2}^{*} &= \sum_{i=1}^{N_f}\sum_{j=1}^{N_d}\left(\cos\left(\theta^{i,j}\right)^{(\alpha_T+1)}\sin\left(\theta^{i,j}\right)\sigma_{i,j}\right)\\
F_{C1}^{*} &= \sum_{i=1}^{N_f}\sum_{j=1}^{N_d}\left(\cos\left(\theta^{i,j}\right)^{(\alpha_C+2)}\sigma_{i,j}\right)\\
F_{C2}^{*} &= \sum_{i=1}^{N_f}\sum_{j=1}^{N_d}\left(\cos\left(\theta^{i,j}\right)^{(\alpha_C+1)}\sin\left(\theta^{i,j}\right)\sigma_{i,j}\right)
\end{aligned}
\tag{15}
$$

Therefore

$$
\begin{aligned}
F_n^2 = F_T^{+2}F_{T1}^{*\,2} + F_C^{+2}F_{C2}^{*\,2} - 2F_T^{+}F_C^{+}F_{T1}^{*}F_{C2}^{*} + F_T^{+2}F_{T2}^{*\,2} + F_C^{+2}F_{C1}^{*\,2} + 2F_T^{+}F_C^{+}F_{T2}^{*}F_{C1}^{*} = \\
F_T^{+2}\left(F_{T1}^{*\,2}+F_{T2}^{*\,2}\right) + F_C^{+2}\left(F_{C1}^{*\,2}+F_{C2}^{*\,2}\right) + 2F_T^{+}F_C^{+}\left(F_{T2}^{*}F_{C1}^{*} - F_{T1}^{*}F_{C2}^{*}\right)
\end{aligned}
\tag{16}
$$

For a known depth–of–cut, feedrate, and spindle speed, the maximum normal machining force per spindle revolution is

$$
\left(F_n^{\max}\right)^2 = \left(F_T^{+}\right)^2 + \left(F_C^{+}\right)^2\left(F_{C1}^{**2}+F_{C2}^{**2}\right) + 2F_T^{+}F_C^{+}\left(F_{T2}^{**}F_{C1}^{**} - F_{T1}^{**}F_{C2}^{**}\right) \tag{17}
$$

where F_{T1}^{**}, F_{T2}^{**}, F_{C1}^{**}, and F_{C2}^{**} are the values of F_{T1}^{*}, F_{T2}^{*}, F_{C1}^{*}, and F_{C2}^{*}, respectively, resulting in $F_n^{\max}$ and are found by numerical simulation. To reduce the computational burden during real time implementation, a curve is fit to equation (17) with stored values of F_{T1}^{**}, F_{T2}^{**}, F_{C1}^{**}, and F_{C2}^{**} for different depths–of–cut, feedrates, and spindle speeds in the admissible process operating range. An excellent model structure relating $F_n^{\max}$ to d, V_r, and N_s is

$$
F_n^{\max} = K_1 V_r^{b_1}\left(N_s^{k_{c_1}}\left(N_s^{\,2} + k_{c_2}N_s + k_{c_3}\right)\right)\left(d^{k_{d_1}}\left(d^2 + k_{d_2}d + k_{d_3}\right)\right) \tag{18}
$$

where the values of the model parameters K_1, k_{c_1}, k_{c_2}, k_{c_3}, k_{d_1}, k_{d_2}, and k_{d_3} are found via optimization. A particle swarm optimization code was written in MATLAB and then implemented. The RMS of the error percentage between the model and simulated machining force is 0.26%.

To maintain a maximum machining force per spindle revolution for different spindle speeds and depths–of–cut, equation (17) is solved for V_r given a desired value of $F_n^{\max}$. Equation (17) can be rewritten as

$$\left(F_n^{\max}\right)^2 = \left(\left(F_{T1}^{**}\right)^2 + \left(F_{T2}^{**}\right)^2\right)\tilde{F}_T^2\, V_r^{2(\alpha_T+1)} + \left(\left(F_{C1}^{**}\right)^2 + \left(F_{C2}^{**}\right)^2\right)\tilde{F}_C^2\, V_r^{2(\alpha_C+1)} + 2\left(-F_{T1}^{**}F_{C2}^{**} + F_{T2}^{**}F_{C1}^{**}\right)\tilde{F}_T\,\tilde{F}_C\, V_r^{(\alpha_T+\alpha_C+2)} \tag{19}$$

where $\tilde{F}_T = \dfrac{K_T\left(2\pi R_t\right)^{\gamma_T}}{N_t^{(\alpha_T+1)}N_d} d^{(\beta_T+1)} N_s^{(\gamma_T-\alpha_T-1)}$ and $\tilde{F}_C = \dfrac{K_C\left(2\pi R_t\right)^{\gamma_C}}{N_t^{(\alpha_C+1)}N_d} d^{(\beta_C+1)} N_s^{(\gamma_C-\alpha_C-1)}$.

By solving equation (19) for V_r, a reference feedrate is calculated based on a desired maximum normal machining force per spindle revolution for different values of depth–of–cut and spindle speed. To reduce the real time computational burden, a curve is fit to the obtained values of the reference feedrate versus $F_n^{\max}$, d, and N_s in the viable process operating range. This reference feedrate is then fed to the interpolator. It should be mentioned that the machining force model parameters (i.e., K, α, β, γ) are nominal values and can change with tool wear and cutting temperature. However, in this paper, ideal conditions are assumed (i.e., changes in these process parameters are negligible during the process). If the model parameters change significantly more than the stability margins of the controller, a parameter estimation procedure should be implemented to update the model and, thus the controller, during the operation.

An aggregation relationship is now derived from equation (18) to relate $F_n^{\max}$ to the bottom level states (i.e., axis position errors). The higher level objective in this work is to track a desired reference machining force. Considering the fact that $V_r = \left(\left(V_r^{\mathrm{x}} \right)^2 + \left(V_r^{\mathrm{y}} \right)^2 \right)^{1/2}$ and assuming that the actual depth–of–cut and spindle speed are the same as their corresponding reference values, the top level tracking error can be written as

$$F_{n_{\mathrm{ref}}}^{\max} - F_n^{\max} = e_F = K_1 \begin{pmatrix} \left(\left(V_{\mathrm{x}}^r \right)^2 + \left(V_{\mathrm{y}}^r \right)^2 \right)^{b_1/2} N_s^{k_{c_1}} \left(N_s^{\,2} + k_{c_2} N_s + k_{c_3} \right) \\ d^{k_{d_1}} \left(d^2 + k_{d_2} d + k_{d_3} \right) \end{pmatrix} - K_1 \begin{pmatrix} \left(V_{\mathrm{x}}^2 + V_{\mathrm{y}}^2 \right)^{b_1/2} N_s^{k_{c_1}} \left(N_s^{\,2} + k_{c_2} N_s + k_{c_3} \right) \\ d^{k_{d_1}} \left(d^2 + k_{d_2} d + k_{d_3} \right) \end{pmatrix} \tag{20}$$

Assuming small variations in the process parameters during the operation, equation (20) can be linearized about the operating conditions via a Taylor series expansion. Ignoring higher order terms

$$\begin{aligned} e_F = & -K_1 \begin{pmatrix} b_1 V^{b_1 - 2} N_s^{k_{c_1}} \left(N_s^2 + k_{c_2} N_s + k_{c_3} \right) \\ d^{k_{d_1}} \left(d^2 + k_{d_2} d + k_{d_3} \right) \end{pmatrix} V_x \left(V_x - V_{rx} \right) \\ & - K_1 \begin{pmatrix} b_1 V^{b_1 - 2} N_s^{k_{c_1}} \left(N_s^2 + k_{c_2} N_s + k_{c_3} \right) \\ d^{k_{d_1}} \left(d^2 + k_{d_2} d + k_{d_3} \right) \end{pmatrix} V_y \left(V_y - V_{ry} \right) \end{aligned} \tag{21}$$

where $V = \left(V_x^2 + V_y^2 \right)^{1/2}$. Using a first order backwards finite difference, the x–axis feedrate error is

$$V_x(k)-V_{rx}(k)=60\left(\frac{x(k)-x(k-1)}{T}-\frac{x_r(k)-x_r(k-1)}{T}\right)= \\ \frac{60}{T}\left(\left(x(k)-x_r(k)\right)-\left(x(k-1)-x_r(k-1)\right)\right)=\frac{60}{T}\left(-e_x(k)+e_x(k-1)\right) \tag{22}$$

A similar expression can be derived for the y–axis feedrate error. The machining force error can now be expressed as

$$e_F(k)=\Omega(k)V_x(k)\frac{-60}{T}\left(e_x(k)-e_x(k-1)\right)+\Omega(k)V_y(k)\frac{-60}{T}\left(e_y(k)-e_y(k-1)\right) \tag{23}$$

where $\Omega(k)=-K_1\begin{pmatrix} b_1V(k)^{b_1-2}N_s^{k_{c_1}}\left(N_s^{\,2}+k_{c_2}N_s+k_{c_3}\right) \\ d^{k_{d_1}}\left(d^2+k_{d_2}d+k_{d_3}\right)\end{pmatrix}$. The linearized machining force error is now related to the lower level states (i.e., axis position errors) by the derived aggregation relation

$$e_F(k)=\mathbf{C}(k)\mathbf{x_b}(k)=\begin{bmatrix}0 & -c_x(k) & c_x(k) & 0 & -c_y(k) & c_y(k)\end{bmatrix}\mathbf{x_b}(k) \tag{24}$$

where $c_x(k)=-\frac{60}{T}\Omega(k)V_x(k)$ and $c_y(k)=-\frac{60}{T}\Omega(k)V_y(k)$. Therefore, the aggregation relation relating machining force error to the axis position errors is

$$x_{top}(k)=e_F(k)=\mathbf{C}(k)\mathbf{x_b}(k) \tag{25}$$

Therefore, using this aggregation relationship, the unmeasurable top level goal is now approximated by a linear combination of measurable bottom level states. As can be seen in equation (25), the top level error goes to zero if the bottom level errors are driven to zero. However, bottom level errors are unavoidable during transient phases. It will be seen that emphasizing the machining force error will allow the axes to be coordinated such that machining force error is reduced even if the axis positions errors are large during these phases. At these points, top and bottom goals are competing objectives and it

is desired for both to be small. In fact, the bottom level goal results in preventing the deviation of each axis from its reference and the top level goal synchronizes the axes, ensuring the relative movement of the axes results in a lower deviation of the maximum machining force from the desired value.

In order to regulate machining force and axis position errors simultaneously, an optimal tracking control problem is now defined and solved, as outlined in [Lewis and Syrmos 1995]. The cost function in this problem comprises both the bottom level and top level objectives and is

$$J_b = \frac{1}{2}\sum_{k=1}^{\infty} L_b(k) \tag{26}$$

where

$$L_b(k) = \left\{ \begin{array}{c} \left[\mathbf{C}(k)\mathbf{x_b}(k) - e_F^r(k)\right]^T q \left[\mathbf{C}(k)\mathbf{x_b}(k) - e_F^r(k)\right] \\ +\mathbf{u_b^T}(k)\mathbf{R_b}\mathbf{u_b}(k) + \mathbf{x_b^T}(k)\mathbf{Q_b}\mathbf{x_b}(k) \end{array} \right\} \tag{27}$$

and e_F^r is the reference maximum machining force error, which is zero. In equation (27) the first term maintains the aggregation relationship between the top and bottom levels. The second and third terms are used to penalize the control usage and state deviations, respectively, at the bottom level. The Hamiltonian at the bottom level is

$$H_b(k) = L_b(k) + \boldsymbol{\lambda}_\mathbf{b}^\mathbf{T}(k+1)\left[\mathbf{A_b}\mathbf{x_b}(k) + \mathbf{B_b}\mathbf{u_b}(k)\right] \tag{28}$$

Taking the derivative of the Hamiltonian with respect to $\mathbf{x_b}(k)$ and noting that $e_F^r(k) = 0$, the Lagrange multiplier is

$$\boldsymbol{\lambda}_\mathbf{b}(k) = \left[\mathbf{C}^\mathbf{T}(k) q \mathbf{C}(k) + \mathbf{Q_b}\right]\mathbf{x_b}(k) + \mathbf{A_b^T}\boldsymbol{\lambda}_\mathbf{b}(k+1) \tag{29}$$

Taking the partial derivative of equation (28) with respect to $\mathbf{u_b}(k)$, equating the result to zero, and rearranging gives the optimal control law

$$\mathbf{u}_\mathbf{b}(k) = -\mathbf{R}_\mathbf{b}^{-1}\mathbf{B}_\mathbf{b}^{\mathrm{T}}\boldsymbol{\lambda}_\mathbf{b}(k+1) \tag{30}$$

Substituting $\mathbf{u_b}(k)$ from equation (30) into equation (4)

$$\mathbf{x}_\mathbf{b}(k+1) = \mathbf{A}_\mathbf{b}\mathbf{x}_\mathbf{b}(k) - \mathbf{B}_\mathbf{b}\mathbf{R}_\mathbf{b}^{-1}\mathbf{B}_\mathbf{b}^{T}\boldsymbol{\lambda}_\mathbf{b}(k+1) \tag{31}$$

Now it is assumed that the Lagrange multiplier can be expressed by

$$\boldsymbol{\lambda}_\mathbf{b}(k) = \mathbf{P}_\mathbf{b}(k)\mathbf{x}_\mathbf{b}(k) \tag{32}$$

where $\mathbf{P_b}(k)$ is a positive definite, nonsingular matrix. Substituting equation (32) into equations (29) and (31) and rearranging, the following Ricatti equation is derived

$$\mathbf{P}_\mathbf{b}(k) = \mathbf{C}^{\mathrm{T}}(k)q\,\mathbf{C}(k) + \mathbf{Q}_\mathbf{b} + \mathbf{A}_\mathbf{b}^{\mathrm{T}}\mathbf{P}_\mathbf{b}(k+1)\left(\mathbf{I} + \mathbf{B}_\mathbf{b}\mathbf{R}_\mathbf{b}^{-1}\mathbf{B}_\mathbf{b}^{\mathrm{T}}\mathbf{P}_\mathbf{b}(k+1)\right)^{-1}\mathbf{A}_\mathbf{b} \tag{33}$$

The matrix $\mathbf{P_b}(k)$ is found from solving equation (33). Since an infinite–time control problem is used, the steady state value of $\mathbf{P_b}$, denoted $\overline{\mathbf{P}}_\mathbf{b}$, is used to solve the above Ricatti equation. Given $\mathbf{A_b}$, $\mathbf{B_b}$, $\mathbf{Q_b}$, $\mathbf{R_b}$, q, and $\mathbf{C}(k)$, the term $\overline{\mathbf{P}}_\mathbf{b}$ can be calculated off–line. If the ranges of c_x and c_y are known, curves can be fit to the entries of $\overline{\mathbf{P}}_\mathbf{b}$ over these ranges. These curves are then used for online implementation to reduce computational effort. Knowing the time history of $\overline{\mathbf{P}}_\mathbf{b}$, the optimal control signal can be expressed as

$$\mathbf{u}_\mathbf{b}(k) = -\mathbf{K}_\mathbf{b}\mathbf{x}_\mathbf{b}(k) \tag{34}$$

where the control gain is

$$\mathbf{K}_\mathbf{b} = \left[\mathbf{R}_\mathbf{b} + \mathbf{B}_\mathbf{b}^{\mathrm{T}}\overline{\mathbf{P}}_\mathbf{b}\mathbf{B}_\mathbf{b}\right]^{-1}\mathbf{B}_\mathbf{b}^{\mathrm{T}}\overline{\mathbf{P}}_\mathbf{b}\mathbf{A}_\mathbf{b} \tag{35}$$

The physical control signals are computed from

$$\begin{bmatrix} b_{x1}u_x(k) \\ b_{y1}u_y(k) \end{bmatrix} = -\begin{bmatrix} b_{x2}u_x(k-1)+b_{x3}u_x(k-2) \\ b_{y2}u_y(k-1)+b_{y3}u_y(k-2) \end{bmatrix} + \begin{bmatrix} r_x(k+1)+a_{x1}r_x(k)+a_{x2}r_x(k-1)+a_{x3}r_x(k-2) \\ r_y(k+1)+a_{y1}r_y(k)+a_{y2}r_y(k-1)+a_{y3}r_y(k-2) \end{bmatrix} + \mathbf{K_b}\mathbf{x_b}(k) \tag{36}$$

Note that the control signals require the reference axis positions at the next iteration, which are typically known.

3. Results and discussion

In this section, the performance of the proposed hierarchical control methodology is explored via a micro end milling simulation of a diamond contour (Fig. 3) on a graphite epoxy composite part using an aluminum titanium nitride coated tool with four flutes and a helix angle of 40°. As these tools break when lateral machining forces in excess of 100 N are applied, a maximum normal machining force per revolution of 30 N is selected as the reference in order to accommodate machining force overshoot due to rapid reference force changes in the process (e.g., at corners or when sudden changes in depth–of–cut occur). The servomechanism parameters used here are from the table–top CNC machine [H. Zomorodi, et al. 2010]: $\tau_x = 9.94\times10^{-3}$ s, $\tau_y = 1.04\times10^{-2}$ s, $K_x = 1.88$ (mm/s)/V, and $K_y = 1.76$ (mm/s)/V. The machining force process parameters are $K_C = 1.06\times10^5$, $K_T = 3.02\times10^5$, $K_L = 2.79\times10^3$, $\alpha_C = 0.959$, $\alpha_T = 1.91$, $\alpha_L = -6.72\times10^{-2}$, $\beta_C = 1.05$, $\beta_T = 1.58$, $\beta_L = 0.933$, $\gamma_C = 0.320$, $\gamma_T = 0.263$, and $\gamma_L = -0.504$. The spindle speed and the depth–of–cut are 7000 rpm and 0.5 mm, respectively, and a constant velocity interpolator is used to generate the reference axis trajectories. A sample period of 1 ms is

used and the control signals are saturated at ±10 V. For all simulations, the tool starts at rest at the x–y coordinate system origin. The control signal weighting matrix is $\mathbf{R_b} = 10^3 \mathbf{I}_{2\times 2}$ for all of the case studies and $\mathbf{Q_b}$ is of the form $\mathbf{Q_b} = q_b \mathbf{I}_{6\times 6}$. Considering the operating range of the depth–of–cut and spindle speed, a viable range for c_x and c_y is computed. The Riccati equation is then solved offline over the viable ranges of c_x and c_y and the entries of $\bar{\mathbf{P}}_\mathbf{b}$ are curve fit to reduce the computational burden. The matrix $\bar{\mathbf{P}}_\mathbf{b}$ is then updated at each sample period after c_x and c_y are calculated.

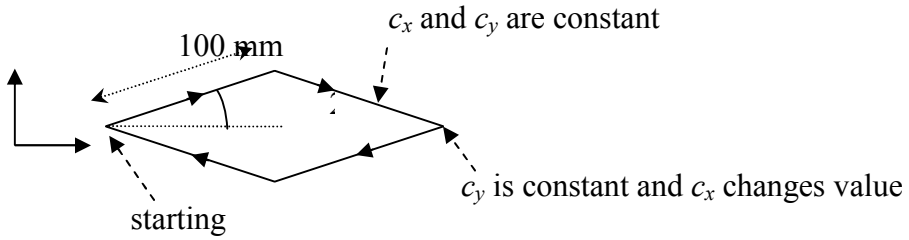

Fig. 3. Diamond contour used for simulation studies.

In this study, the depth–of–cut and spindle speed are constant; therefore, because a constant reference machining force is considered, a constant reference velocity is fed to the interpolator based on equation (20). As can be seen in Fig. 3, tracking a diamond contour with a constant depth–of–cut comprises two types of movement. The first type consists of linear segments for which the reference velocity and the parameters c_x and c_y are constant and, hence, the matrix $\bar{\mathbf{P}}_\mathbf{b}$ is constant. The second type consists of transition points at the corners where c_x and c_y suddenly change values due to the changes in the reference velocity direction and, hence, present a significant challenge for machining force control. At each corner, one of the axes changes its direction of motion; therefore,

its reference velocity changes from positive to negative, or vice versa, and the motors must overcome the axis inertia, which acts as a sudden disturbance for the velocity and, consequently, the machining force. In order to investigate the performance of the hierarchical controller when machining the corners of the part, an analysis is now performed over the feasible range of optimization weights.

3.1. *Hierarchical control analysis*

The feasible ranges of q and q_b were determined to be $q \in \begin{bmatrix} 10^{-3} & 5\times10^{-3} \end{bmatrix}$ and $q_b \in \begin{bmatrix} 10^{-3} & 5 \end{bmatrix}$, respectively, by trial and error using a multitude of simulations. In Table 1, nine different combinations of q and q_b are considered to analyze the effect of changing the emphasis between the top and bottom level objectives. Fig. 4 shows e_x, e_y, and e_F, at the right corner and the resulting contours for Cases I, III, V, VI, and IX in Table 1. Results for the right corner are presented since this is where the largest errors occur. It can be seen that as the ratio q/q_b increases, the axis position errors increase, the machining force errors decrease, and the axis error settling times increase. As the ratio q/q_b decreases, the opposite is true. The sharp changes in axis positions for small ratios of q/q_b cause large velocities and, hence, large machining force errors. As the ratio q/q_b increases, the peak x axis error approaches a constant, while the peak y axis error increases. However, it should be noted that the y axis error is an order of magnitude smaller than the x axis error since the x axis is changing directions at the right corner. The hierarchical controller intelligently adjusts the axis position errors to decrease the machining force errors for large ratios of q/q_b.

Table 1
Hierarchical controller simulation cases.

Case	I	II	III	IV	V	VI	VII	VIII	IX
Q	10^{-3}	10^{-3}	10^{-3}	10^{-3}	10^{-3}	10^{-3}	10^{-3}	2×10^{-3}	5×10^{-3}
q_b	5	2	1	0.5	10^{-2}	0.5×10^{-2}	10^{-3}	10^{-3}	10^{-3}
q/q_b	2×10^{-4}	5×10^{-4}	10^{-3}	2×10^{-3}	0.1	0.2	1	2	5

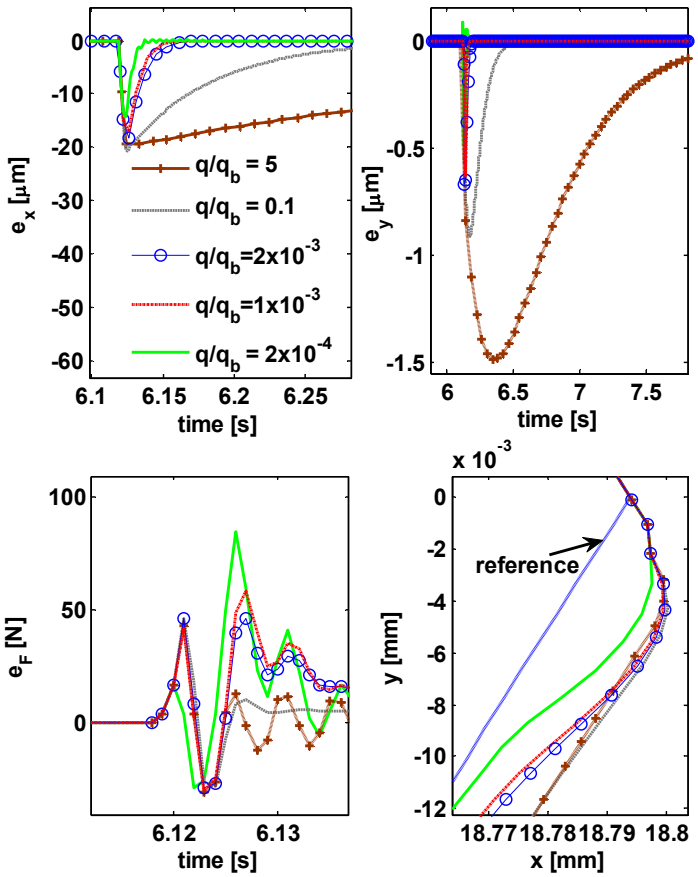

Fig. 4. Simulation of results for hierarchical controllers at diamond's right corner.

The simulation results, including the contour shape at the top and right corners, machining force error, axis position errors, and axis control signals, are presented for Cases I and IX in Figures 5 and 6, respectively. As can be seen in Figures 5 and 6, at both corners the control signal for the axis in which a change in direction occurs

saturates. This is due to the fact that the reference feedrate for the axis which changes direction suddenly from $-V_r\cos(\theta)$ to $V_r\cos(\theta)$, where θ is half of the corner angle, while the reference feedrate of the other axis remains constant. Also, it should be noted that since the right corner where the x axis changes direction is sharper (20°) than the top corner (140°) where only the y axis changes direction, the amount of overshoot in e_x at the right corner is substantially larger (approximately 5 times more) than the overshoot in e_y at the top corner. The results demonstrate that excellent tracking of both axis position and machining force errors are achieved during the steady state regardless of the weighting; however, the transient performance can be adjusted by changing the ratio of q/q_b. As this ratio increases, the axis position errors become larger and their settling times increase to reduce the machining force error.

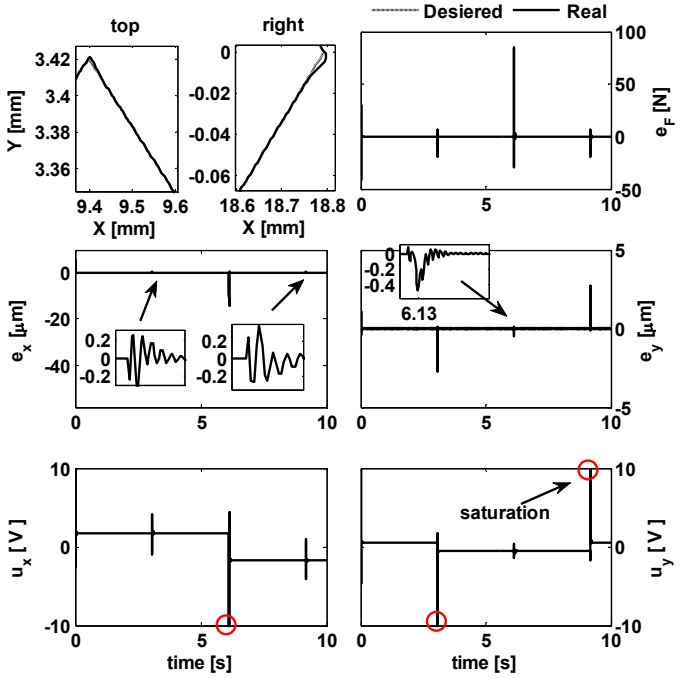

Fig. 5. Detailed simulation results for Case I.

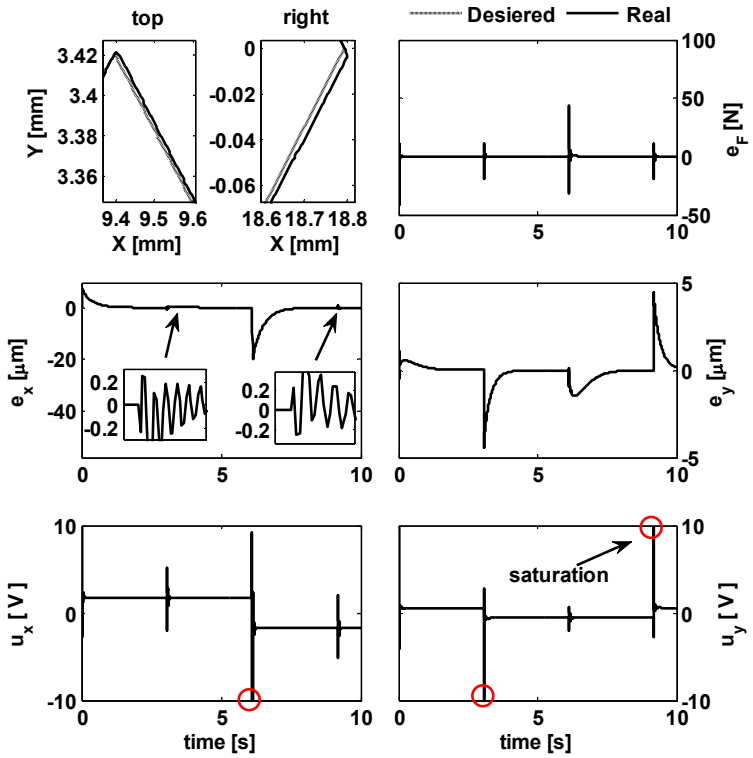

Fig. 6. Detailed simulation results for Case IX.

3.2. *Comparison of hierarchical and decentralized control*

In this section, an optimal decentralized controller is considered by setting $q = 0$, which results in no coupling between the bottom and top levels. This creates two separate decentralized optimal controllers for the axes. For the decentralized controller, the control signal weight is $\mathbf{R_b} = 10^3 \mathbf{I}_{2\times 2}$ and the maximum feasible range for q_b was found to be 10^{-4} to 10. Ten combinations where considered in this range, as shown in Table 2. In Fig. 7, e_x, e_y, e_F, and the resulting contours are compared Cases X, XIV, XVIII and XIX. It can be seen in Fig. 7 that as q_b decreases, transient axis position error magnitudes and settling times increase, and the transient machining force error magnitude and settling time

decrease. Again, it should be noted that since the y axis velocity does not change at the right corner, e_y is much smaller (by two orders of magnitude) than e_x.

Table 2
Decentralized controller simulation cases (i.e., $q = 0$).

Case	X	XI	XII	XIII	XIV	XV	XVI	XVII	XVIII	XIX
q_b	10	8	5	2	1	0.5	0.2	0.1	10^{-3}	10^{-4}
$1/q_b$	0.1	0.125	0.2	0.5	1	2	5	10	10^{3}	10^{4}

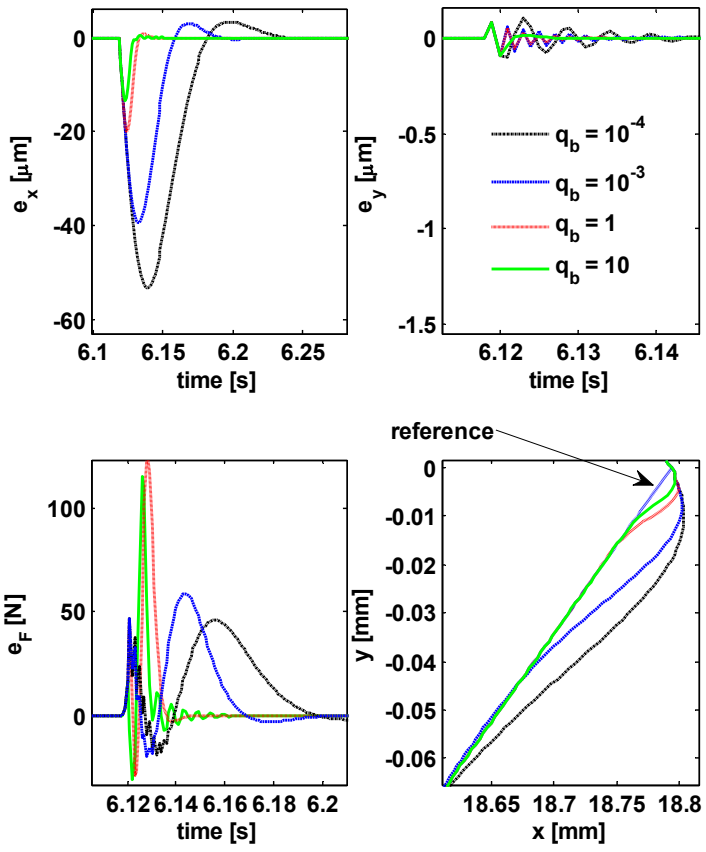

Fig. 7. Simulation results for decentralized controllers at diamond right corner.

A more detailed comparison of the transient performance for the hierarchical and decentralized controllers in their feasible controller parameter ranges is provided in Fig. 8. The maximum axis position, contour (i.e., smallest deviation from the tool tip to the desired contour), and machining force errors are shown, where the x axes are the ratio of q/q_b for the hierarchical controller and $1/q_b$ for the decentralized controller. Therefore, for both methods, lower ratios represent higher emphasis on axis tracking than on machining force tracking.

As the emphasis on axis tracking increases, the axis position error magnitudes decrease and the machining force error magnitudes increase for both methods; however, the machining force error magnitudes are always larger for the decentralized method since the hierarchical method is seeking to satisfy both constraints even when the emphasis on axis tracking is large. When this emphasis becomes very large, the x axis position error and contour error magnitudes converge to the same value for both methods. As the emphasis on axis tracking decreases, in the decentralized method the axis position and contour error magnitudes dramatically increase while the machining force error magnitude decreases. However, in the hierarchical method when the emphasis on axis tracking decreases, while the force error magnitude is always lower than the force errors for decentralized method, the x axis position and contour errors remain relatively constant. The hierarchical method is able to simultaneously reduce the machining force error magnitude and keep the contour error magnitude low by intelligently adjusting the y axis position error magnitude. Unlike the decentralized method, the contour and machining force error magnitudes are insensitive to controller gain variations for the

hierarchical method; thus, the hierarchical method provides excellent performance robustness.

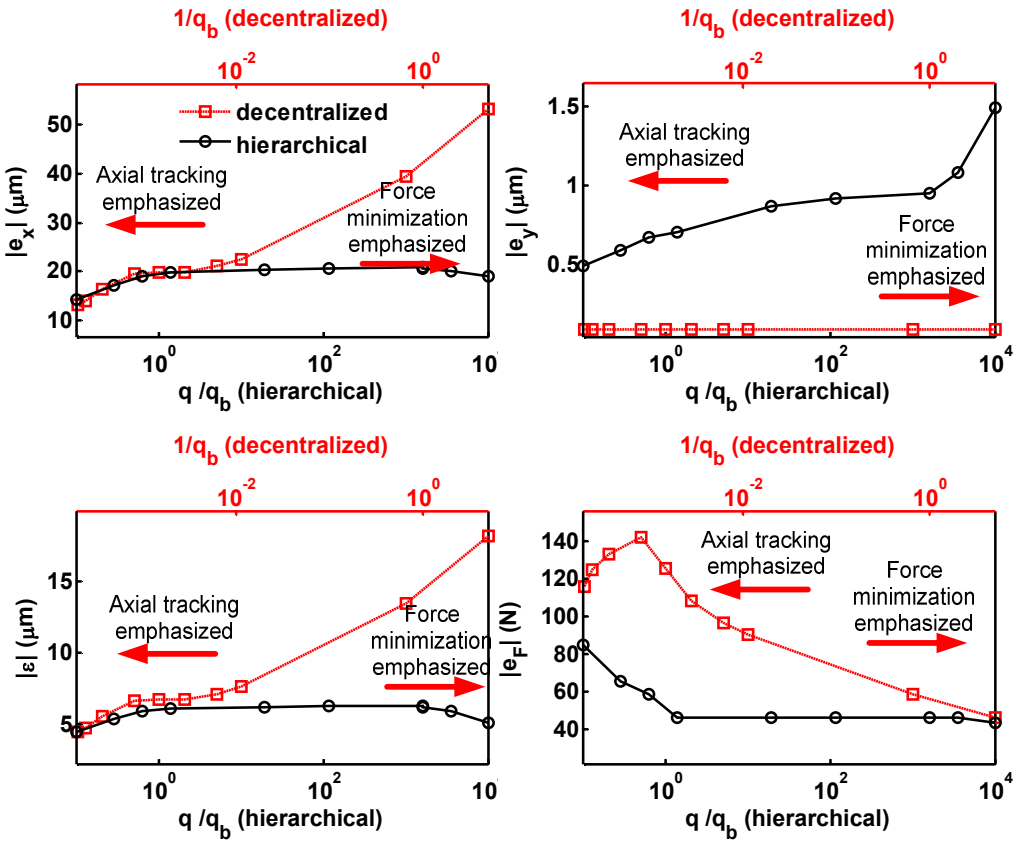

Fig. 8. Maximum axis position, contour, and machining force errors for hierarchical and decentralized controllers.

4. Summary and conclusions

A hierarchical controller was proposed and applied via simulation studies to a micro end milling process to simultaneously regulate axis position and machining force errors. Hierarchical aggregation techniques were utilized to propagate the higher level

objective (i.e., machining force regulation) to the bottom level (i.e., the physical equipment). Optimal control techniques were utilized with a cost function that weights individual axis position errors, machining force error, and control signal usage. A suboptimal solution was then implemented to reduce the required computational effort. The controller performance was verified through simulation case studies for a micro end milling process while cutting a diamond contour. To analyze the effect of changes in the emphasis on the axis position and machining force tracking, nine simulation studies were conducted where q/q_b increased from 2×10^{-4} (i.e., high emphasis on axis tracking) to 5 (i.e., high emphasis on machining force tracking). It was found that the increase in q/q_b resulted in an increase in the axis position error settling times, relatively constant contour error magnitudes, and a decrease in the transient machining force error.

A decentralized controller was developed by setting $q = 0$ and simulations were conducted for $10^{-4} \leq q_b \leq 10$. Both methods, decentralized and hierarchical, achieved excellent steady state performance in terms of both axis position and machining force tracking. As the emphasis on axis position tracking increased, the contour error magnitude decreased and the machining force transient error magnitude increased, and vice versa, for the decentralized controller. For the hierarchical controller, the transient contour error magnitude decreased to the same level as that for the decentralized controller when the emphasis on axis tracking increased; however, while the transient machine force error magnitude also increased, it remained below that for the decentralized controller. Also, as the emphasis on axis tracking decreased, the hierarchical controller was able to intelligently increase the transient y axis position error magnitude to decrease the transient machining error magnitude while keeping the

transient contour error magnitude low. Thus, the hierarchical controller performance is insensitive to changes in the controller parameters for a wide range of controller parameters.

Refrences

Bierbaum, A., Schill, J., Asfour, T., and Dillmann, R. (2009). Force position control for a pneumatic anthropomorphic hand. in *9th IEEE-RAS International Conference on Humanoid Robots*.

Filaretov, V. F., and Zuev, A. V. (2008). Adaptive force/position control of robot manipulators. in *IEEE/ASME International Conference on Advanced Intelligent Mechatronics*.

Franklin, G. F., Powell, J. D., and Emami-Naeini, A., "Feedback control of dynamic systems": Addison-Wesley Reading, 1994.

H. Zomorodi, R. G. Landers, and S. N. Balakrashnan (2010). Hierarchical position–contour control of linear axes. in *International Symposium on Flexible Automation*, Tokyo, Japan.

Harder, L., "Cutting force control in turning-solutions and possibilities," Ph. D. Dissertation, Department of Materials Processing, Royal Institute of Technology, Stockholm, 1995.

Huang, J., Todo, I., and Yabuta, T. (2005). Position/force hybrid control of a manipulator with a flexible tool using visual and force information. *Cutting Edge Robotics*, pp. 611-628.

Karayiannidis, Y., Rovithakis, G., and Doulgeri, Z. (2007). Force/position tracking for a robotic manipulator in compliant contact with a surface using neuro-adaptive control. *Automatica*, vol. 43, no. 7, pp. 1281-1288.

Khayati, K., Bigras, P., and Dessaint, L. A. (2006). A Multistage Position/Force Control for Constrained Robotic Systems With Friction: Joint-Space Decomposition, Linearization, and Multiobjective Observer/Controller Synthesis Using LMI Formalism. *IEEE Transactions on Industrial Electronics*, vol. 53, no. 5, pp. 1698-1712.

Kim, D., and Jeon, D. (2011). Fuzzy-logic control of cutting forces in CNC milling processes using motor currents as indirect force sensors. *Precision Engineering*, vol. 35, no. 1, pp. 143-152.

Kim, S. I., Landers, R. G., and Ulsoy, A. G. (2003). Robust machining force control with process compensation. *ASME Journal of Manufacturing Science and Engineering*, vol. 125, no. 3, pp. 423-430.

Kroger, T., Finkemeyer, B., Heuck, M., and Wahl, F. M. (2004). Adaptive implicit hybrid force/pose control of industrial manipulators: compliant motion experiments. in *IEEE/RSJ International Conference on Intelligent Robots and Systems, IROS*.

Kumar, N., Panwar, V., Sukavanam, N., Sharma, S., and Borm, J.-H. (2011). Neural network based hybrid force/position control for robot manipulators. *International Journal of Precision Engineering and Manufacturing*, vol. 12, no. 3, pp. 419-426.

Landers, R. G., and Ulsoy, A. G. (2000). Model-based machining force control. *ASME Journal of Dynamic Systems, Measurement, and Control*, vol. 122, no. 3, pp. 521-527.

Landers, R. G., Ulsoy, A. G., and Ma, Y. H. (2004). A comparison of model-based machining force control approaches. *International Journal of Machine Tools and Manufacture*, vol. 44, no. 7-8, pp. 733-748.

Lewis, F., and Syrmos, V., "Optimal control": Wiley-Interscience, 1995.

Luo, T., Lu, W., Krishnamurthy, K., and McMillin, B. (1998). A neural network approach for force and contour error control in multi-dimensional end milling operations. *International Journal of Machine Tools and Manufacture*, vol. 38, no. 10-11, pp. 1343-1359.

Munasinghe, S. R., and Nakamura, M. (2007). Hyperbolic tangent function based force-position compliant controller for robotic devices. in *International Conference on Control, Automation and Systems, ICCAS*.

Panwar, V., and Sukavanam, N. (2007). Design of Optimal Hybrid Position/Force Controller for a Robot Manipulator Using Neural Networks. *Mathematical Problems in Engineering*, vol. 2007, pp. 1-24.

Ping-Lang, Y., and Cheng-Hsin, L. (2007). Impedance force control for lateral milling of bone in total knee arthroplasty. in *IEEE International Conference on Systems, Man and Cybernetics, ISIC*.

Roy, J., and Whitcomb, L. L. (2002). Adaptive force control of position/velocity controlled robots: theory and experiment. *IEEE Transactions on Robotics and Automation*, vol. 18, no. 2, pp. 121-137.

Siciliano, B., "Parallel Force/Position Control of Robot Manipulators," *Robotics Research*, G. Giralt and G. Hirzinger, eds., pp. 78-89: Springer London, 2000.

Srinivasan, K., and Tsao, T. C. (1997). Machine tool feed drives and their control - A survey of the state of the art. *ASME Journal of Manufacturing Science and Engineering*, vol. 119, no. 4 PART II, pp. 743-748.

Tang, Y., Landers, R. G., and Balakrishnan, S. N. (2006). Hierarchical optimal force-position-contour control of machining processes. *Control Engineering Practice*, vol. 14, no. 8, pp. 909-922.

Visioli, A., Ziliani, G., and Legnani, G. (2010). Iterative-Learning Hybrid Force/Velocity Control for Contour Tracking. *IEEE Transactions on Robotics*, vol. 26, no. 2, pp. 388-393.

III. Hierarchical explicit model predictive control for extrusion fabrication processes

ABSTRACT

Freeze-form Extrusion Fabrication (FEF) is a recent additive manufacturing process that fabricates ceramics using ram-based paste extrusion in a freezing environment. To ensure consistent and on demand extrusion of the FEF process, ram velocity and extrusion force control algorithms, and the combination of both, during the fabrication process have previously been investigated. In this paper, an Explicit Model Predictive Controller (EMPC) is proposed to systematically combine the benefits of force and velocity control. To increase the robustness of the control method to paste material and rheology variations, these variations were considered as a disturbance to the system and an adaptive disturbance estimation technique was incorporated. Two EMPC surfaces were generated, one for full emphasis on force control and one for full emphasis on velocity control. A hierarchical structure was then constructed where, in the lower level, EMPCs for different objectives reside and in the higher level an emphasis management algorithm intelligently switches between full emphasis on force tracking or full emphasis on velocity tracking. Performance of the proposed controller was evaluated experimentally. A comparison with previous FEF control methods showed the advantage of the proposed method.

1. Introduction

Applications requiring ceramics have increased tremendously in recent decades for a wide variety of industries such as automotive, energy, biomedical, etc. However, since machining ceramics is very difficult [1] and using molds for small scale production are expensive [2] , Additive Manufacturing (AM) processes have emerged as a potential solution for prototyping and small scale production of ceramic parts. One of the main ceramic AM processes is 3D Extrusion Freeforming that involves continuous deposition of ceramic paste layer-by-layer until a 3D part is generated [3]. Some of the well-known methods in this area are Fused Deposition of Ceramics [4], Extrusion Freeform Fabrication [5], Direct Ink Writing [6], Multiphase Jet Solidification [7], Bioplotting, [8], Dispense Plotting [9], Robocasting [10], and Freeze-form Extrusion Fabrication (FEF) [11]. Many AM methods use organic binders for bonding ceramic powders, while methods like Robocasting and FEF use only 2–4 vol% organic binder with paste solids loading of 45–50 vol% or higher [12, 13]. This saves a substantial amount of time in the post processing stage and is environmentally friendly. One of the disadvantages of freeform extrusion methods for ceramic pastes is that these pastes normally have a complex rheology, making it difficult to predict their behavior. In addition, significant variations between batches exist due to variations in paste preparation techniques and variations in environmental conditions. Therefore, more complex control techniques are needed to guarantee consistent paste flow out of the extrusion nozzle.

In freeform extrusion processes there typically is no direct real-time measurement of the paste flow rate; therefore, flow control is conducted either by controlling the

extruder ram velocity [10, 14] or by controlling the pressure applied to the paste [6, 15]. According to previous studies [16], during extrusion when paste is flowing out of the nozzle and the extrusion force is at a steady state value, the ram velocity is linearly related to the paste flow rate. When operating the FEF process with a constant ram velocity, a significant amount of time may be required for the extrusion force to reach a steady state [17]. Without monitoring the extrusion force, there is no systematic way to detect when the extrusion force has reached steady conditions. This is a significant challenge when fabricating parts with intricate features that require frequent extrusion starts and stops. Another challenge in ceramic paste extrusion processing is air bubble release, which interrupts the paste flow for a period, creating a void in the part, and cannot be systematically compensated through ram velocity control. To avoid problems associated with air bubble release, force/pressure control is often used [18]. However, when using extrusion force control, the paste flow and, as a result, the bead thickness, cannot be systematically calculated and, even if a relationship between paste flow rate and extrusion force is found experimentally for one paste, it must be determined again when the paste or nozzle geometry change. With constant ram velocity at steady extrusion, the paste flow rate can be calculated regardless of the paste and nozzle combination, easing the selection of a table feed rate to match the paste flow rate. Deuser et al. [19] proposed a hybrid method where force control was used at the start and stop of deposition and when an air bubble release occurred, while ram velocity control was utilized during steady deposition. The method proposed in that work depended on an analytical paste model that, in turn, required parameters such as the nozzle length and diameter, as well as the identification of several model parameters, such as paste

viscosity, which depend on the environmental temperature, paste recipe, etc., and unmeasurable parameters, such as the amount of air trapped in the paste. In the current work, a nominal model is considered, and the effect of variations in the nominal model's parameters due to changes in paste material, nozzle geometry variations, etc. is considered as an additive disturbance to the extrusion force process, and the disturbance is estimated online using an adaptive disturbance estimation method [20, 21].

In order to use the benefits of extrusion force and ram velocity control, the control objective (i.e., emphasis on each control strategy) needs to change during the extrusion process based on the system status (i.e., extrusion start/stop, air bubble release, normal extrusion). The need for changes in the control objective during the process has many examples in manufacturing and robotics such as change between velocity and force control in a hole drilling process [22, 23] or in an end milling process [24], and change between position and force control during a grasping process using robotic hands [25]. One of the methods for changing the control objectives during the process is using a hierarchical control structure comprising a higher level (i.e., supervisory level) and a lower level (i.e., process level). In this structure, the supervisory level is responsible for monitoring the system status and determining control objectives in real-time, and the process level is responsible for implementing the control objectives [22, 23, 26]. Here, such hierarchical control structure has been incorporated in order to systematically switch the emphasis between extrusion force control to ram velocity control and back, depending on the system status. . The hierarchical structure in this work consists of two levels where, in the lower level process control algorithms reside that directly control the extrusion process according to predefined objectives (i.e., the amount of emphasis placed

on ram velocity and extrusion force tracking). In the higher level of the hierarchy, a supervisory algorithm is formulated to modify the objectives of the process level based on the status of the system (i.e., start/stop, air bubble release, normal extrusion). In the process level, a Nonlinear Model Predictive Controller (NMPC) is configured that, based on different cost functions, places the emphasis on extrusion force tracking or ram velocity tracking. Therefore, the proposed method in this paper is called Hierarchical Model Predictive Control (HMPC). Also it should be mentioned that in the NMPC formulation, the effect of disturbances is estimated and rejected.

Applications of Model Predictive Control (MPC) have widely increased in recent years because of the ability of this methodology to provide an optimum control signal while explicitly accounting for state and input constraints [27]. However, the computational burden has always been a disadvantage when employing MPC algorithms in real-time for applications with fast dynamics [28]. Recent developments in MPC have resulted in different methods to approximate the MPC control signal explicitly as a function of states without performing time consuming real-time optimization [28-32]. This explicit formulation of MPC is often referred to as Explicit MPC (EMPC), a survey of which can be found in [33]. Recently, Chakrabarty et al. [32] introduced an explicit form for the NMPC problem for systems with uncertainty based on the sparse grid approximation method. In this paper the concept of using universal approximators (i.e., a network that can approximate continuous functions on compact subsets of $\mathbf{R}^n$ [34]) suggested by Chakrabarty et al. [32] for creating EMPCs is extended using feed forward neural networks with sigmoid basis functions that are known to be universal approximators [35-37].

This paper is organized as follows. The experimental setup is explained first, followed by system modeling and issues that arises during modeling. In Section 4, the details of the control structure are explained. In order to evaluate the proposed method, the controller design parameters are determined and a systematic way to select process parameters are described in Section 5. In Section 6, the results of experimental implementation of the proposed method are presented and the benefits of using the proposed method instead of the hybrid method proposed in [19] are illustrated.

2. Experimental setup

As seen in Fig. 1, the FEF system has three extruders, enabling the machine to fabricate functionally-graded parts with up to three different materials. Each extruder comprises a ram and a plunger that pushes paste through a reservoir and into a mixing chamber. Each ram is driven by a linear axis, which is actuated by a Kollmorgen servomotor (N2 Series AKM23D) operating through a Servostar300 amplifier. The maximum achievable ram velocity is 3.33×10–3 m/s. Attached to the end of each ram is a load cell (Omega LC-305) with a maximum load rating of 4448 N. The maximum allowable extrusion force on this system is set to 800 N.

A 1010 PXI chassis with three data acquisition cards and a PXI-8115 controller card is used for real-time control. A PXI-6602 counter/timer card measures the rams' motor positions, while a PXI-6025E multifunction card acquires load cell measurements. In addition, a PXI-6711 analog output card is used for sending the command voltages to the ram motors' amplifiers.

The three extruders are attached to a three-axis gantry system controlled by a Delta Tau Turbo PMAC card accepting G&M motion codes via PEWIN 32 software. The Delta Tau card can communicate with the PXI chassis and Labview through analogue signals measured by the PXI-6025 E card. Using this communication channel, ram velocity and start and stop commands of each extruder are sent to Labview, and then control signals are calculated in Labview and sent to the motor amplifiers of the extrusion axes. The maximum allowable table velocity is 25.4 mm/s.

3. System dynamics

The ram dynamics are

$$\dot{V}_r(t) = -\frac{1}{\tau_r} V_r(t) + \frac{K_r}{\tau_r} V_c(t) + \frac{1}{\tau_r} F_{fr}(t) \tag{1}$$

where τ_r (s) is the mechanical time constant, V_r (m/s) is the ram velocity, K_c ((m/s)/V) is the gain, V_c (V) is the control voltage, and F_{fr} (V) is the nonlinear friction. A study by Li et al. [16] focused on modeling the extrusion force using first principles. In their study, the extrusion force dynamics are

$$\dot{F}_r(t) = G(F_r)\left[V_r(t) - V_a(t)\right] \tag{2}$$

where $G(F_r) = \dfrac{\left(F_r(t) - F_{fp} + A_p p_{atm}\right)^2}{A_p p_0 l_0}$, F_r (N) is the ram force, F_{fp} (N) is the friction force between plunger and the reservoir, A_p (m^3) is the plunger cross sectional area, P_0 (Pa) is the initial pressure in the syringe, l_0 (m) is the initial effective air layer thickness, and V_a (m/s) is the paste bulk velocity (i.e., the paste steady state ram velocity

for a given extrusion force), which is a function of paste rheology and nozzle diametere. The model parameters are found by parameter estimation methods as described in [19] and V_r and F_r are measurements. Based on previous studies [38], the bulk velocity can be determined experimentally for each batch of paste and nozzle length and diameter. To do so, a ram velocity control loop is configured, a set of step ram velocity references in the range of operation are commanded, and the steady state extrusion forces at each corresponding ram velocity are recorded. Next, a function relating the steady state ram velocity to extrusion force is fit to the data and used to describe the paste bulk velocity V_a. In Fig. 2, the steady state data for two types of paste extruded with different nozzle diameters are shown. A linear model is fit to the data for each case. Case 1 is the data extracted from the study in [19] where Alumina paste with 45% solids loading is extruded with a 0.609 diameter (mm) × 6.35 length (mm) nozzle. Case 2 is also for Alumina; however, the solids loading is 40% and the nozzle length is 25.4 mm. Case 3 is for a Gypsum based paste by Sheetrock® that is extruded with a 0.609 × 25.4 mm nozzle. Case 4 is for the same Gypsum paste, but extruded with a 0.609 × 12.7 mm nozz1e. The slopes, offsets, and goodness of fit for each data set are shown in Table 1. The high goodness of fit indicates the data is well-modeled by a linear function.

As can be seen in Fig. 2, variations in paste material or nozzle geometry can cause the steady state relationship between F_r and V_r to change significantly affecting the bulk velocity function V_a. Also, because of paste preparation inconsistencies, the amount of air bubbles can change from one batch to the other which affects the value of l_0.

The Hybrid General Tracking Controller (HGTC) proposed by Deuser et al. [19] was based on a methodology that, for each batch of paste and every nozzle geometry,

needed to identify the bulk velocity function and initial amount of air in the reservoir. However, repeating the identification procedure of these unknown parameters every time the paste material or nozzle dimension changes is time consuming and wastes paste. In this work, the effect of variations in $G(F_r)$ and V_a on the force dynamics are captured by a disturbance function, which is estimated online. The function $G(F_r)$ and paste bulk velocity function, V_a, are modeled by

$$\begin{aligned} G\left(F_r\right) &= G_0\left(F_r\right) + \delta G\left(F_r\right) \\ V_a\left(t\right) &= V_{a,0}\left(t\right) + \delta V_a\left(t\right) \end{aligned} \tag{3}$$

where $G_0(F_r)$ and $V_{a,0}$ are the nominal functions for $G(F_r)$ and paste bulk velocity function V_a, respectively, and $\delta G(F_r)$ and δV_a are deviations from the nominal functions. Substituting equation (3) into equation (2), the extrusion force dynamics are

$$\dot{F}_r\left(t\right) = G_0\left(F_r\right)\left[V_r\left(t\right) - V_{a,0}\left(t\right)\right] + d\left(t\right) \tag{4}$$

where

$$d\left(t\right) = -G_0\left(F_r\right)\delta V_a\left(t\right) + \delta G\left(F_r\right)\left(V_r\left(t\right) - V_{a,0}\left(t\right) - \delta V_a\left(t\right)\right) \tag{5}$$

Next, an adaptive disturbance estimation technique is used to estimate the disturbance function in real-time [20, 21, 39]. It is now assumed that the function d can be approximated with a set of basis functions of the ram velocity and extrusion force

$$d\left(t\right) = \left[\mathbf{w}\left(t\right)^T\right]_{1\times k}\left[\boldsymbol{\varphi}\left(t\right)\right]_{k\times 1} \tag{6}$$

where $\mathbf{w}$ is the vector of coefficients, $\boldsymbol{\varphi}$ is a vector of known basis functions of measured variables, which are determined by investigating the nature of the problem, and k is the total number of basis functions. An estimate of d is

$$\hat{d}(t) = \left[\hat{\mathbf{w}}(t)^T\right]_{1\times k}\left[\boldsymbol{\varphi}(t)\right]_{k\times 1} \tag{7}$$

where $\hat{\mathbf{w}}$ is an estimate of the coefficient vector, $\mathbf{w}$. Assuming an estimate of d is available, the following observer is designed for the extrusion force

$$\dot{\hat{F}}_r(t) = G_0(F_r)\left[V_r(t) - V_{a,0}(t)\right] + \hat{d}(t) + K_{obs}\left(F_r(t) - \hat{F}_r(t)\right) \tag{8}$$

where $\hat{F}_r$ is an estimate of F_r and K_{obs} is a positive definite scalar. A stabilizing update rule that ensures boundedness for the extrusion force estimation error and for the estimated vector of coefficients, $\hat{\mathbf{w}}$, is [40]

$$\left[\dot{\hat{\mathbf{w}}}(t)\right]_{k\times 1} = \Gamma\left(\left[\boldsymbol{\varphi}(t)\right]_{k\times 1}\tilde{F}_r^T(t) - \sigma\left[\hat{\mathbf{w}}(t)\right]_{k\times 1}\right) \tag{9}$$

where $\tilde{F}(t) = F_r(t) - \hat{F}_r(t)$ is the ram force estimation error, $\boldsymbol{\Gamma}$ is the rate of adaptation, and σ is a robustifing term to ensure the boundedness of $\hat{\mathbf{w}}$ [40]. The parameter K_{obs} must be chosen large enough to allow the designer to choose large adaptive gains ($\boldsymbol{\Gamma}$) for fast adaptation, but not too large that high frequency oscillations occur in $\hat{\mathbf{w}}$.

A common method to choose a proper set of basis functions is to examine the nature of the problem [21]. In equation (3), assuming the deviations from the nominal functions can be described by the same structure as the nominal functions, based on equation (2), $\delta G(F_r)$ can be described by second order polynomial. Also, since a linear fit is used for modeling the bulk velocity function, V_a, a linear function is used for δV_a. Therefore, considering equation (5), the following vector of basis functions is used

$$\boldsymbol{\varphi}(t) = \left[\bar{F}_r^2(t)\bar{V}_r(t) \quad \bar{F}_r(t)\bar{V}_r(t) \quad \bar{V}_r(t) \quad \bar{F}_r^3(t) \quad \bar{F}_r^2(t) \quad \bar{F}_r(t) \quad 1\right]^T \tag{10}$$

where $\bar{F}_r(t) = \frac{F_r(t)}{F_{r,\max}}$ is the normalized extrusion force, $\bar{V}_r(t) = \frac{V_r(t)}{V_{r,\max}(t)}$ is the normalized ram velocity, $F_{r,\max}$ (N) is the maximum allowable extrusion force, and $V_{r,\max}$ (m/s) is the maximum allowable ram velocity. Here, the normalized variables are used, in order for the elements of $\hat{\mathbf{w}}$ to be in the same order of magnitude. Next, a hierarchical control structure is proposed to regulate the extrusion force and ram velocity dynamics in order to systematically perform start/stop on demand, fast air bubble compensation, and normal extrusion.

4. Control structure

The HMPC controller structure is now described. As mentioned previously, the fastest way to start and stop extrusion is by controlling the extrusion force. Therefore, when a start or stop command is detected the emphasis should be completely placed on force tracking; however, during the extrusion to ensure a specific paste flow, emphasis should be placed on ram velocity tracking. In addition, if an air bubble release occurs during extrusion, the emphasis should be placed on extrusion force tracking in order for the extrusion force to return to its operating value quickly. When the extrusion force reaches its operating value, the emphasis should be switched back to ram velocity tracking.

In this section, a hierarchical controller is designed to regulate the extrusion process. At the higher level, i.e., the supervisory level, an algorithm is designed to detect the system status (i.e., extrusion start/stop, air bubble release, normal extrusion) and

manipulate the cost function in the lower level controller in order to place emphasis on either extrusion force or ram velocity tracking. At the lower level, i.e., the process level, for each control objective (i.e., cost function configuration), an EMPC is generated based on a neural network approximation of an NMPC with the corresponding cost function.

In order to setup the process level, the system dynamics are given in a state space representation. First, the ram velocity error dynamics are

$$\Delta \dot{V}_r(t) = -\frac{1}{\tau_r}\Delta V_r(t) + \left(\frac{1}{\tau_r}F_{fr}(t) - \dot{V}_{ref}(t) - \frac{1}{\tau_r}V_{ref}(t)\right) + \frac{K_r}{\tau_r}V_c(t) \tag{11}$$

where $\Delta V_r(t) = V_r(t) - V_{ref}(t)$ is the ram velocity error and V_{ref} (m/s) is the reference ram velocity. Next, using equation (4), a state space presentation of the system can be obtained as

$$\dot{\mathbf{X}}(t) = \mathbf{f}\left(\mathbf{X}(t)\right) + \mathbf{B}V_c(t) + \mathbf{d}(t) \tag{12}$$

where $\mathbf{X}(t) = \left[\Delta V_r(t) \quad F_r(t)\right]^T$,

$$\mathbf{f}\left(\mathbf{X}(t)\right) = \begin{bmatrix} -\frac{1}{\tau_r}\Delta V_r(t) + \left(\frac{1}{\tau_r}F_{fr}(t) - \dot{V}_{ref}(t) - \frac{1}{\tau_r}V_{ref}(t)\right) \\ G_0\left(F_r(t)\right)\left[\Delta V_r(t) + V_{ref}(t) - V_{a,0}(t)\right] \end{bmatrix}, \qquad \mathbf{d}(t) = \begin{bmatrix} 0 \\ \hat{d}(t) \end{bmatrix}, \quad \text{and}$$

$\mathbf{B} = \begin{bmatrix} K_r/\tau_r \\ 0 \end{bmatrix}$. Next, the process level is configured by designing an EMPC for the system in equation (12), which rejects estimated disturbances.

4.1. *Process level*

In this section, an NMPC problem is formulated for the process dynamics that can reject the effect of estimated disturbances. Next, a neural network approximation is used to construct an EMPC for real-time implementation in the lower level of the control structure. Since the system in equation (12) is in control affine form, an NMPC problem can be formulated with the following cost function

$$\begin{aligned} & V_c^*(t) = \arg\min_{V_c(\tau)} \int_t^{t+T_f} \left(\Delta\mathbf{X}(\tau)^T \mathbf{Q}(\tau) \Delta\mathbf{X}(\tau) + V_c(\tau)^T R V_c(\tau) \right) d\tau \\ & \text{subject to:} \\ & \begin{cases} \dot{\mathbf{X}}(\tau) = \mathbf{f}\left(\mathbf{X}(\tau)\right) + \mathbf{B} V_c(\tau) + \mathbf{d}(\tau) \\ V_c(\tau) \in \mathbb{U}, \forall \tau \in \left[t, t+T_f\right] \end{cases} \end{aligned} \tag{13}$$

where $\Delta\mathbf{X}(t) = \mathbf{X}(t) - \begin{bmatrix} 0 & F_{ref}(t) \end{bmatrix}^T$ is the modified system state errors, T_f (s) is the specified prediction horizon, $\mathbf{Q} = \mathbf{Q}^T > 0$ and $R = R\mathrm{T} > 0$ are weighting matrices, and $\mathbb{U}$ is the control signal domain. The matrix $\mathbf{Q}$ is modified online in the supervisory level in order to change the objectives of the process level. Knowing the variable set $\left(\Delta V_r(t), F_r(t), V_{ref}(t), F_{ref}(t), \hat{d}(t), \mathbf{Q}(t), R\right)$, a nonlinear constrained optimization problem can be solved to find the optimum control signal. However, as mentioned before, one disadvantage of MPC is that it is very computationally expensive and not suitable for fast varying processes. However, different methods have recently been developed in order to explicitly approximate the MPC control signal as a function of states without performing time consuming real-time optimization [28-32]. In this work, the concept of using universal approximators for generating explicit form of MPC, introduced by Chakrabarty et al. [32], is used. Here, a feed forward neural network with sigmoid basis

function is used to approximate the control signal in the typical operating range of FEF processes. To this end, initially the domain of variations of the states, references, disturbance, and weights are found based on physical limitations and experiments, and an equidistance multidimensional grid of states and other parameters is formed in that domain. Next, the constrained nonlinear optimization problem in equation (13) is solved at every point on the grid and saved to memory. Next, a feed forward neural network with Sigmoid basis function is constructed and trained with the grid points as the inputs and the solution of the NMPC problem at every point as the output. This neural network is then placed in the lower level of the control structure and used for real-time implementation.

4.2. *Supervisory level*

Manufacturing parts with complex geometries or intricate features using extrusion, typically requires many starts and stops. To decrease the time required for starting and stopping extrusion, as suggested in [10], extrusion force control can be used. Once the extrusion force reaches the reference value, in order to obtain a consistent paste flow rate, the ram velocity should be regulated at the reference ram velocity.

Sometimes during extrusion, large drops in the extrusion force are noticed that are caused by the release of large air bubbles that have been trapped in the paste during the preparation process [7, 10]. Air bubble release can cause a void in the printed part [10]. To minimize the effect of air bubble release, the extrusion force should be returned to the reference value as quickly as possible. When an excessive drop in extrusion force is

detected, the control system should change control objectives from ram velocity tracking to extrusion force tracking and drive the extrusion force back to the reference value.

In order to achieve objective changes during the process, the supervisory level manipulates the cost function in the controller at the process level. To this end first **Q** is designed as $\mathbf{Q}(t)=\begin{bmatrix} q_{\Delta V}(t) & 0 \\ 0 & q_{\Delta F}(t) \end{bmatrix}$, where $q_{\Delta V}$, and $q_{\Delta F}$ are weights on the ram velocity error, and extrusion force error, respectively, and $q_{\Delta V}$ is a function of $q_{\Delta F}$

$$q_{\Delta V}(t)=q_{\Delta V}^{\max}\left(1-q_{\Delta F}(t)\Big/q_{\Delta F}^{\max}\right) \tag{14}$$

where $q_{\Delta V}^{\max}$ and $q_{\Delta F}^{\max}$ are the maximum values for $q_{\Delta V}$ and $q_{\Delta F}$, respectively. The parameter $q_{\Delta F}^{\max}$ is chosen by fixing R in equation (13) and setting $q_{\Delta F}(t)=q_{\Delta F}^{\max}$, which results in $q_{\Delta V}(t) = 0$, and finding a value of $q_{\Delta F}^{\max}$ resulting in the best extrusion force tracking in the operating range, while $q_{\Delta V}^{\max}$ is selected by setting $q_{\Delta F}(t) = 0$ and finding the largest value for $q_{\Delta V}^{\max}$ that results in a stable ram velocity tracking. Next, $q_{\Delta F}$ is calculated using a hysteresis function

$$q_{\Delta F}(t)=\begin{cases} q_{\Delta F}^{\max} & \left|\Delta F_r(t)\right| \geq \Delta F_{outer} \\ 0 & \left|\Delta F_r(t)\right| \leq \Delta F_{inner} \\ q_{\Delta F}(t-dt) & \text{otherwise} \end{cases} \tag{15}$$

where dt (s) is the time step, ΔF_{inner} (N) is the extrusion force error inner bound and is equal to the measurement resolution, and ΔF_{outer} (N) is the extrusion force error outer bound and is the amount of allowable force error during ram velocity tracking.

In Fig. 3, the hysteresis function in equation (15) is illustrated during start and stop commands. At point ①, the system is at rest and, since $|\Delta F_r(t)| \leq \Delta F_{inner}$ at this point, $q_{\Delta F}(t) = 0$, which means full emphasis is on ram velocity tracking ($V_{ref}(t) = 0$). At point ②, an extrusion start is requested and instantly F_{ref} changes to 400 N (i.e., the extrusion force for this example). At this point $|\Delta F_r(t)| \geq \Delta F_{outer}$ and, as a result, $q_{\Delta F}$ switches to $q_{\Delta F}^{\max}$; hence, full emphasis is on extrusion force tracking. While $|\Delta F_r(t)| \geq \Delta F_{inner}$, extrusion force tracking is emphasized (indicated by area ③) until $|\Delta F_r(t)| \leq \Delta F_{inner}$ (i.e., point ④). This results in the controller switching to full emphasis on ram velocity control. This continues throughout area ⑤, even though there are variations in the extrusion force. At point ⑥, a stop command is detected since $|\Delta F_r(t)| \geq \Delta F_{outer}$ and, therefore, extrusion force control is emphasized until point ⑦, from which point the emphasis is switched to ram velocity control. The values of $q_{\Delta F}$ for all the points and areas are shown in Fig. 3-b.

5. Determining design and process parameters

In this section the controller design parameters are determined experimentally. Also, the process parameters required to print successful parts are determined. In order to identify the parameter values for the disturbance estimator, the guidelines in [41] are adopted. Starting with a small value for K_{obs}, the largest value for $\boldsymbol{\Gamma}$ is found that does not cause unstable estimations. If no value for $\boldsymbol{\Gamma}$ was found K_{obs}, is increased and the process is repeated until a right combination is found. Next, for every value of $\boldsymbol{\Gamma}$, the minimum

value for σ is found such that low amounts of oscillations in the estimated force are observed while not too small that causes unstable estimation. A proper combination of these parameters for this application was found to be $K_{obs} = 100$, $\sigma = 0.1$, and $\mathbf{\Gamma} = 1\times10^4$ *eye*(7). Next, domains of operation for the states are defined. Based on the mentioned limits on maximum ram velocity and extrusion force, the operational domain for ram velocity and extrusion force are $V_r(t) \in [-3.30, 3.30] \times10^{-3}$ (m/s) and $F_r(t) \in [0,1000]$ (N) respectively.

Next, in order to evaluate the domain of variations for $\hat{d}$, a square ram velocity reference with a frequency of 0.1 (Hz), maximum of 3.28 (mm/s) and minimum of -3.30 (mm/s) are commanded to the system in order to excite the extrusion force dynamics with the fastest ram motion possible. Since in this motion the negative velocity is larger than the positive velocity, after every cycle, the ram position at the lowest position after each cycle stays higher than the previous cycle. As a result the maximum force applied to the plunger will decrease after each cycle and therefore, the variation of $\hat{d}$ can be analyzed at all the possible force values. Since based on equation (4), the value of $\hat{d}$ depends on the deviation of the dynamics from the nominal dynamics of the system. Deviation from the nominal model was created in the system by changing the nozzle and by injecting different amounts of air into the paste intentionally. It was found that the largest values of $\hat{d}$ was generated when the nozzle was clogged and large amounts of air were injected into the paste. In Fig. 4, two cases of pastes investigated are shown; one with very small amount of air in paste and one with a very large amount of air injected into the paste intentionally (i.e., approximately 10 ml air for 30 ml paste which is a ratio of 33%). It can

be seen that as the amount of air increases variations of $\hat{d}$ increases. However, even in the case with a large amount of air in the paste, $\hat{d}(t) \in [-25000, 10000]$ (N/s). Therefore, this boundary is selected as the domain of variations for $\hat{d}$. It should be noted that if during implementation it was found that the selected domains of operation for any of the variables were not large enough, the training process could be repeated with the modified operational domain.

Next, the cost function's weights were determined experimentally. Setting $R = 1$ and $q_{\Delta F}(t) = 0$, $q_{\Delta V}(t) = q_{\Delta V}^{\max}$ (i.e., large emphasis on ram velocity control), different values of $q_{\Delta V}^{\max}$ were tested and the optimum values resulting in the best ram velocity tracking where found to be $q_{\Delta V}^{\max} = 2 \times 10^6$. The same process was repeated for large emphasis on force control i.e., $q_{\Delta F}(t) = q_{\Delta F}^{\max}$ and $q_{\Delta V}(t) = 0$. The optimum value was found to be $q_{\Delta F}^{\max} = 10$.

In order to implement the NMPC algorithm in real-time, an explicit form of NMPC is needed. Therefore, setting $R = 1$, for each possible value of $\mathbf{Q}$, the domain of operation for all of the variables in the optimization ($\Delta V_r(t)$, $F_r(t)$, $V_{ref}(t)$, $F_{ref}(t)$, $\hat{d}(t)$) was determined and an equidistance grid of these variables was generated. Next, the NMPC problem from equation (13) was solved with ten steps ahead prediction horizon and five steps control horizon (selected based on the processor speed limitations), for all the grid points using the "fmincon" function in Matlab. Next, a feed forward neural network with one hidden layer, and "Sigmoid" basis functions was generated to approximate the solutions of the NMPC problem. For this problem, 20 neurons were

found to be enough in approximating the signal. In Fig. 5, results of the neural network approximation versus the actual NMPC control signal evaluated at all the points in the generated grid, is shown. It can be seen that for full emphasis on ram velocity the maximum approximation error is approximately 0.02 (V) while for the case of full emphasis on force control this value is approximately 1.5 (V). However, as can be seen from Fig. 6, after implementing the EMPC with full emphasis on force the steady state error in force tracking was found to be approximately one sensor resolution in all the desired range of operation.

The parameters in the higher level are determined next. In this work, $\Delta F_{low} = 7$ N, which is the force measurement resolution, and $\Delta F_{high} = 50$ N which is the amount of allowable force deviation from the reference extrusion force before an air bubble release is detected.

After finding the parameters in the HMPC control structure, a set of process parameters need to be found for the printing process. To this end, a set of experiments are performed in which dash lines were printed with different nozzle diameters and a range of ram velocities and table feed rates. For every nozzle, an acceptable ram velocity is defined by a ram velocity that results in a steady state extrusion force less than 800 N. In order to find the extrusion force for every ram velocity, the paste is extruded with that ram velocity for a period of time until the paste starts extruding out of the nozzle and the extrusion force settles on a steady state value. This process should be performed whenever the paste or the nozzle type is changed. Three different nozzle diameters were considered here (i.e., 0.303, 0.406, and 0.609 mm). For each nozzle the maximum ram velocity was found, and a number of extrusion velocities in the allowable range was

defined. For every ram velocity the velocity of the paste at the nozzle outlet (called nazzle velocity here) is calculated by

$$V_n = \frac{r_p V_r}{r_n} \times 10^3 \tag{16}$$

where r_n mm is the radius of the nozzle, r_p mm is the radius of the plunger, and V_n (mm/s) is the nozzle velocity. For every V_n, a number of table feed rates were defined from zero to 25.4 mm/s which is the maximum allowable table feed rate. Next, for every nozzle and ram velocity a number of dash lines each with a different table feed rate was printed and each experiment was repeated three times. After this, using *imagej* software the thickness of the dash lines were measured in multiple points along the printed line. Fig. 7, shows a sample of the printed lines for the 0.609 mm nozzle and ram velocity of 0.01 mm/s. Fig. 8, shows the line thickness normalized by nozzle diameter, with three standard deviation lines, versus the table feed rate normalized by nozzle velocity. From these experiments it was concluded that generally, whenever the table velocity is in the range of (0.7-1.1)×V_n, the printed line thickness is approximately equal to the nozzle thickness which is normally the desired thickness during a print process. Therefore, for every nozzle it is desired for the ram velocity to be limited such that its corresponding nozzle velocity is less that the maximum table feed rate (i.e., V_n < 25.4 mm/s) in order to make it possible to print at table feed rates of (0.7-1.1)×V_n.

The extrusion start process as explained in [19] involves a dwell time in which the gantry waits for the paste to start extruding before moving. The dwell time that gives the best start and stop needs to be found every time the process parameters or the paste, change.

6. Results and discussion

The performance of the proposed controller is evaluated experimentally in this section. The HMPC is implemented in real-time using Labview, and a set of dash line extrusion tasks with several starts and stops are requested from the system. In order to investigate the advantages of the HMPC method, the HGTC proposed in [19] was also implemented in Labview. Two batches of paste were considered for extrusion using 0.609 mm diameter nozzles with HGTC and HMPC; a paste based on Gypsum by Sheetrock® (called Gypsum paste here) and an Alumina paste with 60% solids loading (called Alumina paste here). The ram velocity was fixed at 0.01 mm/s for both pastes. For printing Gypsum a 12.7 mm length was used, and for Alumina a 6.35 mm length nozzle was used. As a result the extrusion force for Gypsum at 0.01 mm/s ram velocity was found to be 190 N and for Alumina 585 N. The dwell time for Gypsum was found to be 70 ms and for Alumina 200 ms. In order for the line thickness to be approximately equal to the nozzle diameter a table federate of $0.72V_n$ (i.e., 16.9 mm/s) was used here for all the experiments.

First, HGTC was tuned for extruding Gypsum. For tuning HGTC, a relationship for bulk velocity and the initial air layer thickness were determined by a process described in [19]. As can be seen from Table 1, the bulk velocity relationship for printing Gypsum using a 12.7 mm length nozzle was found to be Va(t) = 10-6(0.0913Fr(t) – 12.860). In addition, the initial air layer thickness for this paste was found to be 1 mm. Next, the poles for ram velocity control and extrusion force control are found to achieving the best possible tracking in both cases. After this a switching time for

switching from extrusion force control to ram velocity control, is found such that it allows the extrusion force to reach the reference value and switch to ram velocity control after that point. Three dash lines were printed and the thickness of the lines were measured in the printing direction at 12 points. The results of extrusion using HGTC were then compared to the ones from HMPC. Fig. 9-a and b show the extrusion force, ram velocity and the control signal during the extrusion of one dash line with Gypsum using HMPC and HGTC respectively. In Fig. 9, the state of $q_{\Delta F}$ is shown by High (i.e., $q_{\Delta F} = q_{\Delta F}^{\max}$) and Low (i.e., $q_{\Delta F} = 0$) status. Also, the thicknesses of the printed dash lines as well as the measure thicknesses can be seen in Fig. 10-a and b, and Fig. 11 respectively. As can be seen, a thickness of 0.6-0.7 mm was achieved for both cases.

Next, HMPC and the HGTC tuned for Gypsum were used for extruding Alumina using a 6.35 mm long nozzle. It can be seen from Fig. 9-d that the extrusion force when using HGTC that is not tuned for Alumina, overshoots by approximately 150 N and since the switching time is 0.5 s the controller does not have enough time to reach the steady extrusion force and the printing process results in inconsistent dash line thickness, as shown in Fig. 10-d and Fig. 11. Also, as can be seen in Fig. 9-e, increasing the switching time to 1 seconds will only reveal the oscillatory behavior of the untuned force controller which results in a more inconsistent line thickness as shown in Fig. 10-e and Fig. 11. These experiments show an extreme case of paste variation, which reveals the necessity of tuning the HGTC in these cases and robustness of the HMPC to paste variations. In order to retune HGTC for Alumina all the above mentioned experiments need to be repeated, which is time consuming and results in a substantial amount of wasted paste.

7. Summary and conclusions

In this paper a hierarchical control structure was proposed incorporating an EMPC in the process level with disturbance rejection capabilities and a hysteresis switching algorithm in the supervisory level for providing systematic control objective changes during a paste extrusion process.

In the process level, the variations in process dynamics due to paste material and nozzle geometry changes are considered as a disturbance to the nominal dynamics. The disturbance function is estimated in real-time, using an adaptive estimator, and fed into a neural network based explicit approximation of an NMPC along with the states, state references and the cost function weights. In the supervisory level, depending on the system status (i.e., extrusion start/stop, air bubble release, normal extrusion), the cost function weights are updated and fed into the process level.

Performance of the proposed controller was investigated through extrusion of different paste materials and variations in nozzle length. It was shown that the proposed controller always results in a consistent extrusion line thickness regardless of the system variations.

References

[1] A. N. Samant, and N. B. Dahotre, "Laser machining of structural ceramics—A review", *Journal of the European Ceramic Society*, 2009, vol. 29, no. 6, pp. 969-993.

[2] J. A. Lewis, "Direct-write assembly of ceramics from colloidal inks", *Current Opinion in Solid State and Materials Science*, 2002, vol. 6, no. 3, pp. 245-250.

[3] N. Travitzky, A. Bonet, B. Dermeik, T. Fey, I. Filbert-Demut, L. Schlier, T. Schlordt, and P. Greil, "Additive manufacturing of ceramic-based materials", *Advanced Engineering Materials*, 2014, vol. 16, no. 6, pp. 729-754.

[4] M. Allahverdi, S. C. Danforth, M. Jafari, and A. Safari, "Processing of advanced electroceramic components by fused deposition technique", *Journal of the European Ceramic Society*, 2001, vol. 21, no. 10–11, pp. 1485-1490.

[5] I. Grida, and J. R. G. Evans, "Extrusion freeforming of ceramics through fine nozzles", *Journal of the European Ceramic Society*, 2003, vol. 23, no. 5, pp. 629-635.

[6] J. A. Lewis, J. E. Smay, J. Stuecker, and J. Cesarano, "Direct ink writing of three-dimensional ceramic structures", *Journal of the American Ceramic Society*, 2006, vol. 89, no. 12, pp. 3599-3609.

[7] D. Kupp, H. Eifert, M. Greul, and M. Kunstnerm, "Rapid prototyping of functional metal and ceramic components by the multiphase jet solidification process", *Solid Freeform Fabrication Symposium*, Austin, Texas, 1997, 11-13 August.

[8] R. van Noort, "The future of dental devices is digital", *Dental Materials*, 2012, vol. 28, no. 1, pp. 3-12.

[9] U. Deisinger, "Generating porous ceramic scaffolds: Processing and properties", *Key Engineering Materials*, 2010, vol. 441, pp. 155-179.

[10] J. N. Stuecker, J. Cesarano, and D. A. Hirschfeld, "Control of the viscous behavior of highly concentrated mullite suspensions for robocasting", *Journal of Materials Processing Technology*, 2003, vol. 142, no. 2, pp. 318-325.

[11] T. S. Huang, M. N. Rahaman, N. D. Doiphode, M. C. Leu, B. S. Bal, D. E. Day, and X. Liu, "Freeze extrusion fabrication of 13-93 bioactive glass scaffolds for repair and regeneration of load-bearing bones," *Biomaterials Science - Processing, Properties, and Applications*, pp. 45-55: John Wiley & Sons, Inc., 2011.

[12] T. Huang, M. S. Mason, X. Zhao, G. E. Hilmas, and M. C. Leu, "Aqueous-based freeze-form extrusion fabrication of alumina components", *Rapid Prototyping Journal*, 2009, vol. 15, no. 2, pp. 88-95.

[13] M. C. Leu, B. K. Deuser, L. Tang, R. G. Landers, G. E. Hilmas, and J. L. Watts, "Freeze-form extrusion fabrication of functionally graded materials", *CIRP Annals - Manufacturing Technology*, 2012, vol. 61, no. 1, pp. 223-226.

[14] X. Lu, Y. Lee, S. Yang, Y. Hao, J. R. G. Evans, and C. G. Parini, “Solvent-based paste extrusion solid freeforming”, *Journal of the European Ceramic Society*, 2010, vol. 30, no. 1, pp. 1-10.

[15] J. E. Smay, G. M. Gratson, R. F. Shepherd, J. Cesarano, and J. A. Lewis, “Directed colloidal assembly of 3D periodic structures”, *Advanced Materials*, 2002, vol. 14, no. 18, pp. 1279-1283.

[16] M. Li, L. Tang, R. G. Landers, and M. C. Leu, “Extrusion process modeling for aqueous-based ceramic pastes-part 1: Constitutive model”, *ASME Journal of Manufacturing Science and Engineering*, 2013, vol. 135, no. 5, pp. 051008.

[17] X. Zhao, R. G. Landers, and M. C. Leu, “Adaptive extrusion force control of freeze-form extrusion fabrication processes”, *ASME Journal of Manufacturing Science and Engineering*, 2010, vol. 132, no. 6, pp. 064504.

[18] B. K. Deuser, L. Tang, R. G. Landers, M. C. Leu, and G. E. Hilmas, “Hybrid extrusion force-velocity control using freeze-form extrusion fabrication for functionally graded material parts”, *ASME Journal of Manufacturing Science and Engineering*, 2013, vol. 135, no. 4, pp. 041015.

[19] K. Rajagopal, A. Mannava, S. Balakrishnan, N. Nguyen, and K. Krishnakumar, “Neuroadaptive model following controller design for non-affine non-square aircraft system”, *AIAA Guidance, Navigation and Control*, Chicago, 2009, 10-13 August.

[20] R. Padhi, N. Unnikrishnan, and S. N. Balakrishnan, “Model-following neuro-adaptive control design for non-square, non-affine nonlinear systems”, *Control Theory and Applications, IET*, 2007, vol. 1, no. 6, pp. 1650-1661.

[21] J. M. Maciejowski, "Predictive control with constraints": Prentice Hall, 2002.

[22] P. Patrinos, and H. Sarimveis, “A new algorithm for solving convex parametric quadratic programs based on graphical derivatives of solution mappings”, *Automatica*, 2010, vol. 46, no. 9, pp. 1405-1418.

[23] M. M. Seron, J. A. De Dona, and G. C. Goodwin, “Global analytical model predictive control with input constraints”, *IEEE Conference on Decision and Control*, Sydney, NSW, 2000, 12-15 December.

[24] A. Bemporad, M. Morari, V. Dua, and E. N. Pistikopoulos, “The explicit linear quadratic regulator for constrained systems”, *Automatica*, 2002, vol. 38, no. 1, pp. 3-20.

[25] C. N. Jones, and M. Morrari, “Multiparametric linear complementarity problems”, *IEEE Conference on Decision and Control*, San Diego, CA, 2006, 13-15 December.

[26] A. Chakrabarty, V. Dinh, G. T. Buzzard, S. H. Zak, and A. E. Rundell, “Robust explicit nonlinear model predictive control with integral sliding mode”, *American Control Conference*, Portland, OR, 2014, 4-6 June.

[27] A. Alessio, and A. Bemporad, "A survey on explicit model predictive control," *Nonlinear Model Predictive Control*, Lecture Notes in Control and Information Sciences L. Magni, D. Raimondo and F. Allgöwer, eds., pp. 345-369: Springer Berlin Heidelberg, 2009.

[28] B. C. Csáji, “Approximation with artificial neural networks,” Faculty of Sciences, Etvs Lornd University, 2001.

[29] Z. Chen, and F. Cao, “The approximation operators with sigmoidal functions”, *Computers and Mathematics with Applications*, 2009, vol. 58, no. 4, pp. 758-765.

[30] G. Cybenko, “Approximation by superpositions of a sigmoidal function”, *Mathematics of Control, Signals, and Systems*, 1992, vol. 5, no. 4, pp. 455.

[31] K. I. Funahashi, “On the approximate realization of continuous mappings by neural networks”, *Neural Networks*, 1989, vol. 2, no. 3, pp. 183-192.

[32] M. Li, L. Tang, R. G. Landers, and M. C. Leu, “Extrusion process modeling for aqueous-based ceramic pastes-part 2: Experimental verification”, *ASME Journal of Manufacturing Science and Engineering*, 2013, vol. 135, no. 5, pp. 051009.

[33] A. Toghraee, D. A. Bristow, and S. N. Balakrishnan, “Estimation of tip-sample interaction in tapping mode AFM using a neural-network approach”, *American Control Conference*, Montreal, QC, 2012, 27-29 June.

[34] K. Rajagopal, S. Balakrishnan, J. E. Steck, and D. Kimball, “Robust adaptive control of a general aviation aircraft”, *AIAA Atmospheric Flight Mechanics Conference*, Toronto, Ontario Canada, 2010, 2-5 August.

[35] A. Mannava, S. N. Balakrishnan, T. Lie, and R. G. Landers, “Optimal Tracking Control of Motion Systems”, *IEEE Transactions on Control Systems Technology*, 2012, vol. 20, no. 6, pp. 1548-1558.

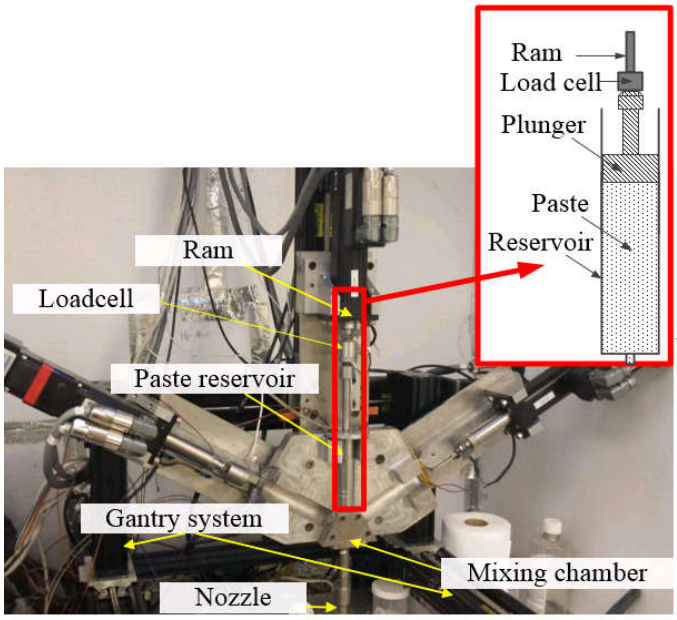

Fig. 1. FEF experimental system.

Table 1
Steady state relationship between extrusion force and ram velocity for various pastes and nozzle lengths, and a 0.609 mm nozzle diameter.

Case	Paste	Nozzle length (mm)	Slope ((μm/s)/N)	Offset (μm/s)	Goodness of fit
1	Alumina	6.35	0.0433	-12.5	0.963
2	Alumina	25.4	0.0691	-10.3	0.977
3	Gypsum	25.4	0.0535	-10.1	0.918
4	Gypsum	12.7	0.0914	-12.9	0.982

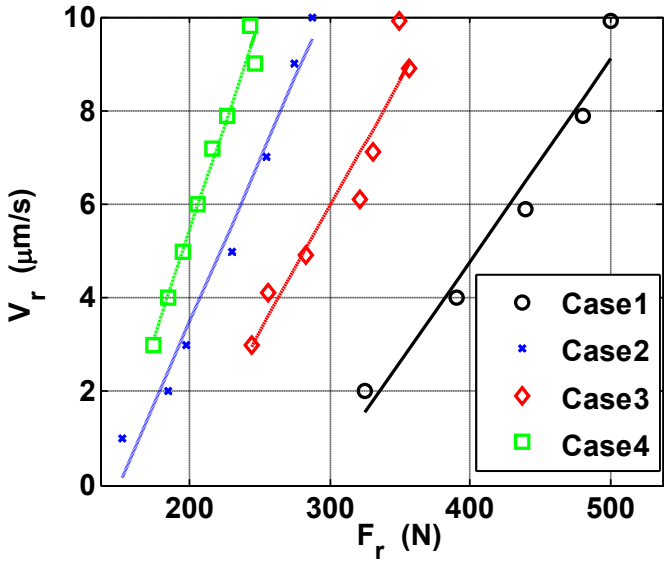

Fig. 2. Steady state ram velocity versus steady state extrusion force (Marker points denote experimental data and continuous lines denote the model).

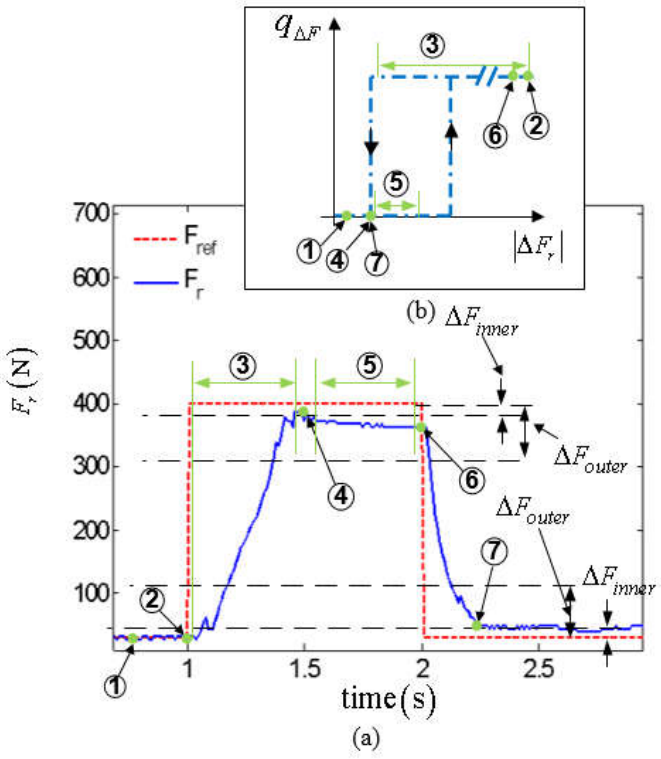

Fig. 3. Illustration of hysteresis switching function for q_F.

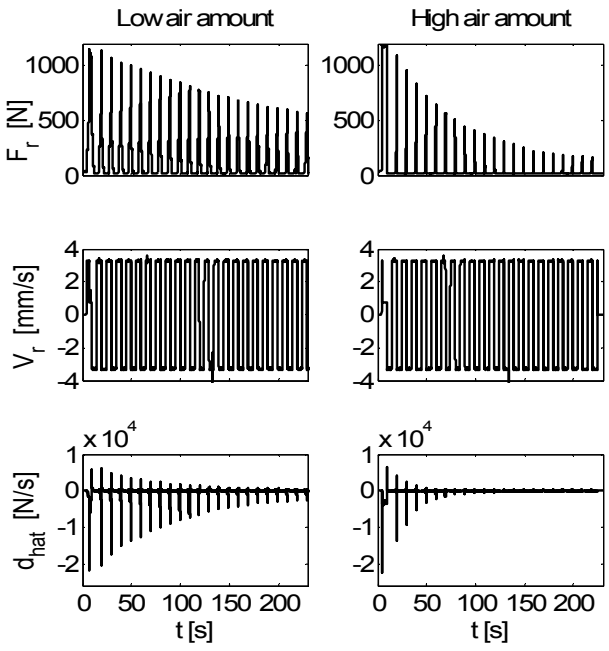

Fig. 4. Experimental investigation of disturbance bounds.

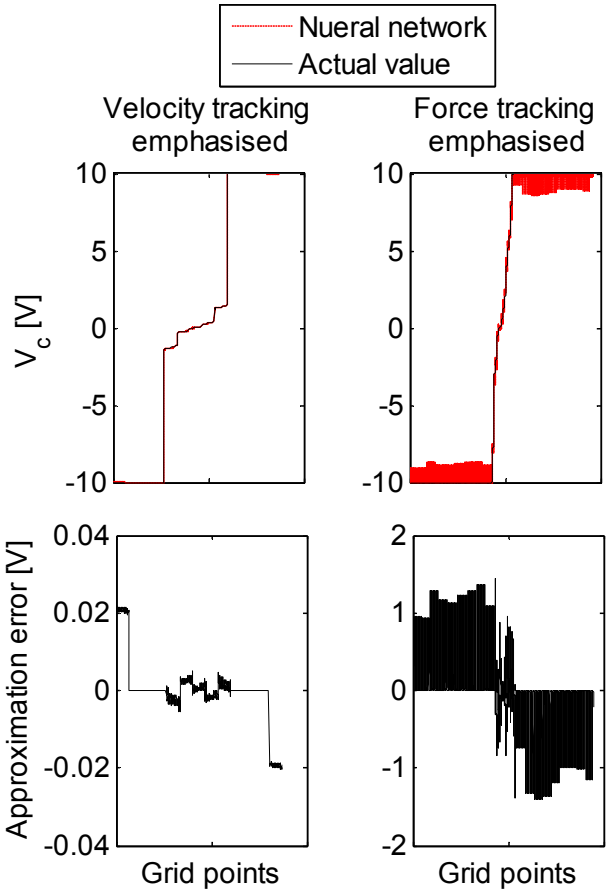

Fig. 5. Neural network approximation results.

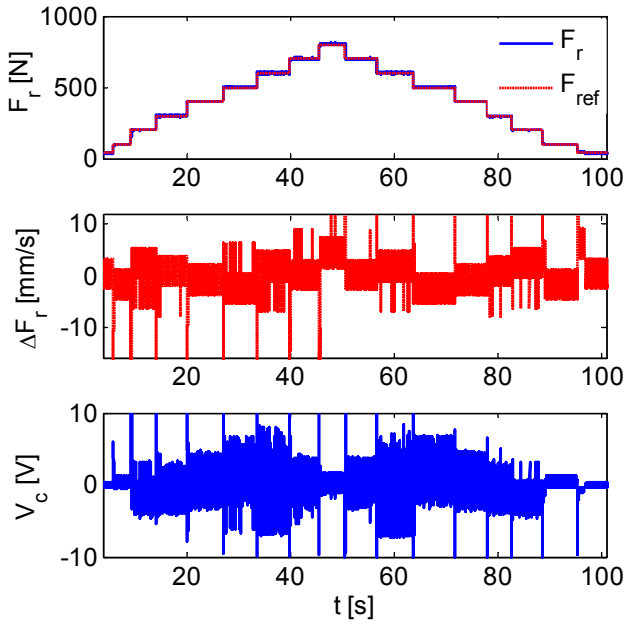

Fig. 6. Step test for evaluating the full emphasis on force tracking.

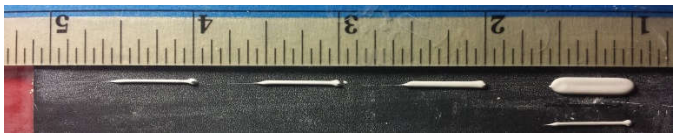

Fig. 7. Dash lines printed with 0.609 mm diameter nozzle and ram velocity of 0.01 mm/s and variable table feed rates.

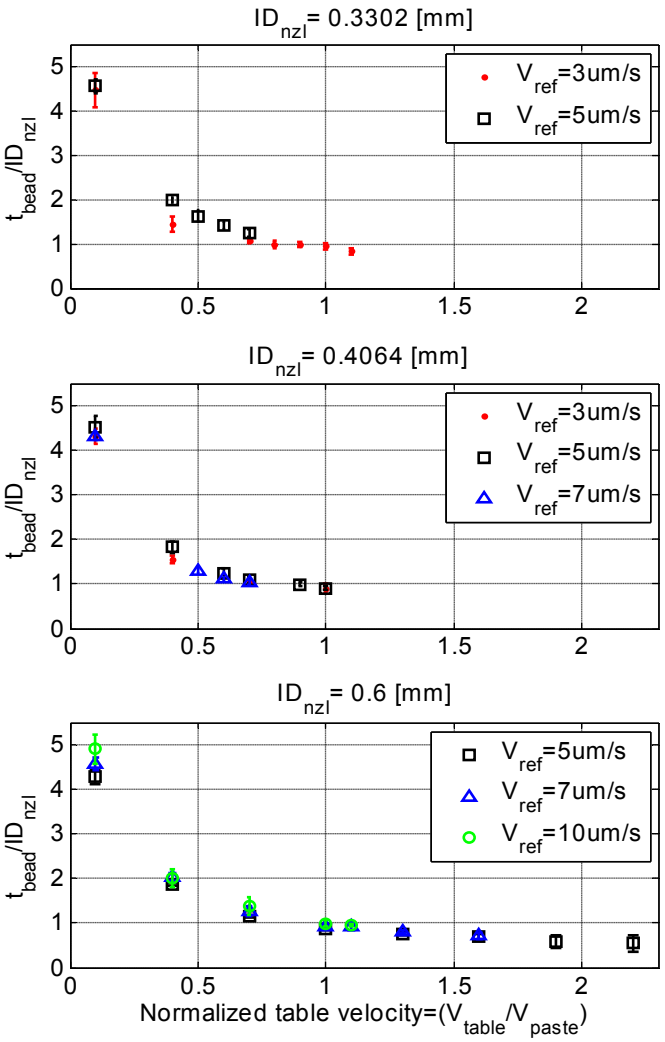

Fig. 8. Normalized thickness versus normalized table feed rate .

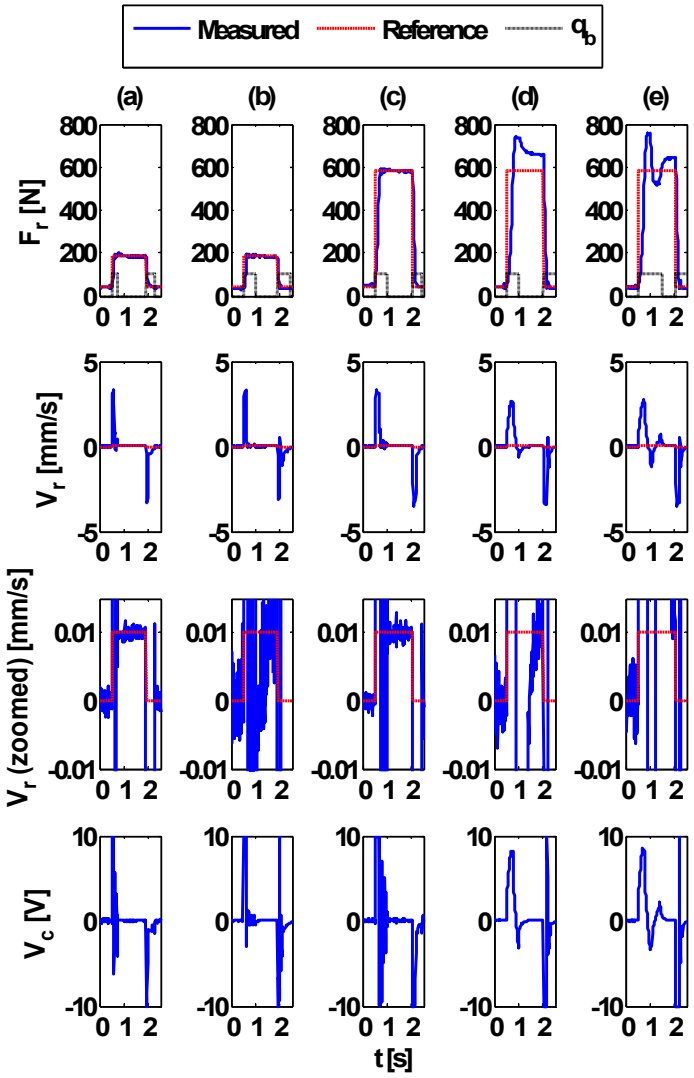

Fig. 9. Extrusion force, ram velocity, and command voltage signals for a)Gypsum with HMPC, b) Gypsum with HGTC tuned for printing Gypsum, c)Alumina with HMPC, d) Alumina with HGTC tuned for printing Gypsum, e) Alumina with HGTC tuned for printing Gypsum with switching time increased.

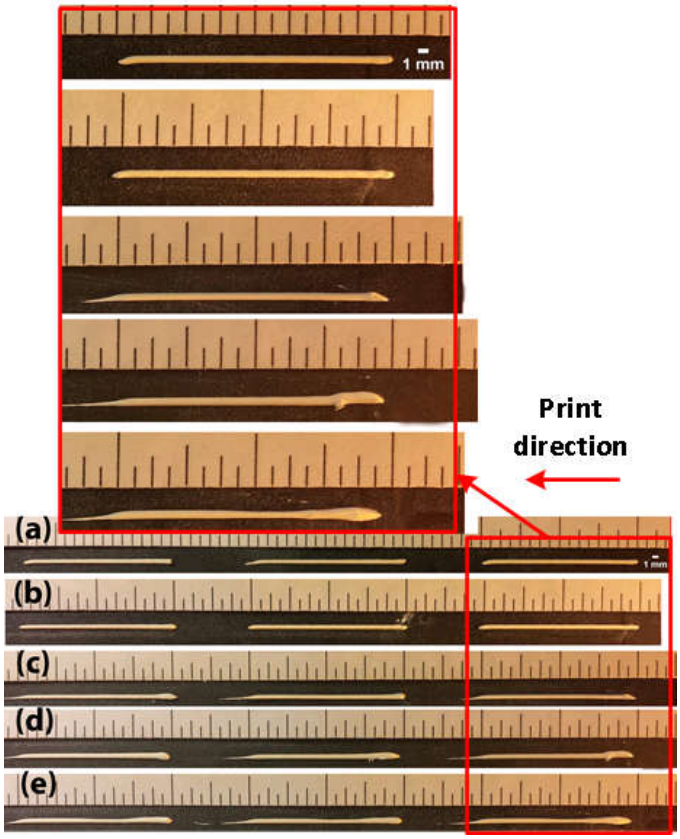

Fig. 10. Printed dash lines a) Gypsum using HMPC, b) Gypsum using HGTC tuned for printing Gypsum, c) Alumina using HMPC, d) Alumina using HGTC tuned for printing Gypsum, e) Alumina using HGTC tuned for printing Gypsum with switching time increased.

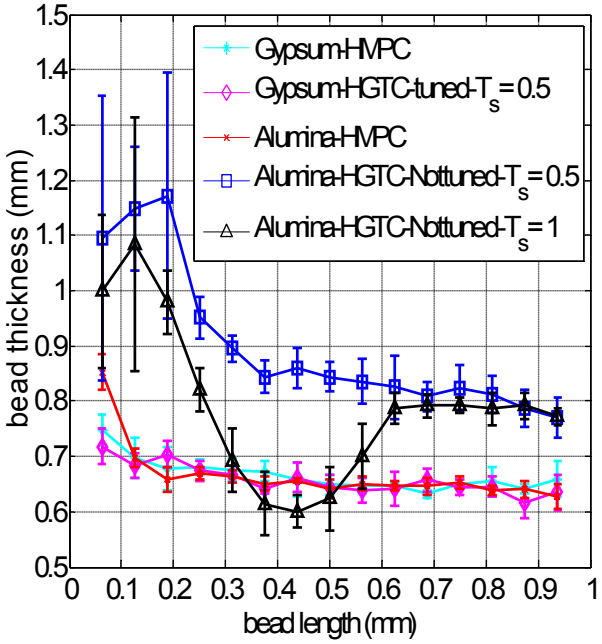

Fig. 11. Comparison of line thicknesses along the line length.

SECTION

2. SUMMARY AND CONCLUSIONS

In this study, the use of hierarchical control structures for controlling complex systems with changing objectives was investigated. The results of which, are published in three papers that comprise this dissertation and are presented in the sections titled “Paper I”, “Paper II”, and “Paper III”. The hierarchical structure proposed in this study is comprised by a supervisory level (i.e., a decision making stage responsible for changing control objectives) and a process level (i.e., a local controller capable of controlling a system with different objectives). In the first two parts of this study only the process level controller was considered. A hierarchical controller called Hierarchical Optimal Control was introduced with the capability of controlling a motion system and a micro milling process with different objectives (e.g., force control versus position control). Multiple tests showed the performance of the controller with respect to changing objectives in two different applications in manufacturing. In the third section, a hierarchical controller was introduced (called Hierarchical Model Predictive Controller) that was comprised of a process level controller based on Nonlinear Model Predictive Controller and a supervisory level for automated control objective changes during a Freeze-form Extrusion Fabrication process.

In the first paper, the problem of tracking complex contours in motion systems was considered. In tracking a contour, when the axial error regulation cannot be improved, sometimes, reducing the contour error (i.e., the closest distance from actual point to the desired contour) is possible, which can be beneficial in improving the

tolerance of the machined part in an end milling process. In section "Paper I", the Hierarchical Optimal Control method was developed that provided a platform for changing the control objective from axial tracking to contour tracking and back, while tracking a desired path. The process dynamics in this system was analyzed in two levels. The contour error was considered in a higher level and the axial error dynamics were considered in a lower level. A relationship, called the aggregation relationship, between the contour error and the axial errors was derived. This relationship was then used to simplify an optimal control problem with a cost function including the cost from both axial and contour errors, from a nonlinear optimal control problem into a linear one.

The proposed controller was implemented in Simulink and was used to control a table top CNC machine. To show the performance of the controller in response to control objective changes, a set of experiments were performed in which the emphasis of the controller's objective was changed from axial tracking to contour tracking by changing the value of axial error weight versus the contour error weight in the cost function of the optimal control problem. The experiments showed that when the axial errors could not be reduced (e.g., when the control signal is saturated), placing more emphasis on contour regulation could reduce the contour error. However at steady state, since the axial errors were within 2 encoder resolutions (i.e., 0.1 μm), changing the emphasis on contour error would not affect the contour error.

In the second part of this study (i.e., section "Paper II"), the Hierarchical Optimal Control structure was extended to be used for force/position control of an end milling process. Like the previous part, the process in this part was analyzed in two levels. In the higher level, error between the maximum cutting force per each spindle revolution and

the reference maximum cutting force was considered, and in the lower level, the axial position errors were considered. In order to aggregate the maximum cutting force error from the higher level into the lower level, a mechanistic model of the cutting force was developed and, after linearization, a linear relationship (i.e., called aggregation relationship) was found between the maximum cutting force error and axial errors. An optimal controller was then developed with a cost including the maximum cutting force and the axial position errors. Using the aggregation relationship the optimal controller with a nonlinear cost was simplified into a linear problem. Also, in order to change the controller objective the weight on maximum cutting force and the axial position error are changed.

The controller performance was evaluated through simulation studies for cutting a diamond contour using an end milling process. In order to investigate how changing the weights on the maximum cutting force error versus position error (i.e., the emphasis of the control objective on each) affects the controller performance, multiple cases were defined where the ratio of maximum cutting force error's weight over the position error's weight would increase. It was found that increasing this ratio would result in a decrease in the cutting force error without sacrificing the contour error.

In order to show the effectiveness of the proposed method a normal optimal controller was also implemented with no consideration of cutting force in the higher level by setting the weight on the higher level to zero. Multiple simulation tests were performed with the normal optimal controller where the weight on axial tracking was increased to improve the axial tracking performance. Comparing the resulting contour error for both methods, it was found that as the emphasis on the tracking error was

increased in both methods, the contour error would decrease and at the maximum emphasis on axial tracking for both methods, the contour error would reach the same magnitude. However, comparing the maximum cutting forces revealed that at the maximum emphasis on axial tracking the proposed method results in a lot smaller force error compared to the normal optimal control method. Therefore, it was found out that including the aggregated maximum cutting force in the formulation would always result in less cutting force without sacrificing the contour tracking performance.

In the third part of this study, using a hierarchical control structure for force/velocity control in ram based extrusion of ceramic pastes was investigated. The control design requirement for this system was to be able to change the control objective (i.e., emphasis on extrusion force or ram velocity tracking) based on the system status (i.e., start/stop extrusion, air bubble release, extrusion force at steady condition). The proposed hierarchical control structure for this system comprised a supervisory level (i.e., responsible for detecting the system status) as well as a process level (i.e., responsible for generating a control signal based on the current system objective). In the process level a Nonlinear Model Predictive Controller (NMPC) was formulated with a cost function including the effect of extrusion force tracking error as well as ram velocity tracking error. Since the extrusion force dynamics in this system had significant variations due to paste material and nozzle geometry changes, for the control design, a nominal extrusion force model was used that included an additive disturbance function representing the variations in the nominal model. An adaptive estimation algorithm was implemented to estimate the disturbance function in real time.

In order to be able to implement the NMPC in real time, an explicit form of the NMPC was developed through neural network approximation. The inputs to this explicit form are the weights of the state errors, which are determined by the supervisory level, the extrusion force, the ram velocity, their reference values, and the value of the disturbance function, which is calculated in real time by the disturbance estimator and the output is the approximated control signal.

In the supervisory level, an algorithm for detecting the system status (i.e., start/stop extrusion, air bubble release, extrusion force at steady condition) was developed based on a hysteresis switching function and the emphasis of the controller was changed through adjustments to the states' weights in the process level cost function. The performance of the total control structure was investigated experimentally through extrusion of multiple dash lines that involved several starts and stops during extrusion. When compared to previous methods for controlling the extrusion system, it was revealed that the proposed controller always results in a consistent line thickness regardless of the paste material.

REFERENCES

[1] H. Zomorodi Moghadam, R. G. Landers, and S. N. Balakrishnan, “Hierarchical optimal force-position control of complex manufacturing processes”, Control Engineering Practice, 2014, vol. 25, pp. 75-84.

[2] H. Zomorodi Moghadam, R. G. Landers, and S. N. Balakrishnan, “Hierarchical optimal contour control of motion systems”, Mechatronics, 2014, vol. 24, no. 2, pp. 98-107.

[3] R. J. Furness, A. G. Ulsoy, and C. L. Wu, “Supervisory Control of Drilling”, Journal of Engineering for Industry, 1996, vol. 118, no. 1, pp. 10-19.

[4] M. Ozaki, “Supervisory control of drilling of composite materials,” Doctoral, Engineering-Mechanical Engineering, University of California Berkeley, 2000.

[5] T. Takahashi, T. Tsuboi, T. Kishida, Y. Kawanami, S. Shimizu, M. Iribe, T. Fukushima, and M. Fujita, “Adaptive grasping by multi fingered hand with tactile sensor based on robust force and position control”, IEEE International Conference on Robotics and Automation, Pasadena, CA, 2008, 19-23 May.

[6] A. G. Ulsoy, and Y. Koren, “Control of machining processes”, ASME Journal of dynamic systems, measurement, and control, 1993, vol. 115, pp. 301-308.

[7] T. Moor, and J. Raisch, “Hierarchical hybrid control of a multiproduct batch plant”, IFAC World Congress, Prague, Czech Republic, 2005, August.

[8] R. G. Landers, and S. N. Balakrishnan, “Hierarchical optimal contour-position control of motion control systems”, ASME International Mechanical Engineering Congress and Exposition, Anaheim, California, 2004, November 13 – 19, 2004.

[9] Y. Tang, R. G. Landers, and S. N. Balakrishnan, “Hierarchical optimal force-position-contour control of machining processes”, Control Engineering Practice, 2006, vol. 14, no. 8, pp. 909-922.

[10] H. C. Lee, and G. J. Jeon, “Real-time compensation of two-dimensional contour error in CNC machine tools”, IEEE/ASME International Conference on Advanced Intelligent Mechatronics, Atlanta, Georgia, 1999, September 19-23, 1999.

[11] Y. Koren, “Cross-coupled biaxial computer control for manufacturing systems”, ASME Journal of Dynamic Systems, Measurement and Control, 1980, vol. 102, no. 4, pp. 265-272.

[12] L. Feng, Y. Koren, and J. Borenstein, “Cross-coupling motion controller for mobile robots”, IEEE Control Systems Magazine, 1993, vol. 13, no. 6, pp. 35-43.

[13] J. H. Chin, and T. C. Lin, “Cross-coupled precompensation method for the contouring accuracy of computer numerically controlled machine tools”, International Journal of Machine Tools and Manufacture, 1997, vol. 37, no. 7, pp. 947-967.

[14] B. Chu, S. Kim, D. Hong, H.-K. Park, and J. Park, “Optimal cross-coupled synchronizing control of dual-drive gantry system for a SMD assembly machine”, JSME International Journal, 2004, vol. 47 Series C, no. 3, pp. 939-945.

[15] P. K. Kulkarni, and K. Srinivasan, “Optimal contouring control of multi-axial feed drive servomechanisms”, ASME Journal of Engineering for Industry, 1989, vol. 111, no. 2, pp. 140-148.

[16] G. Franklin, J. Powell, and A. Emami-Naeini, "Feedback control of dynamic systems", 3rd edition ed.: Addison-Wesley Reading, 1994.

[17] B. Siciliano, "Parallel Force/Position Control of Robot Manipulators," Robotics Research, G. Giralt and G. Hirzinger, eds., pp. 78-89: Springer London, 2000.

[18] K. Khayati, P. Bigras, and L. A. Dessaint, “A Multistage Position/Force Control for Constrained Robotic Systems With Friction: Joint-Space Decomposition, Linearization, and Multiobjective Observer/Controller Synthesis Using LMI Formalism”, IEEE Transactions on Industrial Electronics, 2006, vol. 53, no. 5, pp. 1698-1712.

[19] N. Kumar, V. Panwar, N. Sukavanam, S. Sharma, and J.-H. Borm, “Neural network based hybrid force/position control for robot manipulators”, International Journal of Precision Engineering and Manufacturing, 2011, vol. 12, no. 3, pp. 419-426.

[20] V. F. Filaretov, and A. V. Zuev, “Adaptive force/position control of robot manipulators”, IEEE/ASME International Conference on Advanced Intelligent Mechatronics, 2008, 2-5 July 2008.

[21] Y. Ping-Lang, and L. Cheng-Hsin, “Impedance force control for lateral milling of bone in total knee arthroplasty”, IEEE International Conference on Systems, Man and Cybernetics, ISIC., 2007, 7-10 Oct. 2007.

[22] A. Bierbaum, J. Schill, T. Asfour, and R. Dillmann, “Force position control for a pneumatic anthropomorphic hand”, 9th IEEE-RAS International Conference on Humanoid Robots, 2009, 7-10 Dec. 2009.

[23] J. Huang, I. Todo, and T. Yabuta, “Position/force hybrid control of a manipulator with a flexible tool using visual and force information”, Cutting Edge Robotics, 2005, pp. 611-628.

[24] Y. Karayiannidis, G. Rovithakis, and Z. Doulgeri, “Force/position tracking for a robotic manipulator in compliant contact with a surface using neuro-adaptive control”, Automatica, 2007, vol. 43, no. 7, pp. 1281-1288.

[25] J. Roy, and L. L. Whitcomb, “Adaptive force control of position/velocity controlled robots: theory and experiment”, IEEE Transactions on Robotics and Automation, 2002, vol. 18, no. 2, pp. 121-137.

[26] A. Visioli, G. Ziliani, and G. Legnani, “Iterative-Learning Hybrid Force/Velocity Control for Contour Tracking”, IEEE Transactions on Robotics, 2010, vol. 26, no. 2, pp. 388-393.

[27] T. Kroger, B. Finkemeyer, M. Heuck, and F. M. Wahl, “Adaptive implicit hybrid force/pose control of industrial manipulators: compliant motion experiments”, IEEE/RSJ International Conference on Intelligent Robots and Systems, IROS, 2004, 28 Sept.-2 Oct. 2004.

[28] A. N. Samant, and N. B. Dahotre, “Laser machining of structural ceramics—A review”, Journal of the European Ceramic Society, 2009, vol. 29, no. 6, pp. 969-993.

[29] J. A. Lewis, “Direct-write assembly of ceramics from colloidal inks”, Current Opinion in Solid State and Materials Science, 2002, vol. 6, no. 3, pp. 245-250.

[30] N. Travitzky, A. Bonet, B. Dermeik, T. Fey, I. Filbert-Demut, L. Schlier, T. Schlordt, and P. Greil, “Additive manufacturing of ceramic-based materials”, Advanced Engineering Materials, 2014, vol. 16, no. 6, pp. 729-754.

[31] T. S. Huang, M. N. Rahaman, N. D. Doiphode, M. C. Leu, B. S. Bal, D. E. Day, and X. Liu, "Freeze extrusion fabrication of 13-93 bioactive glass scaffolds for repair and regeneration of load-bearing bones," Biomaterials Science - Processing, Properties, and Applications, pp. 45-55: John Wiley & Sons, Inc., 2011.

[32] J. N. Stuecker, J. Cesarano, and D. A. Hirschfeld, “Control of the viscous behavior of highly concentrated mullite suspensions for robocasting”, Journal of Materials Processing Technology, 2003, vol. 142, no. 2, pp. 318-325.

[33] X. Lu, Y. Lee, S. Yang, Y. Hao, J. R. G. Evans, and C. G. Parini, “Solvent-based paste extrusion solid freeforming”, Journal of the European Ceramic Society, 2010, vol. 30, no. 1, pp. 1-10.

[34] J. A. Lewis, J. E. Smay, J. Stuecker, and J. Cesarano, “Direct ink writing of three-dimensional ceramic structures”, Journal of the American Ceramic Society, 2006, vol. 89, no. 12, pp. 3599-3609.

[35] J. E. Smay, G. M. Gratson, R. F. Shepherd, J. Cesarano, and J. A. Lewis, "Directed colloidal assembly of 3D periodic structures", Advanced Materials, 2002, vol. 14, no. 18, pp. 1279-1283.

[36] T. Huang, M. S. Mason, X. Zhao, G. E. Hilmas, and M. C. Leu, "Aqueous-based freeze-form extrusion fabrication of alumina components", Rapid Prototyping Journal, 2009, vol. 15, no. 2, pp. 88-95.

[37] M. C. Leu, B. K. Deuser, L. Tang, R. G. Landers, G. E. Hilmas, and J. L. Watts, "Freeze-form extrusion fabrication of functionally graded materials", CIRP Annals - Manufacturing Technology, 2012, vol. 61, no. 1, pp. 223-226.

[38] M. Li, L. Tang, R. G. Landers, and M. C. Leu, "Extrusion process modeling for aqueous-based ceramic pastes-part 1: Constitutive model", ASME Journal of Manufacturing Science and Engineering, 2013, vol. 135, no. 5, pp. 051008.

[39] X. Zhao, R. G. Landers, and M. C. Leu, "Adaptive extrusion force control of freeze-form extrusion fabrication processes", ASME Journal of Manufacturing Science and Engineering, 2010, vol. 132, no. 6, pp. 064504.

[40] B. K. Deuser, L. Tang, R. G. Landers, M. C. Leu, and G. E. Hilmas, "Hybrid extrusion force-velocity control using freeze-form extrusion fabrication for functionally graded material parts", ASME Journal of Manufacturing Science and Engineering, 2013, vol. 135, no. 4, pp. 041015.

VITA

Hesam Zomorodi Moghadam attended the Science and Research branch of Azad University, Tehran, Iran from 2001 to 2005 where he received his B.Sc. degree in Mechanical Engineering. He started his graduate studies in Mechanical Engineering in Sharif University of Technology, Tehran, Iran, and received his M.Sc. degree in 2008. Hesam joined the Mechanical Engineering department of Missouri University of Science and Technology, Rolla, Missouri, in 2009 to pursue his PhD under the supervision of Dr. Robert G. Landers. He received his PhD degree in 2016.

His PhD research focused on Hierarchical Control theory development, analysis, and implementation for complex manufacturing systems. He has also worked on several other projects such as development, analysis, and control of electro-mechanical systems and modeling, analysis and control of fuel cell systems. He has presented his work in 5 different conferences and 4 journal papers.